FZU
Fyzikální ústav Akademie věd České republiky

Faculty of Science
Palacký University Olomouc

Department of Physical Chemistry

Doctoral Thesis

Chemical and Physical Properties of Nanostructures on Surface Investigated by Scanning Probe Microscopy

Author: Ing. Vijai Meena Santhini

Supervisor: Doc. Ing. Pavel Jelínek, Ph.D.

Olomouc 2021

This thesis entitled "**Chemical and Physical Properties of Nanostructures on Surface Investigated by Scanning Probe Microscopy**" is an original work carried out by me, enrolled in Department of Physical Chemistry, Palacký University, Olomouc, Czech Republic. The research work was done under the supervision of **Dr. Pavel Jelínek** at Institute of Physics (FZU), Czech Academy of Sciences, Prague, Czech Republic. This work is original and has not been previously submitted to this or any other University for the award of any degree, diploma or fellowship. The information and data given in this thesis is authentic to the best of my knowledge. All information derived from the work of others has been acknowledged in the text and a list of references is provided.

In **Olomouc** Date: **02-06-2021**

Author's Signature

Acknowledgements

I express my sincere gratitude to my supervisor Dr. Pavel Jelínek, Institute of Physics (FZU) for his encouragement, patience and above all, for his guidance through the entire course of my work in experimental surface science. I am thankful for his inspiration and for being welcoming and helpful at all times.

It is my pleasure to be associated with the following prestigious institutions in Czech Republic for my doctoral thesis: Department of Physical Chemistry, Palacký University (UPOL), Olomouc; Institute of Physics (FZU), Czech Academy of Sciences, Prague and CATRIN-Regional Centre of Advanced Technologies and Materials (RCPTM), Olomouc. I thank them for giving me an opportunity to carry out my research as well as providing me all the research facilities for the work.

I am thankful to Prof. Dr. Michal Otyepka, my academic supervisor at CATRIN-RCPTM, Palacky University, for his constant support and guidance.

I would like to acknowledge my colleagues and friends of FZU and RCPTM: Martin Švec, Oleksander Stetsovych, Aleš Cahlík, Bruno de la Torre, Jan Berger Martin Ondraček, Pingo Mutombo, Jesús Mendieta, Benjamín Mallada, Aurelio Gallardo, Shayan Edalatmanesh, Adam Matěj, Jiří Doležal; my former colleagues of FZU: Jack Hellerstedt, Christian Wackerlin, Taras Chutora, Maria Moro and Narendra Prabhakar who have been ever supportive and motivated me both personally and professionally for the past five years.

I am grateful to Prof. Dr. Olivier Siri for providing me an opportunity to carry out a three-month internship in Centre Interdisciplinaire de Nanoscience de Marseille (CINam), University of Marseille, France. A great support from Simon Pascal and other group members led to the successful completion of a part of this research work. The people also provided with the necessary molecules for the experiments and other characterization results.

I would like to also thank the people at the Institute of Organic Chemistry and Biochemistry: Ivo Starý, Irena G. Stará, Jiři Klívar and the rest of the group for the synthesis of molecules, characterization experiments and other interesting discussions and thoughts.

I am short of words to express my gratitude to my parents, who forever have been a constant source of inspiration and encouraged me with all their love and support. I am also thankful to my friends and relatives for putting up with me and for always being there.

And finally, the universal power I believe in, I am thankful for being bestowed with everything I need, the strength and the willpower to complete this work.

Abstract

This thesis provides an alternative approach to traditional polymerization technique for synthesising polymers with organic molecules. It focuses on the growth of 1D polymers particularly metal coordinated polymers and polymers with organometallic monomers, on metal surfaces. The properties of these nanostructures on surfaces are studied with the help of Scanning Probe Microscopy (SPM) techniques.

The growth of 1D metal coordinated polymers by co-deposition of transition metals and quinone molecules onto metal surfaces under ultra-high vacuum is explored, and a difference in metal coordination has been observed depending on the choice of metal. The structural and electronic properties of these 1D coordination polymers are characterized by means of STM/nc-AFM with CO-functionalized tips and supported by DFT and other theoretical calculations. The synthesis of H-bonded wires with the same precursor molecule has been discussed to emphasize the difference on metal coordination.

A distinct 1D polymer made up of organometallic ferrocene monomer units on Ag(111) surface has been synthesised and the properties have been characterized with STM/nc-AFM technique. The charge transport in the 1D nanowire has been analysed by carrying out lifting experiments with the STM tip and a transport model has been devised theoretically.

Keywords: 1D polymers, metal coordinated, organometallic, SPM, quinone, ferrocene, SPM, AFM

Contents

Introduction

Nanotechnology is a branch of science which allows us to achieve precise control over matter, down to nanoscale or specifically the atomic level. The word “Nano” finds its origin in both Greek and Latin literature, *nanos* and *nanus* respectively, both of which mean “dwarf” [1]. It is a multidisciplinary field combining solid state physics, material science, chemistry and biosciences. Thus it is necessary to have a combined knowledge of these scientific disciplines rather than efficiency in any one [2].

The various aspects of nanotechnology focuses on creation and use of materials and structures in the size range of about 0.1-100 nm, that expanses from atomic to macromolecular length scales. These nanometre or atomic scale materials commonly known as nanomaterials are the ones with less than 100 nm size in at least one dimension. They possess different physicochemical properties compared to their bulk phase due to their shape and size. [3]

The nanomaterials can produce unique characteristics and capabilities on modification of their shape and size at the nanoscale level. These materials are found in different shapes depending on their dimensions; for example zero dimensional (0D) nanoparticles, one-dimensional (1D) nanorods and nanowires, two dimensional (2D) layers or films, and also three dimensional (3D) bulk nanomaterials such as nanocomposites, multi nanolayers etc. They might accommodate the demands of industries targeting on miniaturization, especially in the fields of micro and nanoelectronics. These materials will be of practical use only if they are economically

viable, thus it is necessary to explore strategies for mass fabrication of atomic or molecular assemblies in a controlled fashion. [1], [4]

There are three major routes in the synthesis of nanomaterials: biological, chemical, physical. The biological route concentrates on the synthesis of nanomaterials from plant extracts and microorganisms such as algae, bacteria etc. However there are two key approaches in physical and chemical synthesis of nanomaterials: top-down approach and bottom-up approach. In the top-down approach larger materials are reduced to smaller particles by mechanical methods. In the bottom-up approach, nanoparticles or smaller entities such as atoms or molecules are condensed together to form larger nanomaterials. [3]–[5]

In this context of synthesis of nanomaterials, nanofabrication is the most advanced technology involving processes and methods for creating nanostructures and devices on surfaces in a controlled and repeatable manner. The nanofabrication methods also come under the two categories: the top-down methods usually transfer or impose a pattern or structure onto the substrate which is being processed [6], [7]. The bottom-up preparation of nanostructures is substantially based on growth phenomena; aims on atomic and molecular self-assembly into organized structures on surfaces or in solutions. This approach is usually carried out by depositing atomic or molecular species on the substrate either under vacuum or ambient conditions, or in solution to form nanoscale structures by virtue of a myriad of atomistic processes occurring on surface. [1], [8]–[11]

The extreme potential of bottom-up approach of synthesis of nanomaterials has led to the development of a sub-category in the fields of surface science and chemistry, known as On-surface chemistry. This genre of chemistry is achieved by coupling of reactive

molecular building blocks on surfaces to form organized, extended nanostructures. Such protracted and expanded frameworks have a solubility limit in solution phase thus their synthesis is almost unlikely following traditional synthetic processes in wet chemistry. In comparison to synthesis in solution, on surface nanostructures and intermediate species have high stability due to the ultra-high vacuum (UHV) reaction conditions and surface interactions. The surface 2D confinement favours a higher range of temperatures and also enables the construction of planar nanostructures which otherwise are inaccessible in a three dimensional reaction environment. But there are problems in conducting on-surface chemistry, which do not appear in solution or wet chemistry. It is difficult to control site specific reactions and diffusion of reactive molecules into the substrate; it also requires specific experimental setup and UHV conditions thus only few reaction parameters can be varied and experiment needs to be tuned in prior. [3], [12]–[15]

This branch of surface science needs high resolving analysis methods to study and control the reactions directly at the surface. The invention of **scanning tunneling microscope (STM) and atomic force microscope (AFM)**, a breakthrough in this discipline serve as efficient tools to image and characterize materials at the atomic and submolecular scale, manipulate single atoms and molecules and investigate their reactivity in the assembled structures on surfaces [16]–[19]. Since then, chemists have been successful in preparing different dimensional (0D, 1D, 2D) molecular nanosystems on surfaces[3], [15].

The backbone of the **1D and 2D nanostructures** is mainly formed through different organic coupling reactions on surfaces such as Ullmann coupling, Glaser coupling, or dehydrogenative coupling etc., contributing to the carbon-carbon covalent bond; through hydrogen bonding and through coordinate bonding resulting in metal-carbon

bonds or metal bonds with heteroatoms of the ligand [20]–[23]. In this scenario, low dimensional nanostructures especially one-dimensional (1D) wires on surfaces have been extensively explored and employed due to their future applications in the field of molecular electronics [24]–[28].

Among the various on surface **1D nanostructures**, organometallic nanowires and metal-coordinated polymers are gaining a considerable recognition in the recent years due to their wide range of electrical, magnetic, optical and electrochemical properties. The genre of organometallic species is unique as they integrate the intrinsic properties of the metal with the functionalities of the macromolecules or organic species attached to them and exhibit a completely different dynamic behaviour or resemble the properties of both the constituents together. [20], [23], [29], [30]

The dissertation focuses on **two different types of 1D polymers** or nanowires on metal surfaces, which differ on the coupling reactions and nature of covalent bonding between the individual monomer units. The structure and properties of the 1D polymers have been investigated and characterized using **low temperature scanning tunneling microscope/atomic force microscope (LT-STM/AFM)** under ultra-high vacuum conditions. The chemical structures of the 1D nanowires are clearly resolved by obtaining high resolution AFM measurements with CO functionalized tips [31].

The first part of the thesis focuses on the synthesis of 1D H-bonded wires with a **quinoid ligand** (2,5-diamino- benzoquinonediimine). Quinoidal ligands have gained tremendous attention as ligands in coordination chemistry due to the design of the complexes which have a huge number of applications in molecular electronics, optics and magnetism. The synthesis of metal coordinated oligomers with the same ligand in

solution has not been successful due to solubility and purity issues. The downfall of wet chemistry in the synthesis of oligomers led to the idea of formation of **1D quinoid-metal coordinated polymer on surface**, wherein bond formation occurs between the metal atoms and suitable ligand as a result of multitude of on-surface reactions. The long flexible nanowires are formed on the surfaces by simultaneous dehydrogenation of the quinoid ligand and covalent-coordination bonding with the transition metals; the coordination modes depend on the choice of metal and/or the nature of the substrate thus show different structural and electronic properties.

The second part of the thesis concentrates on the formation of **1D organometallic polymer on surface**, where the individual monomer units itself are organometallic in nature. Halogenated ferrocene molecules have been used as monomers to form polyferrocenylene polymers on surface and the backbone of the polymer is achieved by C-C covalent bonding between the individual units through Ullmann coupling; however similar synthesis in wet chemistry in the previous decades was not much successful due to solubility issues, presence of impurities etc., thus leading to formation of low weight oligomers. Hence on surface synthesis of such organometallic polymers helps to overcome the limits of conventional solution polymerization thus characterize and study their structural and electronic properties at atomic scale.

1. Instrumentation

1.1. Scanning Probe Microscopy

The Scanning Probe Microscopy (SPM) is a vastly growing research technique in surface science and consists of a number of probe microscopes with similar working principle. The SPM techniques provide the possibility to study the morphology and local properties of a solid state surface with the atomic resolution. It has also evolved as a unique method for creating structures at nanometer scales on surfaces.

The scanning tunneling microscope invented in 1981 by Gerd Binnig and Heinrich Rohrer, is the first scanning probe microscope and since then has been used to study the atomic structure of surfaces. The duo scientists were awarded the Nobel Prize in Physics in 1986 for their remarkable invention. Later, atomic force microscope (AFM), magnetic force microscope (MFM), electric force microscope (EFM), Kelvin probe force microscope (KPFM) and many other devices altogether with STM constituted the family of scanning probe microscopes.

1.1.1. Working Principle of SPM

The surface microstructure and local properties are analysed with the help of scanning probe microscopes which mostly use tips specifically prepared for this purpose. The different probe microscopes employ various types of interactions between the tip and the surface to provide surface analysis, thus the recorded signals are different for each

microscope. The normal operating tip-surface distance is ~0.1-10 nanometres and the size of the tip or apex is about ten nanometers down to a single atom.

There is a common mechanism inherent to mostly all probe microscopes featuring a feedback system (FS) that controls the distance between the tip and the sample, as shown in schematic **Figure 1.1**. A unique detection parameter (P) dependent on the tip-sample distance is kept constant to the set value (P_o) by the feedback system; as the tip sample distance changes, this parameter changes. To keep this parameter constant, a differential signal is amplified and sent to the piezo transducer (PT) in the feedback system thus controlling the tip-sample distance. The transducer uses the change in the parameter value as signal to change the tip-sample distance thus controlling it to the highest accuracy possible. The surface topography of the sample can change the interaction parameter during the scanning process and the feedback system restores the pre-set value of the interaction parameter thus the tip-sample distance is controlled in real-time.

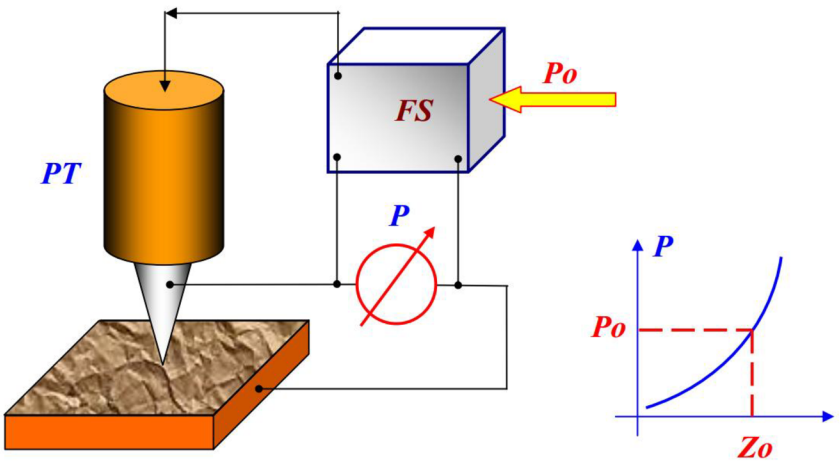

Figure 1.1: The block diagram of the feedback system in scanning probe microscope. Adapted from [32]

The process of mapping the surface topography and obtaining an SPM image is based on the above-mentioned mechanism. The tip is moved to a position (x,y) on the sample and the signal P(x,y) from the position is fed to the transducer which is considered to be proportional to the local displacement of the sample surface from the ideal plane. The values of P(x,y) at different positions are used to map the surface topography as a whole. The scanning process takes place consecutively in the form of a line scan and a frame scan. First the tip moves along a certain line on the sample, the value of the signal proportional to the height value in topography is fed to the transducer and recorded in the computer memory. Then the tip comes to the initial point and steps to the next line, defining the frame scan and the process is repeated. The recorded feedback signals are processed by the computer and the SPM surface topography image is plotted with the help of computer graphics. Apart from surface topography, many other surface properties such as electric, mechanical, optical etc. can also be investigated using SPM. [32]

1.2. Scanning Tunneling Microscope

The first microscope to be known in the family of probe microscopes is the Scanning Tunneling Microscope (STM). STM is an invaluable tool in the field of surface science, investigating a large number of metal and semiconductor surfaces providing an extraordinary atomic level spatial resolution. The first invention in this category was a topografiner in the 1970s by Young, Scire and Ward; it was able to achieve a resolution of 0.3 nm perpendicular and 20 nm lateral to the surface using field electron emission

and tunneling current. The spatial limitations of the topografiner were overcome by the invention of STM in the 1980s. [33]

1.2.1. Working Principle of STM

The major working principle of STM is based on quantum tunneling effect, which can be described as the phenomenon of electrons tunneling through a narrow potential barrier between metal tip and a conducting sample in the presence of an external electric field. The schematic representation in **Figure 1.2** shows the tunneling of electrons through a potential barrier in STM. When the STM tip approaches the sample surface at distances of several Angstroms, a tunnel-transparent barrier is formed. The barrier size is calculated with the values of work function for electron emission from the tip (φ_t) and the sample(φ_s). The effective barrier φ^* is equal to the average work function by considering the shape of the barrier to be rectangular:

$$\varphi^* = \frac{1}{2}(\varphi_s + \varphi_t)$$

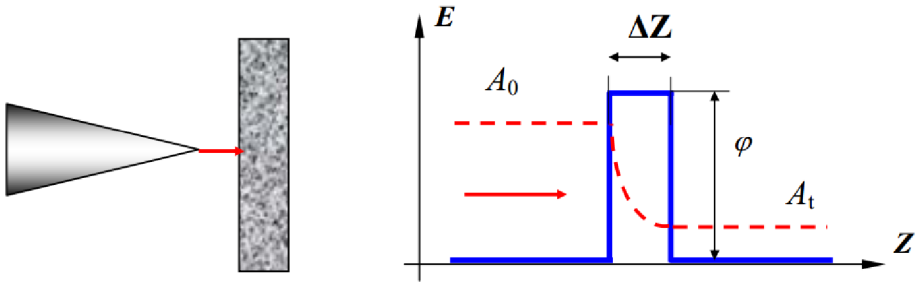

Figure 1.2: Scheme of electrons tunneling through a potential barrier in STM. Adapted from [32]

The schematic representation of STM operational principle and instrumentation is represented in **Figure 1.3**. The quantum tunneling occurs when an electrical potential is applied between two electrodes through a non-conducting gap; in case of STM the two electrodes resemble the metal tip and the metal or semiconductor surface and the non-conducting gap is the vacuum between the both. The tunneling of electrons occurs from occupied to unoccupied states in the direction governed by the potential applied between the tip and the surface. This phenomenon helps to derive a relationship on the tunneling current I between two infinite electrodes and the non-conducting gap d between them for low voltages:

$$I \approx \frac{V}{d} e^{-A\varphi^{\frac{1}{2}}d}$$

where A=0.125 $(eV)^{-1/2}$, V is the applied potential and φ is the average potential barrier height. This describes that for a tunneling barrier around 4 eV high, a 1 Å change in separation distance will lead to a change of one order of magnitude in the value of tunneling current. The increase in distance leads to the decrease in the tunneling current; this distance dependence relationship is the crucial element for the atomic resolution imaging capability of STM. Thus, a constant current can be maintained through a feedback mechanism and electronic structures of the surface can be mapped topographically, hence as already discussed, the common mechanism described above with respect to SPM is also inherent to the Scanning Tunneling Microscope. [18], [32], [34], [35]

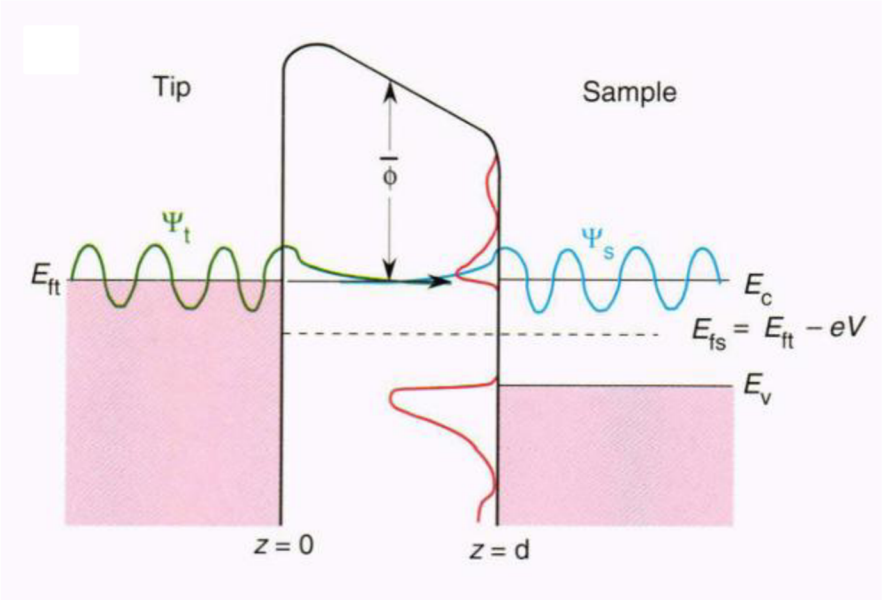

Figure 1.3: Schematic representation of the operational principles that drive a scanning tunneling microscope. Energy E versus distance z of a tunneling junction, where E_f is the Fermi level, E_v is the top of the valence, band E_c is the bottom of the conduction band, Ψ is the electron wave function, and Φ is the tunneling barrier height. The subscripts t and s refer to tip and sample. The red curves depict the electron density of states of the sample. Adapted from [36]

1.2.2. STM Operation Modes

The **Figure 1.4** represents a schematic scanning setup of a scanning tunneling microscope. A sharp tip made up of tungsten, iridium or platinum-iridium alloy, sharpened by chemical etching or mechanical grinding is mounted to a scanning device known as *xyz* scanner. The scanner allows to position in a three dimensional frame i.e. in x, y and z directions using piezoelectric actuators and can acquire a subatomic precision. The tunneling current I_t flows between the tip and the sample at a distance of several angstroms when a bias V_t is applied to the sample.

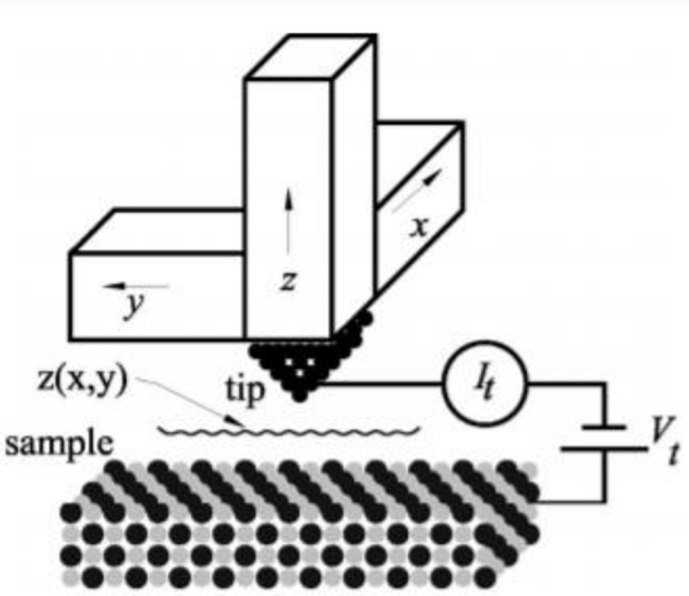

Figure 1.4: A schematic of a scanning tunneling microscope. Adapted from [17]

The tunneling current is used as a feedback signal in a z-feedback loop. Thus, images are captured at a **constant current mode or topographic mode**. This mode records the *z* position or the distance between the tip and the sample needed to maintain a constant tunneling current and surface topography images are produced by scanning the tip in the *xy* plane. The feedback controller maintains the constant tip-sample distance with high accuracy. Thus the scan speed is limited to a very large extent to avoid tip crashes and is adjusted according to the topographic features on the surface. [32], [37]

The imaging of atomically smooth surfaces can be more effectively captured at **constant height mode**, where the distance between the tip and sample is kept constant. The change in tunneling current is recorded at different positions on the sample. This process can be achieved by either switching off the feedback controller or scanning at a very high speed so that the feedback control cannot match the atomic corrugations on

the surface. But this mode has high chances of tip crash and huge amount of piezo creep can be observed due to fast scanning rate.

It is necessary to maintain the quality of the tip to achieve high spatial resolution which is determined by the tunneling current exponentially dependent on the tip-sample distance. The quality of the tip is its atomic structure and not the macroscopic curvature radius thus there is either a single atom at the tip apex or small cluster of atoms. The tunneling current flows between the projecting atom on the tip apex and the sample, thus the tips must be prepared efficiently through chemical etching. The structure of the tip apex can be viewed optically with the help of electron microscopes. [32], [37]

The STM operation does not require vacuum but is mostly operated under ultra-high vacuum (UHV) environments as it avoids contamination or oxidation of surfaces. This is necessary for obtaining high resolution imaging of the surface topography as surface oxidation reduces the conductivity of the surfaces and thus affects the tunneling current and causes problems in imaging. The UHV environment is achieved by incorporating the required materials and efficient pumping systems in the STM system. The materials and samples used inside the STM chamber are always checked to be vacuum compatible. The combination of oil-pumps, turbo pumps and ion pumps are attached to the instrument to achieve a pressure upto 10^{-11} mbar. [17]

1.3. Atomic Force Microscope

Even though STM is an asset to the field of surface science, it has its own serious limitations. The system relies on the electrical conduction of the sample material as it is based on the principle of tunneling effect between the tip and sample. Thus it can only

be used to analyse electrically conductive samples such as metals and semiconductors. And also in case of conductors, few materials cannot be studied under ambient conditions such as high-pyrolytic graphene (HOPG) and requires ultra-high vacuum environment. The ambient atmosphere can result in adsorption and desorption of atoms and molecules from surface, while UHV is a solution for clean and well-defined surfaces. A stable tunneling process across the vacuum gap is also hindered due to the mechanical and thermal vibrations caused between the tip and the sample. [17] Moreover STM technique relying on the detection of tunnelling current is limited to only conducting samples

These drawbacks of STM led to the development of atomic force microscope (AFM) by Binning, Quate and Gerber in 1986. During the operation of STM, it was noticed that there are significant atomic forces which act collaterally with the tunneling current and these forces could be used to gain atomic resolution on surfaces, hence AFM came into existence. This force microscope does not depend on the electrical conductivity of the sample hence can be used to image insulators as well. It can be used to image the surface without any surface preparation, thus does not required UHV conditions and can be operated in ambient conditions.

The key components and design of AFM is pretty much similar to STM except the probe tip is replaced with a cantilever or force sensor. It is not possible to study force effects in STM thus a sensor is needed for measuring forces between the tip and the sample. A force sensor is a spring which senses the tip-sample forces and is rigid in two axes and soft in third axis due to the cantilever beam geometry. The force sensor is characterized by different properties such as eigen frequency f_o, quality factor Q, stiffness k, and the chemical and structural composition of the cantilever tip.[17]

1.3.1. Operating Modes of AFM

The modes of AFM can be categorized into two groups: contact or static mode and dynamic or non-contact modes. The imaging signal in AFM is the acting force between the tip and the sample.

Static Mode (Contact Mode)

In this mode, the tip sample force is converted into the deflection of the cantilever. The tip apex of the cantilever is in direct contact with the surface, and the force either attractive or repulsive acting between the tip and the sample is counterbalanced by the elastic force generated by the cantilever deflection. The cantilevers need to be much softer than the bonds between the atoms of the tip and the sample to realize high sensitivity and the deflections should be larger than the deformations of the tip and the sample. [16], [17]

This mode can be carried out either at constant force or at constant average distance between the tip and the sample. In the constant force approach, a constant value of the cantilever bend and simultaneously the interaction force is provided by the feedback loop system. Thus the voltage applied to the z-scanner will describe the surface topography. In the constant distance or constant height mode, the tip moves at some arbitrary distance above the sample and the cantilever bend proportional to the interaction or applied force is recorded thus the image shows the spatial distribution of the tip- sample force.

The static mode can lead to a mechanical breakage of the tip or wear of the sample surface. It is not possible to measure small static deflections with good signal-to-noise

ratio. The chemical bonding forces responsible for the atomic resolution are mostly affected by the long range van der Waals forces. These challenges in static or contact mode could be overcome by operating in non-contact mode or dynamic mode. [16], [17]

Dynamic Mode (Non-Contact Mode)

In the dynamic mode, the cantilever has forced oscillations by mounting it on an actuator to provide an external excitation. As tip approaches the sample, the cantilever experiences an additional force due to van der Waals interaction with the surface. The two methods in dynamic or non-contact mode AFM are: amplitude-modulation (AM) and frequency-modulation (FM).

The cantilever is made to oscillate at a fixed amplitude and frequency which is close to the eigen frequency of the cantilever. As the tip approaches the sample, the oscillation changes the amplitude and the phase of the cantilever due to the elastic and non-elastic interactions. These amplitude changes are used a feedback signals. The AM mode is used widely as it is simpler to measure the amplitude at the eigen or operational frequency of the cantilever and a monotonic feedback signal is available. [17], [38]

The FM mode characterizes a cantilever with eigen frequency and spring constant which is subjected to a controlled positive feedback and vibrates at a constant amplitude. It is the most preferred AFM technique in ultra-high vacuum and has five operating parameters: the first three parameters i.e. spring constant, eigen frequency, quality factor are dependent on the type of cantilever used while the oscillation amplitude and frequency shift can be adjusted freely. In this mode the dissipative and non-dissipative interactions are separated which lead to increase in the driving amplitude oscillating the

cantilever and frequency shift respectively. High eigen frequencies and quality factors can provide good atomic resolution images at reduced sensitivity to external mechanical vibrations and good signal-to-noise ratio.

Both these modes were considered to be non-contact modes as the cantilever is positioned far away from the sample and the net force between the tip and sample is attractive. But later amplitude mode has been used at closer tip-sample distances in ambient conditions and resulting in repulsive tip-sample interactions thus called the Tapping mode. [17], [38]

1.3.2. Challenges Using AFM in Comparison to STM

The atomic resolution with STM or an AFM can be achieved when the mechanical vibrations between the sample and the tip is lower than the atomic corrugations on the surface. This can be made possible by enhancing the stability and vibration isolation of the system. The challenges faced in AFM is rooted in the controlling of the major parameter, the signal force while the parameter in STM i.e. tunneling current in vacuum shows a relative ease in obtaining atomic resolution.

The tunneling current is monotonic in nature which helps to control the distance between the tip and the sample through a feedback loop. It is not the case with signal force as it non-monotonous i.e. initially the force is attractive and then turns into repulsive when the atoms of the tip and sample come in contact. The plot of tunneling current (I_t) and tip-sample force (F_{ts}) as a function of distance (z) is represented in **Figure 1.5**. Secondly, the tunneling current is extremely short range and as it is strongly

distance dependent, it mainly comes from the single atom protruding the most from the tip. In contrast tip-sample force consists of strong long range interactions such as van der Waals and many other types, and the chemical forces provide very low magnitudes of atomic resolution. Third, it is easy to measure the pA to nA range tunneling current with a simple experimental setup and good signal-to-noise ratio while it is difficult to measure signal forces in pico to nanonewton range. [17], [39]

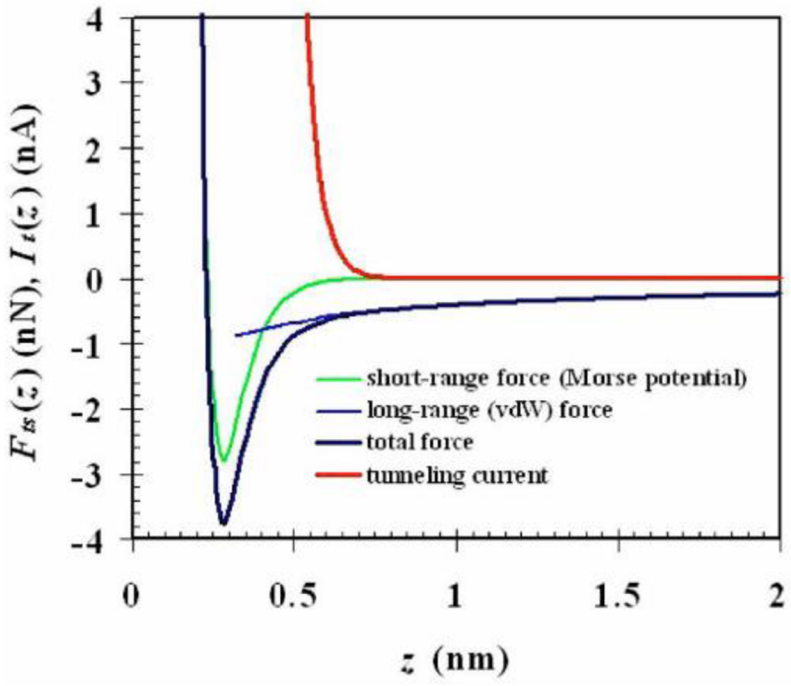

Figure 1.5: Plot of tunneling current I_t and force F_{ts} (typical values) as a function of distance z between center of front atom and plane defined by the centers of surface atom layer. Adapted from [17]

Initially, these problems led to hindrance in measuring atomic resolution images using AFM due to micro-machined silicon based cantilevers as it was only possible to detect deflection using optical methods. The ambient conditions also led to contaminations on

surface which made it difficult to measure the tip-sample force interactions. The development of qPlus and Kolibiri sensors with the force detector tips and in-built deflection sensors has led AFM to exceed the spatial resolution of STM. These quartz based sensors help to perform STM and AFM measurements in parallel with extreme stability and high signal-to- noise ratio. [39], [40]

2. One Dimensional Quinoid Based Polymers on Surfaces

Quinones belong to one of the most important classes of π-conjugated molecules with applications covering a broad spectrum ranging from chemistry to materials science, physics to biology, and engineering to medicine [41]–[44]. They act as remarkable ligands affording complexes of varying designs and applications in catalysis, molecular electronics and many other scientific areas [42], [43], [45], [46]. Since decades, para- and ortho- benzoquinonediimines (p- and o-BQDI) have been used for synthesis of different coordination (mono and bi-dentate) complexes due to their ease of access. The substitution of amine ($-NH_2$) groups at 2 and 5 positions of p-BQDI result in 2,5-diamino-1,4-benzoquinonediimines (**2HQDI**) which offers a drastic turn in coordination chemistry. **2HQDI** as a ligand merges the structural properties of both the o-BQDI and p- BQDI, resulting in formation of both mon-, bi-, bis-bidentate coordination complexes thus is more versatile than the other two [43], [45].

2,5-diamino-1,4-benzoquinonediimines (**2HQDI**) are particularly interesting because of the unusual distribution of their overall 12-π electrons system which can be described as two nearly-independent 6-π electrons subunits chemically connected through two C-C single bonds. This unique distribution (*i.e.,* the so-called "coupling principle") – first suggested 50 years ago based on theoretical studies of 12-π electrons quinones, was confirmed experimentally in 2003, giving rise to fascinating optical properties [43], [44]. Importantly, these quinones have attracted considerable interest as ligand in

coordination chemistry because their π*-orbitals can mix extensively with the valence d-orbitals of a metal center, allowing a full electron delocalization over both metal and ligand [47], [48]. Thus, the very rich and versatile behaviour of **2HQDI**s as ligand could be demonstrated for the preparation of mono and dinuclear complexes respectively, exhibiting valuable properties in several technological sectors [43], [48]. The ligand exists as two tautomers in solution at equilibrium, whose alternation occurs mutually via a fast intramolecular double proton transfer generating a structure of higher symmetry than the tautomers, thus directly altering the π-conjugation of the **2HQDI** molecule.[49] Although the **2HQDI** molecule was reported in 1887 [50], it has been rarely investigated in coordination chemistry mostly due to its low solubility and poor stability in different reactions unlike the N-substituted systems (N-alkyl or N-aryl) [45], [51]–[60].

The synthesis of nickel coordinated complexes (NiQDI) with **2HQDI** molecules as ligand has been reported, showing a stepwise formation of coplanar NiQDI polynuclear complexes with upto 3 units [48]. The absence of N-substituents on the ligand results in a unique behaviour leading to the formation of Ni-coordinated complexes in solution due to lack of steric hindrance. In solution, the oligomerization reaction takes place by consecutive deprotonation and metalation of **2HQDI** ligand yielding metal coordinated complexes where each ligand molecules is linked to the metal center through two covalent and two coordinate bonds. Thus the metal centers always attain the oxidation state of +II and the π-system of the bridging quinoid unit gets fully delocalized forming π-d delocalized systems [61]–[63].

The synthesis of **2HQDI** ligand has been described in **Appendix I**, as already reported in the literature [48] but synthesizing the starting compound first then followed by

quinone synthesis rather than using the commercially available reagent and also by replacing the base used previously. The ligand has been used to carry out oligomerization reactions in solution with transition metals such as Fe, Co and Cu following the synthesis procedure similar to nickel coordinated complexes (**Appendix I**). The solution polymerization reaction products have been characterized using Nuclear magnetic resonance (NMR) spectroscopy and Mass assisted Laser Desorption/Ionization (MALDI) to analyse the composition and mass of the acquired complex. The polymerization kinetics of the complex has been studied using Ultraviolet-Visible-Near Infrared Spectroscopy (UV-vis-NIR) to understand the successive metalation reactions in an organic solvent with time. The oligomer size depends on the solvents used for the complex formation as the process stops when the limit of solubility is attained [64]. The studies were not completely successful as the previously known Ni-coordinated complex [48], due to the formation of impure and less stable metal coordinated quinoid complexes in solution (see **Appendix I**).

The incapability of traditional polymerization technique to produce pure, stable individual transition metal coordinated quinoid oligomers pave the way to on surface polymerization approach under UHV conditions. The advantage of this approach is the possibility to synthesize long, flexible defect-free polymers and also tune the properties of these one dimensional long wires by changing either the metal center or the ligand [29], [65]–[69]. The ligand design plays an important role in this scenario as it is necessary to maximize the conjugation through coordination by keeping the π-systems almost coplanar.

The first part of on-surface synthesis focuses on synthesis of 1D H-bonded wires on Au(111) formed by the precursor molecule **2HQDI**. The synthesis procedure and on

surface characterization of the H-bonded wires have been discussed with further analysis in Cahlik *et.al.* [70]. The second part of on-surface synthesis and substantial focus of this chapter is to describe the formation of 1D coordination polymers on two different metal surfaces Au(111) and Cu (111), through codeposition of transition metals and **2HQDI** ligand. The MQDI (M=Fe, Co, Ni, Cr) wires show four-fold square planar coordination mode while Cu_2QDI afford a two-fold linear coordination. The coordination polymers have been characterized using STM and nc-AFM techniques and the properties of these coordination polymers have been studied further [71].

2.1. On Surface Synthesis of H-bonded Wires

(Figures and text sections have been adapted from [70] and modified according to the main text)

Contribution of the author: Deposition of molecules on surface and STM characterization.

The H-bonded 1D wires formed with **2HQDI** molecules can be considered as a paradigm to study nuclear quantum effects (NQEs) at low temperatures. There have been many studies previously both experimentally [72] and theoretically [73], demonstrating the impact of NQEs on the strength of hydrogen bonds. This effect can result in proton delocalization in the system thus altering their chemical properties [74]. The advancement in scanning probe microscopy has enabled to study proton transfer processes [75]–[79]; the high spatial resolution of single molecules with proper tip functionalization [31], [80] helped to study the concerted proton motion in water tetramers [81].

In this section, a H-bonded 1D molecular system has been synthesised on metallic surface and the concerted proton motion within this 1D system has been studied. A clean metallic Au(111) surface was obtained by repeated Argon ion sputtering and annealing cycles. The self-assembled molecular chains were formed by depositing single **2HQDI** molecules onto Au(111) substrate by sublimation from a home-built evaporator. The hydrogen bond formation in the 1D molecular wires can be attributed to the presence of imine (as H-acceptor) and amine groups (as H-donor) in the **2HQDI** ligand. The well-defined alternation of single and double bonds with respect to the position of the amine group hydrogen atoms may result in two isomeric π-conjugations in the 1D chain. The nuclear quantum effect described in the 1D system i.e. the concerted proton motion enhances the mechanical stability and thus modifies the electronic structure by forming new electronic in-gap states localized at the terminal positions of the 1D chain (as explained in Cahlik *et.al.* [70]).

Two different types of chains were observed depending on the synthesis process: straight or symmetric chains and canted chains. The straight chains were formed when the molecules were sublimed at a temperature of ~90-100 ^{0}C onto a cold sample held at 5K directly into the microscope head; then the sample was transferred to the chamber and left at room temperature for ~1 hour, later placed into the microscope head for measurement. The canted chains were formed by depositing the molecules sublimed at ~ 90-120 ^{0}C on a thermalized sample (~20-60 ^{0}C) and then transferring it to the microscope head.

The molecular chains were investigated at low temperatures (5K) under UHV conditions. The STM overview image in **Figure 2.1** show 3-100 nm long 1D symmetric chains assembled in directions independent of the Au(111) surface herringbone reconstruction,

unlike the coordination polymers discussed further. There are characteristic bright spots at the end of these chains (**Figure 2.1.b**) which are absent in the coordination polymers formed with the same ligand. The chains can be manipulated along the surface by contacting them at the end with the tip and moving it laterally. The consecutive lateral manipulations of a 1D straight chain are shown in **Figure 2.1.c**. The chains remain intact during the manipulation experiments and the bright spots also remain at their ends thus demonstrating a weak interaction with the metallic substrate but strong intermolecular interactions.

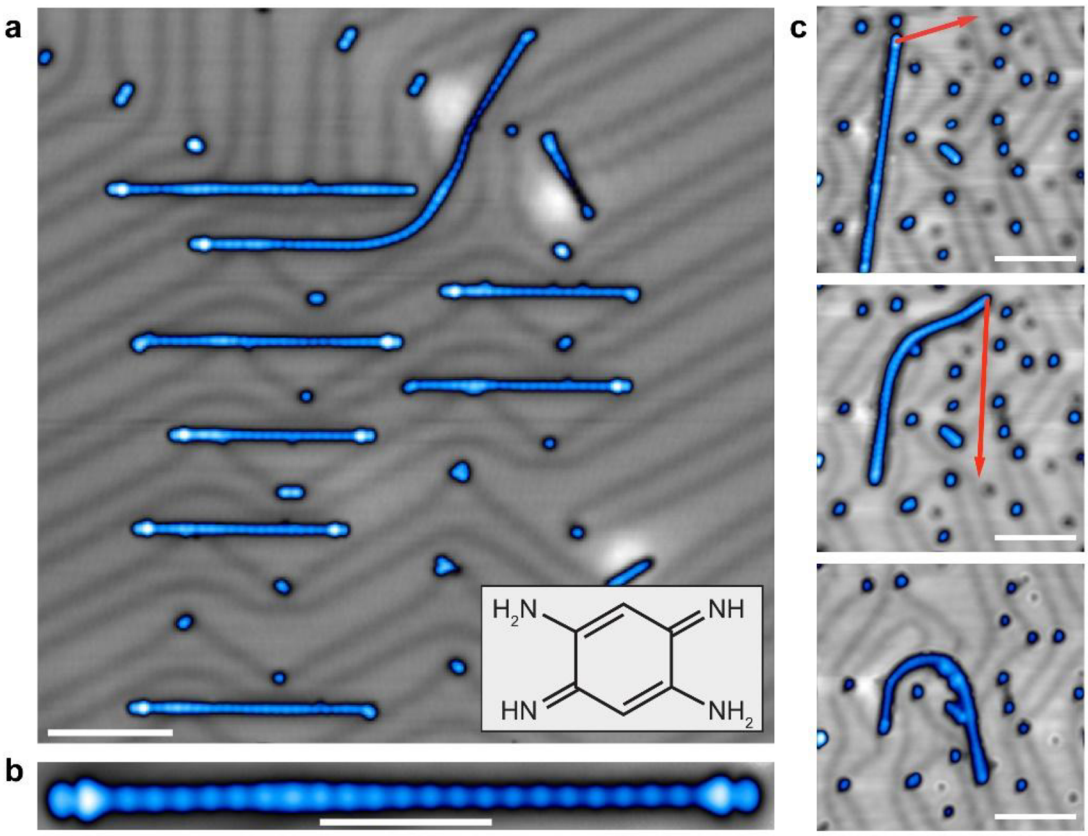

Figure 2.1: (a) Representative overview STM image of molecular chains and single molecule species. (50 mV, 10 pA, scale bar 10nm). Inset: 2,5 -diamino-1,4-benzoquinonediimine (**2HQDI**) structure. **(b)** Close-up STM image of the symmetric chain with characteristic bright spots at the ends. (30 mV, 5 pA, scale bar

5 nm) **(c)** From top to bottom: sequentially acquired STM images of chain manipulation experiment. Red arrows represent the probe movement after contacting the chain end (all images 100 mV, 10 pA, scale bars 10 nm). Adapted from [70]

The canted molecular chains are completely different from the symmetric chains in growth pattern and structure, **Figure 2.2.a**. They contain more defects and grow significantly along the herringbone reconstruction of the Au(111) surface, also lack the bright spots at the ends. Compared to the symmetric chains, the mechanical stability of the canted chains is really low thus lateral manipulation is prohibited and the chain splits into segments on moving with the tip (**Figure 2.2.b**).

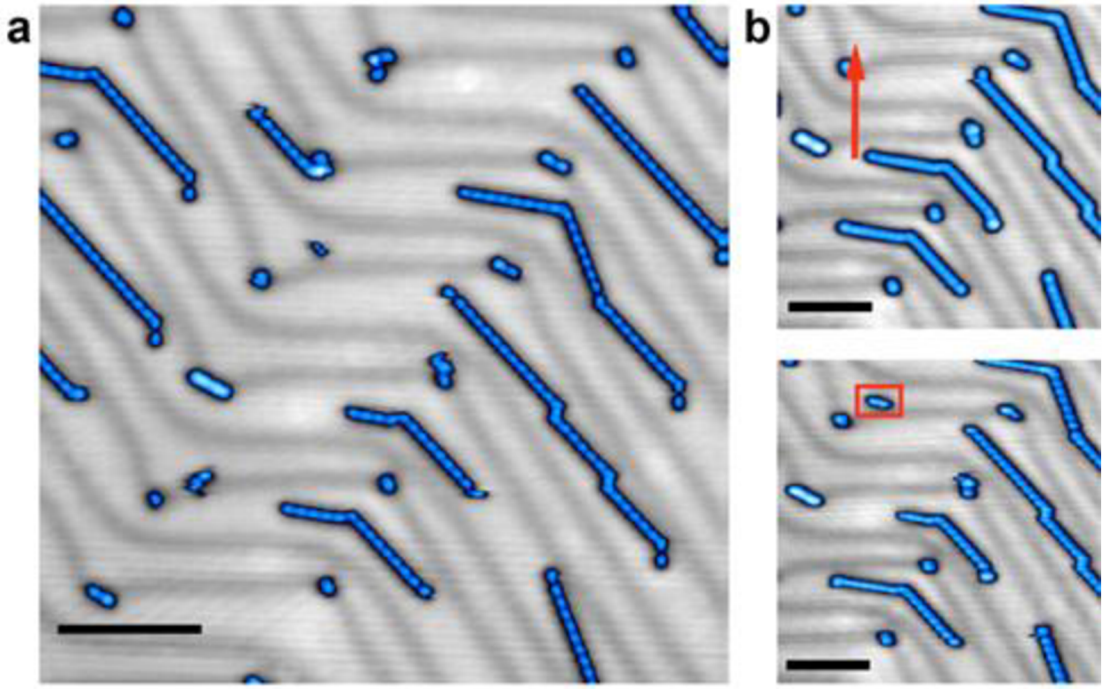

Figure 2.2: (a) Representative overview STM image of canted molecular chains. (140 mV, 20 pA, scale bar 10 nm) **(b)** STM images (140 mV, 20 pA) taken before and after manipulation experiment. Red arrows represent the probe movement after contacting the chain end (procedure detailed in Methods). Image on

the right side (after the manipulation) show apparent splitting of the chain into segments. Scale bars 10 nm. Adapted from [70].

The manipulation experiment methods and details have been mentioned in [70]. The mechanical properties of the two chains differ in the influence of proton tunneling on the hydrogen bonding between the molecular units of the 1D wires. There are individual molecular species on the substrate, which are distinct and situated on the elbows or kinks of the herringbone on the Au(111) surface. They have been identified as individual molecules consisting of an extra proton. The structure of the two different types of chains as well as the individual species has been investigated with the help of high resolution nc-AFM images with a CO functionalized tip. The synthesis and characterization experiments have been discussed in detail; the nuclear quantum effects which enhance the cohesion of relatively strong hydrogen bonding has been investigated theoretically (see Cahlik *et.al.* [70]).

2.2. On Surface Synthesis of Coordination Polymers

(Figures and text sections have been adapted from [71] and modified according to the main text)

Contribution of the author: Deposition of molecules on surface, STM/nc-AFM measurements and analysis.

The experiments as described in **Figure 2.3** were performed in a low temperature ultrahigh-vacuum system with combined STM/nc-AFM capabilities. As shown in the Scheme, two structurally different 1D coordination polymers (CP) with **2HQDI** molecules have been obtained: M-coordinated (M=Cr, Fe, Co, Ni) four-fold square planar CPs and Cu-coordinated two-fold linear CPs.

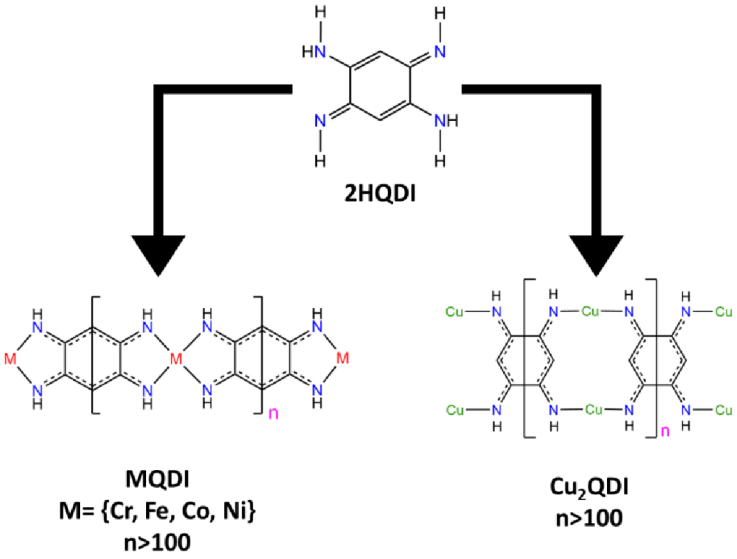

Figure 2.3: Scheme of on surface formation of structurally distinct four-fold coordinated **MQDI** (M=Cr, Fe, Co, Ni) wires and two-fold coordinated **Cu_2QDI** wires by dehydrogenative metalation of **2HQDI**.

2.2.1. Synthesis of Metal Coordinated Molecular Wires on Au(111)

A single-crystalline Au(111) substrate was prepared by repeated cycles of argon ion sputtering and annealing. The formation of **MQDI** (M=Cr, Fe, Co, Ni) wires was achieved by the codeposition of metal atoms and **2HQDI** molecules on Au (111). The metal atoms were deposited by an electron-beam evaporator on the substrate which was held at a temperature above the desorption temperature of the molecules (~ 400 ^{o}C). The **2HQDI** molecules were sublimed at 115 ^{0}C and codeposited along with metal atoms for 4 minutes.

The on surface synthesis allows synthesis of long metal coordinated wires comprising metal atoms and quinone molecules (**Figure 2.4**), as a result of dehydrogenation reaction on the surface similar to solution polymerization reactions mentioned previously.

The **FeQDI** wires follow the herringbone reconstruction lines of the Au (111) surface and the excess metal atoms are adsorbed on the ridges of the herringbone on Au (111) surface (**Figure 2.4.a**). The overview STM images of other metal coordinated chains, **CrQDI**, **CoQDI** and **NiQDI** also show similar lengths and structural characteristics on Au (111) (**Figure 2.4 b,e,f**). The lengths of these molecular wires exceed 100 nm, providing a new approach to overcome the limitations of achieving long polymers through traditional polymerization technique. The zoom-in STM images (**Figure 2.4.c,d,g,h**) of all the molecular wires on Au(111) have the same width, show similar periodicity and structural arrangement.

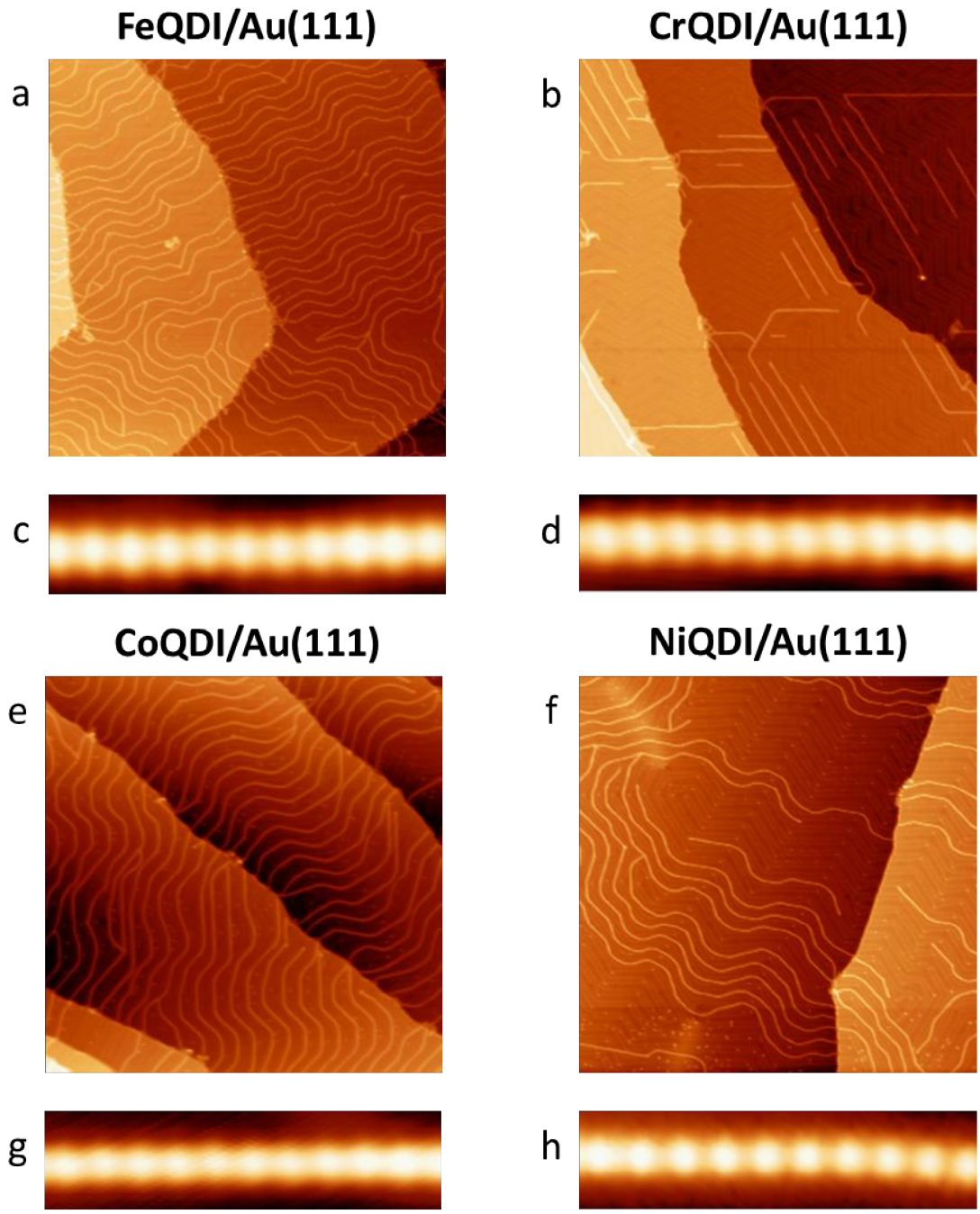

Figure 2.4: STM images of **(a) FeQDI (b) CrQDI (c) CoQDI (d) NiQDI** wires on Au(111). The overview images are 200 × 200 nm² and the zoom-in images are 8 × 2 nm². Imaging parameters (bias voltage, tunnel current set point): (a) **FeQDI** (500 mV, 10 pA); (b) **CrQDI** (100 mV, 30 pA); (c) **FeQDI** zoom-in (-200 mV, 23 pA); (d) **CrQDI** zoom-in (30 mV, 10 pA); (e) **CoQDI** (350 mV, 10 pA); (f) **NiQDI** (100 mV, 42 pA); (g) **CoQDI** zoom-in (-400 mV, 32 pA); (h) **NiQDI** zoom-in (100 mV, 42 pA). Adapted from [71]

The flexibility of the molecular wires have been demonstrated by performing lateral manipulation experiments on Au(111) substrate with the help of STM tip. The molecular wires can be manipulated by different interactions with the tip and folded into different shapes, as shown in **Figure 2.5**; revealing the weaker interactions of the 1D wires with the substrate.

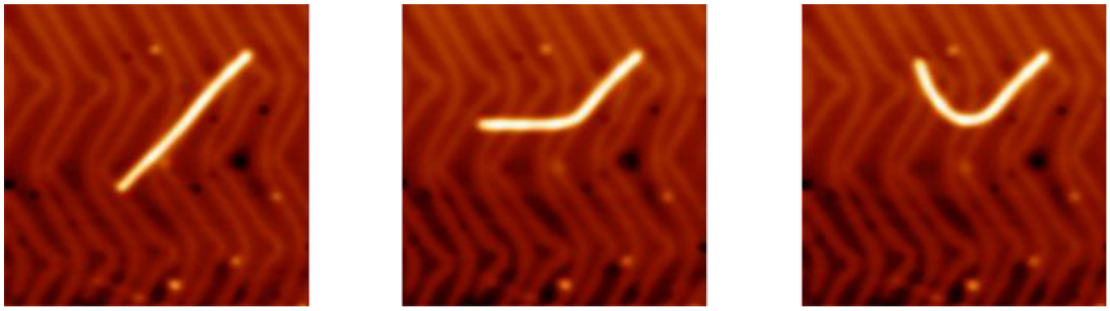

Figure 2.5: From left to right: sequentially acquired STM images of chain manipulation experiment of **FeQDI** wire on Au(111). Scanning Parameters:(300 mV, 20 pA, 40x40 nm^2). Adapted from [71]

2.2.2. Synthesis of Metal Coordinated Molecular Wires on Cu(111)

The formation of metal-quinone coordinated molecular wires on Cu(111) was necessary to study the dependence of the structure of these wires on the nature of the substrate. The STM topography of **MQDI** wires were similar on Au(111), thus only one system i.e. **FeQDI** molecular wires have been studied for comparison. A single-crystalline Cu(111) substrate was prepared by repeated cycles of argon ion sputtering and annealing. The **FeQDI** wires on Cu(111) were formed by the same process as on Au(111), as mentioned previously in **Section 2.2.1**. The **Cu_2QDI** wires (as shown in **Figure 2.3**) were formed

by deposition of **2HQDI** molecules at room temperature on Cu (111) by sublimation at 115 °C and then subsequently annealing the sample upto ~250 °C for 10 minutes.

The overview STM images of **FeQDI** and **Cu_2QDI** wires on Cu(111) show more branching and follow specific directions of the substrate, **Figure 2.6.a,b**, in comparison to the molecular wires on Au(111) where branching between the wires occur rarely. The previous studies on the growth of inorganic and organic 2D materials [82], [83] on surfaces attributes to the kinetically controlled growth characteristics on Cu(111), thus resulting in higher rates of branching among the 1D molecular wires. This growth mechanism also can be associated with higher diffusion barriers on Cu(111) substrate than on Au(111). The zoom-in STM images (**Figure 2.6.c,d**) show that the **Cu_2QDI** wires are comparatively wider than the **FeQDI** wires on Cu(111) as well as the **MQDI** wires on Au(111). The periodicity along the **Cu_2QDI** is evidently smaller than the other molecular wires, which has been substantiated with the nc-AFM observations described further.

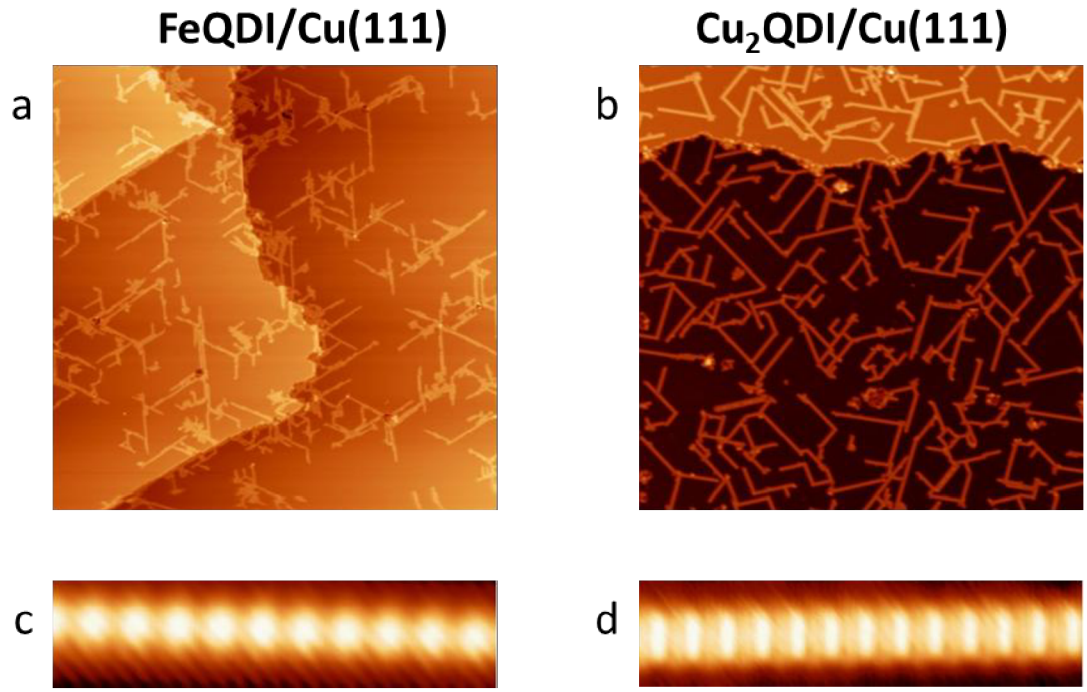

Figure 2.6: STM images **(a)** FeQDI on Cu(111) and **(b)** Cu_2QDI wires on Cu(111). The overview images are 200 × 200 nm² and the zoom-in images are 8 × 2 nm². Imaging parameters (bias voltage, tunnel current set point): (a) (500 mV, 20 pA); (b) (1.2 V, 10 pA); (c) (-200 mV, 50 pA); (d) (300 mV, 30 pA). Adapted from [71]

2.2.3. Characterization of On Surface Coordination Polymers

The structure of the **Cu_2QDI**, **FeQDI** chains on Cu(111) and **FeQDI** wires on Au(111) has been characterized with the high resolution frequency shift image obtained with a CO modified tip (**Figure 2.7**). The nc-AFM images of **FeQDI** wires exhibit a four-fold square planar coordination (**Figure 2.3**) on both Au(111) and Cu(111), **Figure 2.7.a,b**, irrespective of the nature of the substrate. The Fe atom coordinates head-to-head

between the two ligands showing a clearly visible "x-like" contrast feature between the quinone ligands. On the contrary, **Cu_2QDI** wires on Cu(111) show two-fold linear coordination with two Cu atoms between two ligands (**Figure 2.3**); each Cu atom links to the ligands arranged side-by-side through nitrogen atoms thus exhibiting a different structural contrast, clearly represented in **Figure 2.7.c**. In **Cu_2QDI** wires, coupling principle has been effectively described as the bridging ligand can be seen as two nearly-independent subunits with six π electrons each, connected through two C-C single bonds chemically. This results in the formation of electronically independent 12-membered macrocycles with 12 π electrons of the ligand, preventing full electron delocalization over the wire.

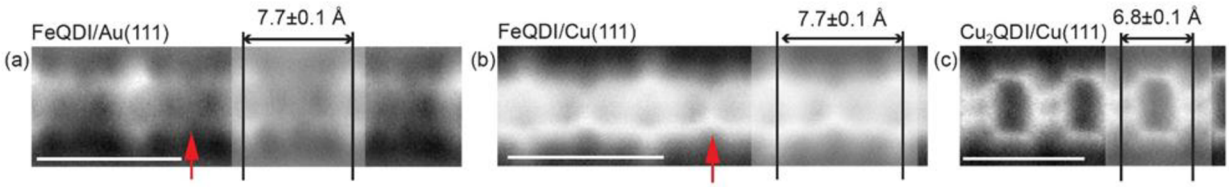

Figure 2.7: High resolution constant height nc-AFM images with CO modified tip of **(a) FeQDI** wires on Au(111) **(b) FeQDI** wires on Cu(111) and **(c) Cu_2QDI** wires on Cu(111). Both (a) and (b) exhibit the same characteristic "x-like" contrast feature (marked by red arrows) between adjacent molecular units and same lattice periodicity, clearly distinct from the contrast and the periodicity between the neighboring molecules in **Cu_2QDI** wires. [Scale bars: 1 nm; Aosc = 50 pm]. Adapted from [71]

The different structural arrangement of the metal atoms and ligands result in smaller periodicity along the wire for **Cu_2QDI** wires (6.8 ± 0.1 Å) whereas the periodicity for **FeQDI** wires is 7.7 ± 0.1 Å. The possibility of N-N bonding between the ligands can be eliminated as it would have resulted in a lower periodicity (5.7 A⁰ from DFT) along the

wire. The AFM simulations (**Figure 2.8**) of **FeQDI** on Au(111) and **Cu_2QDI** on Cu(111) produced using probe particle model [84] clearly resemble experimental AFM contrast. The structures of these molecular wires have been established with the help of total energy DFT simulations and the calculated lattice vectors are consistent with the experimental results in [71].

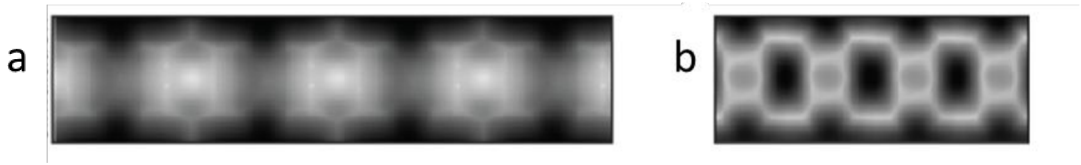

Figure 2.8: Simulated AFM images of (a) **FeQDI**/Au(111) (b) **Cu_2QDI**/Cu(111) coordination polymers. Adapted from [71] (Image Courtesy: Martin Ondraček)

The dehydrogenation reaction of **2HQDI** molecules and the simultaneous formation of metal coordinated molecular wires on surface have been further supported with XPS measurements in [71]. The XPS measurements have been carried out for native **2HQDI** molecule on the surface as well as **FeQDI**, **NiQDI** wires on Au(111) and **Cu_2QDI** wires on Cu(111) surface. It clearly denotes that all the nitrogen atoms of the ligand involved in the formation of the metal coordinated polymers have identical chemical environments, thus also excludes the possibility of hydrogen bonded wires. The periodicity in these 1D wires is also an indication of metal-coordination as H-bonded wires have a larger periodic distance, as investigated in [70].

The coordination mechanism of **FeQDI** and **Cu_2QDI** wires have been analysed theoretically with the help of DFT calculations of free standing polymers [71]. The

calculated projected density of states [71] show that in case of FeQDI wires, more d-orbitals are involved in rehybridization with the p-orbitals resulting in four-fold coordination [48] while in **Cu_2QDI** chain only s and d_{yz} orbitals hybridize with the p orbitals of the nitrogen atoms, hence is two-fold coordinated. The electrostatic potential maps [71] help to analyse the oxidation states of the metal atoms in the polymer wires; a larger charge transfer in **FeQDI** wire results in +II oxidation state while Cu is in +I oxidation state in **Cu_2QDI** wire. The theoretical studies certainly concede the experimental results and confirm that the 1D polymers formed on the surface exhibit π-d conjugation.

The most remarkable feature is the possibility to synthesise structurally and electronically similar **FeQDI** wires on both Au(111) and Cu(111) surfaces, while it has not been possible to synthesise **Cu_2QDI** wires on Au(111) by the electron beam evaporation of Cu metal. This can be noted as the favorable diffusion of Cu adatoms into the bulk of the Au single crystal.

2.2.4. Aromaticity Predictions in the Coordination Polymers

The aromaticity of the ligand and metal conjugated rings in the 1D chain has been investigated by means of various aromaticity indices. The aromaticity predictions based on magnetic criteria, such as the nucleus-independent chemical shift (NICS) have been analysed for both the free standing 1D chains **(Figure 2.9)**: **FeQDI** and **Cu_2QDI**. In **FeQDI** molecular wire, the NICS values are negative (-25.7 ppm and -17.5 ppm respectively) for the C_6 ring of the ligand as well as the five membered ring containing

the metal, thus exhibiting aromatic character. The negative value indicates a diatropic ring current in presence of a magnetic field. In **Cu_2QDI** chain, the C_6 ring of the ligand and the 12 membered macrocycle are both antiaromatic in nature, with positive NICS values (+8.6ppm and +6.6 ppm respectively) signalling paratropic ring current. It is necessary to note that these values may not be free from the influence of metal centres which in some cases can cause unreliable predictions.

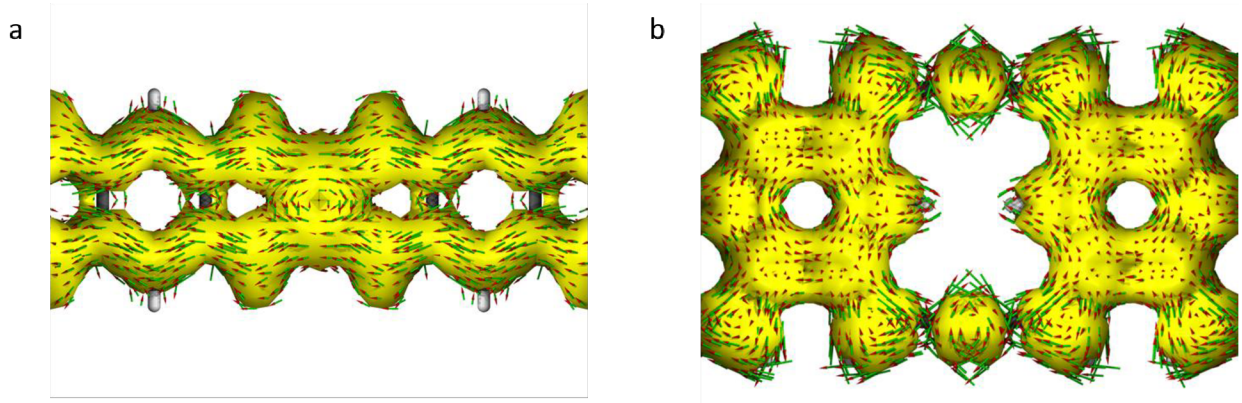

Figure 2.9: (a) ACID plot of **FeQDI**/Au(111), black arrow indicating the clockwise direction of current density vectors for better clarity. **(b)** ACID plot of **Cu_2QDI**/Cu(111), black arrow indicating the clockwise direction of current density vectors for better clarity. The molecular planes are placed perpendicular to the magnetic field vector. Small green arrows are computed current density vectors. Adapted from [71] (Image Courtesy: Adam Matěj)

To study the delocalization of the electrons in the 1D chains, the anisotropy of the current induced density (ACID) [85] in the **FeQDI** and **Cu_2QDI** chains have been analysed **(Figure 2.10)**. The ACID isosurface of the **FeQDI** chain show current density vectors plotted in the clockwise direction indicating a diatropic ring current flowing along the 1D polymer, confirming the aromatic behaviour in agreement with the NICS

values. In contrast to **FeQDI**, the ACID plot and anticlockwise current density vectors of **Cu_2QDI** chain exhibits paratropic current and thus antiaromaticity, in analogy with the NICS data. But the current density vectors are clearly seen as cyclic in nature separately for both the C_6 ring of the ligand as well as the 12 membered macrocycle, hence demonstrating that individual delocalized macrocycles form the backbone of the 1D **Cu_2QDI** chain.

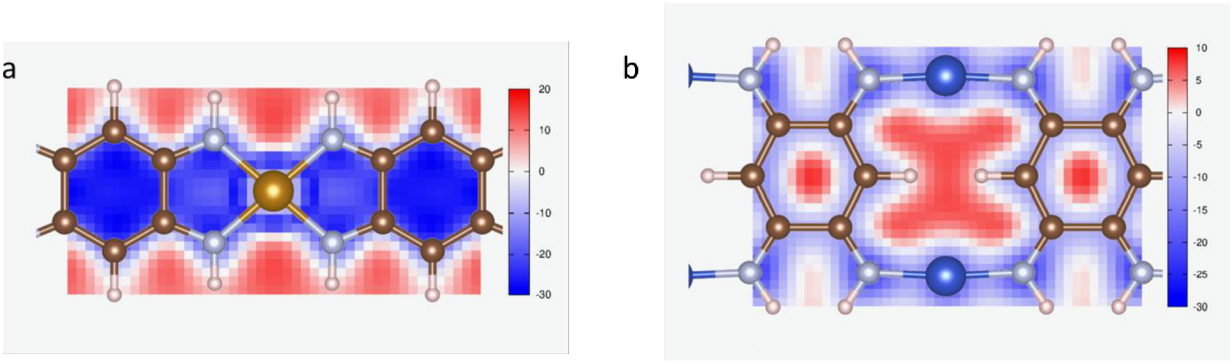

Figure 2.10: (a) NICS grid of **FeQDI**/Au(111) **(b)** NICS grid of **Cu_2QDI**/Cu(111). Adapted from [71] (Image Courtesy: Adam Matěj)

The bond scheme representing the resonating macrocycle structures of **Cu_2QDI** chain is shown in **Figure 2.11**. This cyclic delocalization of electrons is absent in the **FeQDI** chains, as the current density vectors are not purely circular on the ligand ring, thus no formation of macrocycles. The ACID plot of **FeQDI** chain reveals the presence of two decoupled delocalized π-d electronic systems which has been depicted in **Figure 2.3** for **MQDI**. The decoupling has been confirmed by the alternating large bond length values within the C_6 ring of the ligand [71].

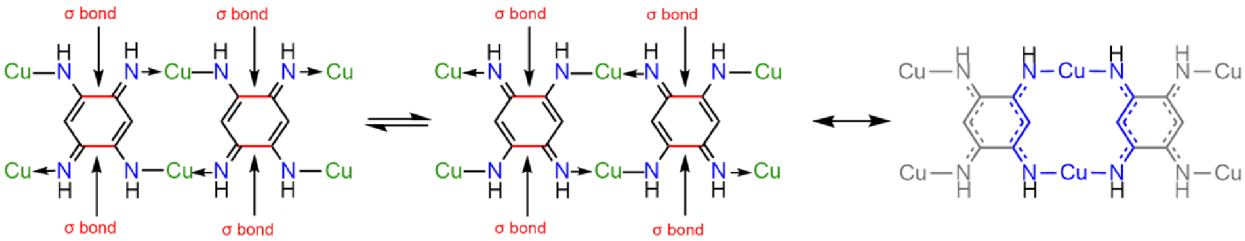

Figure 2.11: Scheme depicting the bonds and resonating structures of the 12 membered macrocycle in **Cu_2QDI** wires on Cu(111). Adapted from [71] (Image Courtesy: Olivier Siri)

Another aromaticity index, the harmonic oscillator model of aromaticity (HOMA) [86] has been calculated based on bond equalization [71] thus providing a structural concept of aromaticity. The HOMA values for C_6 ring of the ligand in **FeQDI** and **Cu_2QDI** are 0.4864039 and -0.241255 respectively, characterizing aromatic (**FeQDI**) and antiaromatic (**Cu_2QDI**) nature in correspondence to both NICS and ACID data. However, this indicator is applicable only for hydrocarbons consisting of some of the heteroatoms (N,O,P), thus cannot be applied to the metal containing rings in both the 1D chains due to the unavailability of metal-bond parameters.

For understanding the aromaticity of conjugated metallacycles, Mauksch and Tsogoeva have worked out the frontier π-orbital topology rule:

"The metallacycle is aromatic (antiaromatic) when the number of π-MOs is even and the π-HOMO is of Möbius (Hückel) topology-and vice versa when the number of π-MOs is odd." [87]

The nature of aromatic stabilization in metallacycles is related to the bonding between the transition metals and the adjacent atoms resulting in two different topologies of π-d orbital conjugation: π-type (Huckel) topology involving d_{yz} metal orbital and δ- type

(Mobius) topology involving d_{xz} orbital. The 12-membered metallacycle in the **Cu_2QDI** chain involves the conjugation of two d_{yz} metal orbital of Cu with the p orbitals of N atom from the calculated projected density of states [71], thus the conjugation can be considered as π-type or Huckel topology. In the context of the above mentioned rule, the 12-membered metallacycle in the **Cu_2QDI** chain consists of 8 π-MOs (even) and π-HOMO is of Huckel topology, hence the metallacycle is antiaromatic in nature; clearly in agreement with the NICS and ACID analysis. To note, this rule is applicable for the metallacycles whose number of π-electrons is equal to the number of members in the ring [88].

2.3. Conclusion and Perspectives

This chapter hence presents a unique approach to synthesise long, flexible and defect-free 1D metal coordinated polymers with π-d conjugation. The codeposition of **2HQDI** molecule and various transition metal atoms (Fe, Co, Ni, Cr, and Cu) on metal surfaces under UHV conditions overcome the limitations of solubility and purity in traditional solution polymerization techniques. It has been possible to investigate and demonstrate the coordination modes and structure of the 1D polymers through high resolution STM/nc-AFM imaging and theoretical calculations. The **MQDI** wires (M=Cr, Fe, Co, Ni) show a four-fold coordination mode with the quinoid ligand while Cu adopts a linear two fold coordination mode with the nitrogen atoms of the ligand. The electronic states of **MQDI** wires delocalize fully over the metal and ligand forming π-d systems while **Cu_2QDI** wires are formed by electronically independent antiaromatic 12-membered macrocycles with two metal centres preventing full electron delocalization over the wire. The anti-aromatic nature has been investigated theoretically with the help of various

aromaticity predictions such as NICS and ACID plots. The scanning probe microscopy techniques will help to further study the magnetic and electronic properties of the individual polymers on surfaces under UHV conditions. It is also possible to study the charge transport through the 1D wires by conducting lifting experiments and also study the switching of molecules in the presence of light, magnet or any other conditions.

3. Polyferrocenylenes on Ag (111): Synthesis, Conformational and Electrical Transport Properties

(Figures and text sections have been adapted from [89] and modified according to the main text)

Contribution of the author: Deposition of molecules on surface, STM/nc-AFM measurements and analysis.

The early 1950s witnessed the tremendous development of organometallic chemistry with the discovery of the compound **ferrocene**. The synthesis of ferrocene by Kealy and Paulson in 1951, and independently by Miller, Tebboth, and Tremaine, led to the emergence of a new class of molecules called **metallocenes** [90], [91]**.** These compounds consist of an organometallic sandwich structure with a metal centre bound to two planar cyclopentadienyl (Cp) anion rings ($C_5H_5^-$). Initially the metal centres were 3d transition metals, thereafter the family of metallocenes has extended to 4d and 5d metals such as ruthenium and osmium and also several other π-bonded aromatic ring systems such as cycloheptatrienyl or benzene cycles in the structure [92].

The synthetic and structural capabilities of the metallocenes have been documented for their diverse properties in potential areas such as catalysis, various oxidation-reduction reactions, synthesis of metal based structures and polymers; recent applications include organic and molecular electronics as well as spintronics due to their built-in spin

functionalities ensuring high device efficiency [93]. The electronic and magnetic properties of metallocene structures can be tuned by changing the metal center, by linking different metallocenes or by oxidation of the molecules.

Metallocenes and its derivatives have been proven as ideal systems to study the intermetal interactions in the complexes [94]. The metal atom positioned perpendicular to the aromatic ring plane binds to the p-electrons of the ring by donating its outer d-electrons. The prototype metallocene i.e. **ferrocene** shows the pp-dp type of bonding mechanism with an iron atom between the two parallel Cp rings in a sandwich structure. The Cp rings have an inter-ring distance of ~3.3 A^0 and can rotate freely to a great extent thus form eclipsed and staggered conformations under different conditions [95], [96]. The compound easily sublimes above 100^0 C thus making it an extraordinary precursor molecule for on surface reactions under ultra-high vacuum (UHV) [93].

The valence-shell electrons of the compound are paired hence ferrocene molecule is diamagnetic in nature. The even number electron structure i.e. 18e metal center as compared to other odd number electron structures such as cobaltocene, magnocene etc. attributes to the robustness of the ferrocene molecule. Out of the total electrons involved in bonding, 12 electrons populate the strongly bonding orbitals and rest six electrons occupy the non-bonding orbitals. The non-bonding electrons in the high energy orbitals provide a very strong configuration which establishes the redox properties as well as many other chemical properties of the ferrocene molecule. The p-electrons of all the carbon atoms participate together in the bonding pattern, thus there are no individual metal-carbon bonds [97].

Since 1960's, a large number of studies have been conducted on the synthesis of oligomeric ferrocenes and their thermal and electrical properties. 1,1'-oligomeric

ferrocenes from biferrocene (consisting of 2 ferrocene units) to sexiferrocene (6 units) have been formed using different reaction procedures and precursor compounds. Mainly the precursor compounds have been halogen containing ferrocenes and the oligomerization process proceeds by Ullmann reaction under different experimental conditions [98]–[101]. Iodoferrocene was considered to be one of the extremely reactive compounds in Ullmann reaction, producing a very high yield [100], [102].

The ferrocene units in the ferrocene oligomers interact with each other resulting in the formation of mixed-valence states with the coexistence of Fe(II) (ferrocene) and Fe (III) (ferrocenium ion) within the same molecule [103]–[105]. The mixed-valence complexes provide a platform to study the intramolecular internuclear transfer, thus understand the rates of electron transfer and other properties in the solution redox processes [103], [106]–[108].

A diverse variety of ferrocene oligomers and polymers have been synthesized by various methods using different precursor molecules [98], [99], [101], [109]–[112]. The first category is the presence of conjugated spacer groups in the ferrocene oligomer, where the chemical structure and length of the spacer group affect the electronic interactions between the ferrocene units thus influence the physical properties of such ferrocene oligomers and polymers [105]. The bridging group between the ferrocene centres lead to different functionalities and chemical properties. The second category is synthesis of ferrocene polymers by combining the electron donating ferrocene moieties to electron accepting groups resulting in fluctuating electronic structures. The third category is completely a different one, called the polyvinylferrocenes where an alkyl chain or allyl chain polymer contains ferrocene as substituents or pendant moieties, thus the interaction between the ferrocene units is completely inhibited [113], [114].

The most interesting category of ferrocene conjugated polymers is the main chain unsubstituted ferrocene containing polymers [115], [116] called the **poly(1,1'-ferrocenylene) or polyferrocenylenes (PFc)**, as shown in **Figure 3.1.** They are an attractive target owing to their phenomenal properties due to the short distance between the directly bonded ferrocene units through the covalent bonding between the adjacent Cp rings [117]. They show a very significant redox behaviour caused by the electron exchange between the ferrocene centres in the main chain unlike the polyvinylferrocenylenes with pendant ferrocene molecules [118], [119]. The through-electronic bond interaction in polyferrocenylenes result in higher bulk conductivity with electrical conductance values in the range 10^{-14} and 10^{-2} S cm^{-1}, than the systems consisting of non-interacting ferrocene and ferrocenium units such as the polyvinylferrocenes [120], [121]. These conductance values also depend on the method of chemical synthesis, crystallinity of the polymer, homogeneity of the system and doping processes [99]. But the conductivity is lower than other organic conducting polymers such as polyaniline, as the charge is localized on the metal sites in polymers containing ferrocenes in the main chain.

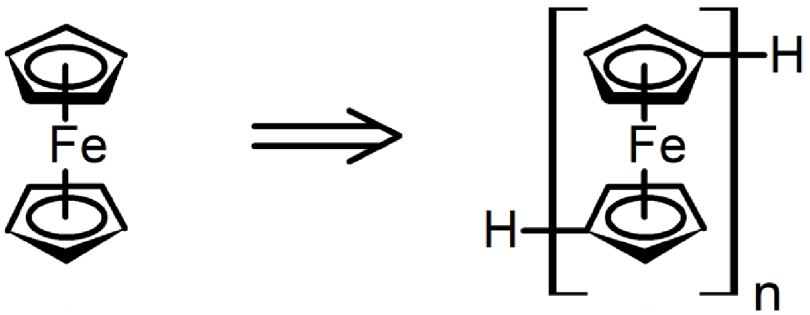

Figure 3.1: Scheme of structure of **polyferrocenylenes** (PFc). Adapted from [89]

There have been several attempts and developments in the synthesis of polyferrocenylenes after Korshak and Nesmeyanov *et.al.* described them for the first time in the early 1960's [122]. A large number of polymerization reactions using different monomers were proposed but most of the polymers synthesized were low weight, insoluble and impure. The impurities or substituents in the polymer result in higher molecular weight up to 7000- 10000 Da [123], [124]. It is difficult to synthesize pure high molecular weight polymers with traditional polymerization techniques as there is a decrease in solubility with the increase in degree of polymerization, with maximum up to 4600 Da (around 25 units) for the most crystalline polymer but difficult to separate into single polymers as known in solution polymerization [125].

The dilemma to synthesize pure individual polyferrocenylene chains has been solved in the following sections with the approach of on surface polymerization under ultra-high vacuum conditions. This mode of synthesis has helped to overcome the issues of solubility, purity and controlled synthesis of PFcs thus long 1D PFc polymers can be grown on surfaces and individually characterized with scanning probe microscopy (SPM) techniques [20], [26], [65], [126]–[129].

An extensive research has been conducted on adsorption of metallocene and metallocene based molecules and structures on surfaces, both experimentally and theoretically [130]–[134]. In this framework, the adsorption of single Fc molecule as well as Fc derivatives on different surfaces has been studied in detail. It is necessary to understand the intermolecular interactions in ferrocenes, their electronic properties and the nature of interaction with the substrate to form self-assembled structures on the surface. The functional groups introduced in the ferrocene molecules can determine the dimension of the self-assembled structures [128], [130], [135]–[137]. Different ferrocene derivatives

have shown potential application in molecular thin film-based devices due to their redox activities. The adsorption of such molecules on surfaces result in electronic modifications thus gains a considerable attention in molecular electronics [118], [136], [138]. A large number of two dimensional patterns have been achieved on the surface with various ferrocene derivatives [139], [140]. Even one dimensional growth of Fc derivatives on HOPG have been studied using ambient AFM [141], but pure 1D polyferrocenylenes as addressed further has not yet been realized.

The Ullmann coupling of organic dihalides on metal surface has been a great effort towards on surface polymerization reactions [142]. In this context, haloferrocene molecules were thought to act as reliable precursors to form ferrocene polymers on Ag(111) surface, similar to wet chemistry experiments. To note, the commercially available 1,1'-dibromoferrocene and 1,1'-diiodoferrocene are too volatile molecules due to low sublimation temperatures of ferrocene molecules, thus it is difficult to deposit on surfaces under UHV conditions. 1,1'''-dibromo-1,1''-biferrocene [143], a comparatively heavier molecule than other two, do not remain adsorbed on the Ag(111) surface during the polymerization attempts by thermal annealing. The behaviour of 1,1'''-diiodo-1,1''-biferrocene (**Fc_2-I_2**) was completely differently and led to the successful formation of long polyferrocenylene nanowires **(Figure 3.2)** on Ag(111) surface, as discussed further. The synthesis procedures of the precursor molecules are discussed in Supplementary information [89].

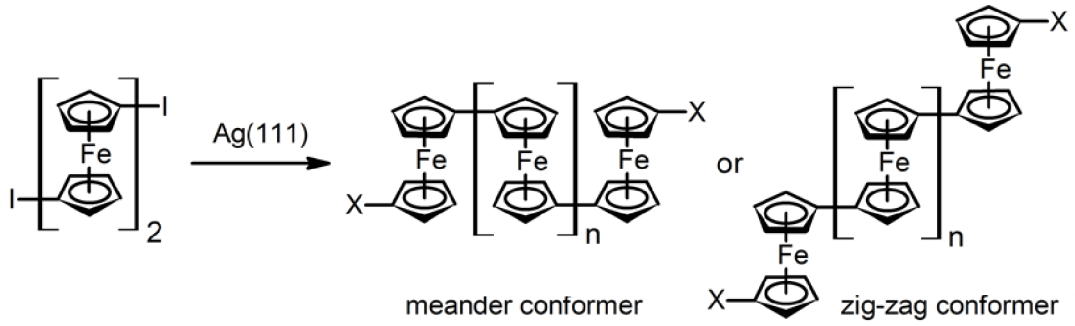

Figure 3.2: Scheme of on surface synthesis of **polyferrocenylene** on Ag (111) surface. Adapted from [89]

3.1. Deposition and Characterization of Fc_2-I_2 Molecules on Ag (111) Surface

The precursor molecules **Fc_2-I_2** were deposited by the process of sublimation using E-beam evaporator onto clean Ag(111) surface. The self-assembly of molecular adsorption was characterized by STM imaging. The molecules formed islands on the terraces **(Figure 3.3.a)** and along the step edges of the surface **(Figure 3.3.b)**. The individual molecules in the islands were resolved as double protrusions under constant height scanning mode **(Figure 3.3.a)**, each protrusion resembling a ferrocene unit of the molecule.

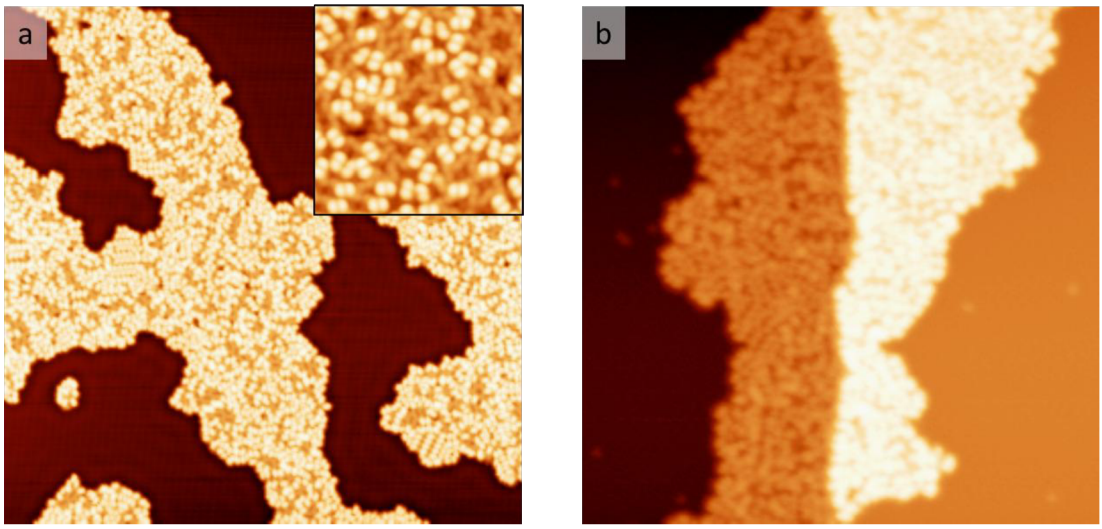

Figure 3.3: Fc_2-I_2 on Ag(111). **(a)** STM image of **Fc_2-I_2** islands on surface. **(b)** STM image of **Fc_2-I_2** islands along the step edges. Scanning Parameters: (a) (500 mV, 10 pA, 100 × 100 nm^2); (b) (500 mV, 10 pA, 50 × 50 nm^2).

The distribution of molecules in the islands on the surface **(Figure 3.4.a)** is mostly disordered **(Figure 3.4.b)**; however some islands also show ordered molecular stacking **(Figure 3.4.c)**. The remaining terraces of Ag(111) surface is mostly clean, which implies that the molecules did not lose their iodine atoms on deposition.

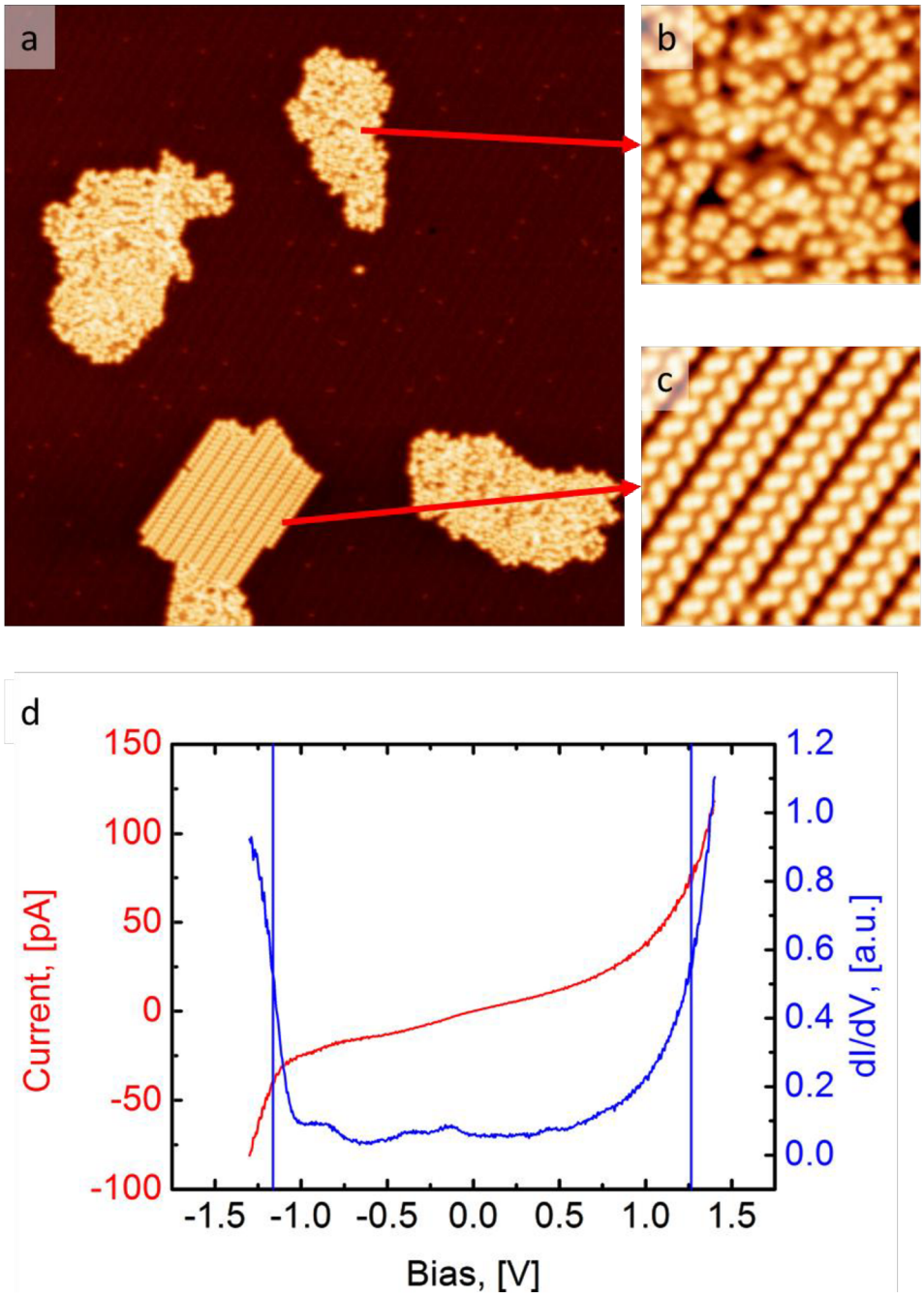

Figure 3.4: Fc_2-I_2 on Ag(111). **(a)** STM image of **Fc_2-I_2** islands on Ag(111) surface. **(b)** Disordered phase in the island. **(c)** Ordered phase in the **Fc_2-I_2** islands. **(d)** I/V (red curve) and corresponding dI/dV (blue curve) taken over **Fc_2-I_2** island. Vertical blue lines highlight the band gap of ~2.4V on the molecules before reaction. Scanning Parameters: (a) (500 mV, 10 pA, 100 × 100 nm^2); (b, c) (500 mV, 10 pA, 10 × 10 nm^2). Adapted from [89].

Apart from the structural characterization, an I/V curve and corresponding dI/dV curve were measured with a metallic STM tip on the molecular islands. The vertical blue lines, **Figure 3.4.d**, clearly show the bandgap of ~ 2.4 eV for the **Fc_2-I_2** molecules.

3.2. Formation of Polyferrocenylene Nanowires

The molecules undergo deiodination upon thermal annealing of the substrate, consequently resulting in C-C covalent bonding of the radicals via Ullmann coupling to form polyferrocenylene (PFc). The ferrocene polymerization on Ag(111) surface can be attributed to annealing temperatures and time, **Figure 3.5**. The PFc nanowires formation starts as the substrate is annealed for 10 minutes at ~400K, but the system also shows the presence of huge number of disordered ferrocene clusters which have not undergone deiodination yet (**Figure 3.5.a**). At the same temperature, annealing for longer time (20 minutes) resulted in the deiodination of all the ferrocene clusters and their polymerization to form PFc (**Figure 3.5.b**). The post annealing morphology of the Ag(111) surface at ~420K also show a large amount of iodine adatoms which were released during the reaction. On increasing the temperature to ~425K, Ag(111) surface was found to be clean indicating desorption of ferrocene units, leaving only iodine atoms on the substrate (**Figure 3.5.c**).

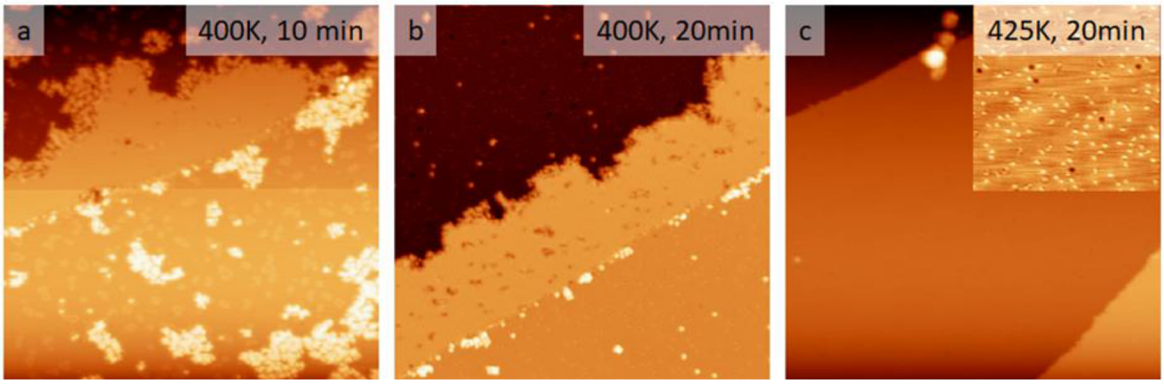

Figure 3.5: STM topographies of **polyferrocenylene** samples prepared at different annealing temperature/time on Ag(111). **(a)** Annealing temperature: ~400K, 10min: some **polyferrocenylene** nanowires, but also high amount of unordered ferrocene clusters on the surface. **(b)** Annealing temperature: ~400K, 20min: majority of the ferrocene forms ordered **polyferrocenylene** nanowires. **(c)** Annealing temperature ~425K, 20 min: ferrocene desorbs from the surface, only Iodine remains. Scanning Parameters: (a) (900 mV, 10 pA, 100 × 100 nm²); (b) (500 mV, 10 pA, 100 × 100 nm²); (c) (500 mV, 10 pA, 100 × 100 nm²), inset: 50 × 50 nm².

3.3. Structural Characterization of 2D Polyferrocenylene Islands

The PFcs formed on the surface have been resolved as bright rows in STM, packed in the form of two dimensional (2D) islands growing from the step edges of Ag(111) surface, **Figure 3.6**.

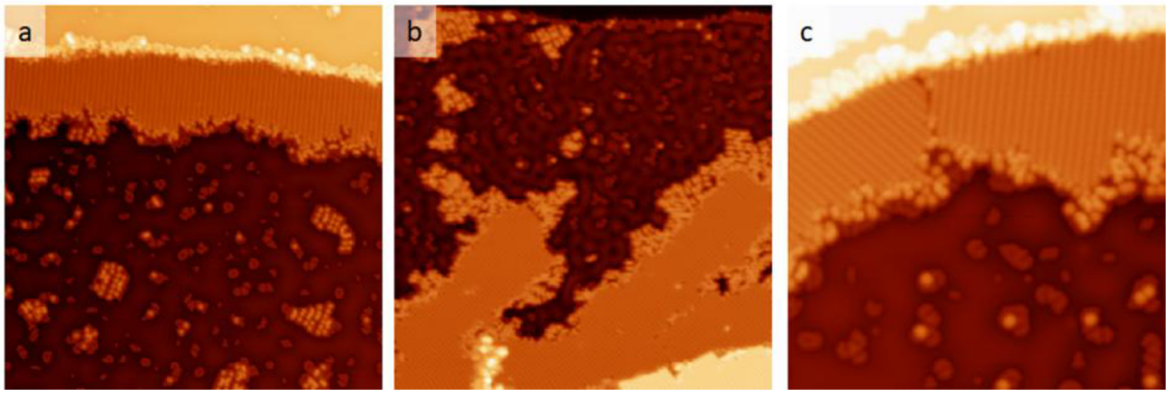

Figure 3.6: STM topography images of **polyferrocenylene** islands on Ag(111). Scanning Parameters: (a) (-300 mV, 20 pA, 70 × 70 nm²); (b) (30 mV, 10 pA, 80 × 80 nm²); (c) (-300 mV, 20 pA, 40 × 40 nm²).

The molecular ordering in the 2D islands is in two different forms, as observed in **Figure 3.7**.

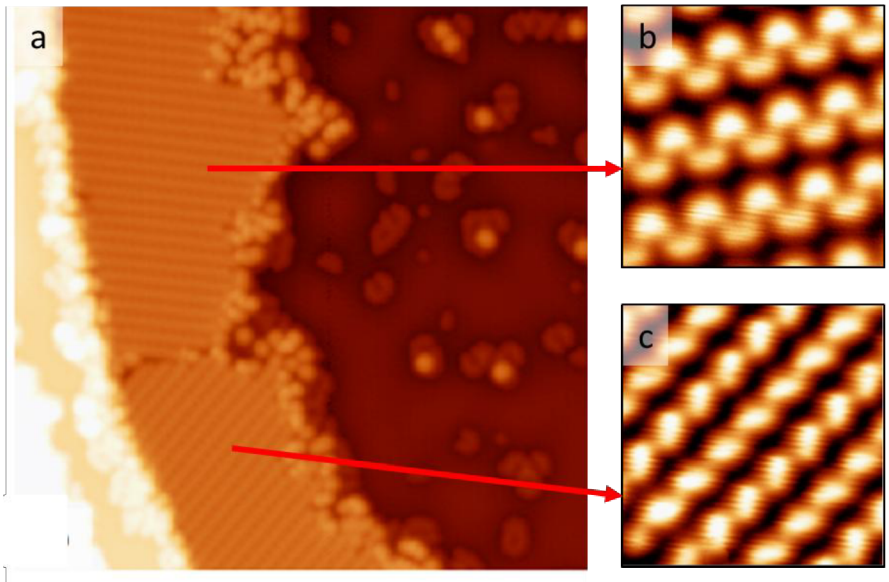

Figure 3.7: (a) STM overview of the two different polyferrocenylene islands. **(b, c)** Zoom in images of the polyferrocenylene nanowires in the two islands. Scanning Parameters: (a) (-100 mV, 20 pA, 40 × 40 nm²); (b) and (c) constant height current images: 1 mV, 3 × 3 nm². Adapted from [89]

This observation has been substantiated with high resolution AFM images with CO functionalized tips on the 2D polymer islands, **Figure 3.8** showing explicit contrasts for the two different molecular stacking. The molecular periodicities along the polymer (a_1 = ~0.4 nm, a_2 = ~ 0.55 nm) as well as the distance between two polymer rows (b_1 = ~1.0 nm, b_2 =~0.7 nm) are measured for **meander** and **zig-zag** 2D islands respectively, **Figure 3.8.a-b**. Based on the measurements, two models have been proposed for the two different PFc conformers **(Figure 3.2)** formed on the Ag(111) surface: **meander (Figure 3.8.c)** and **zig-zag (Figure 3.8.d)**.

The proposed models have been justified with the total energy Density Functional Theory (DFT) simulations. The AFM simulation images using the Probe particle model [84], in **Figure 3.8.c-d**, clearly match the experimental evidence of the two different 2D polymers islands thus favouring the proposed models.

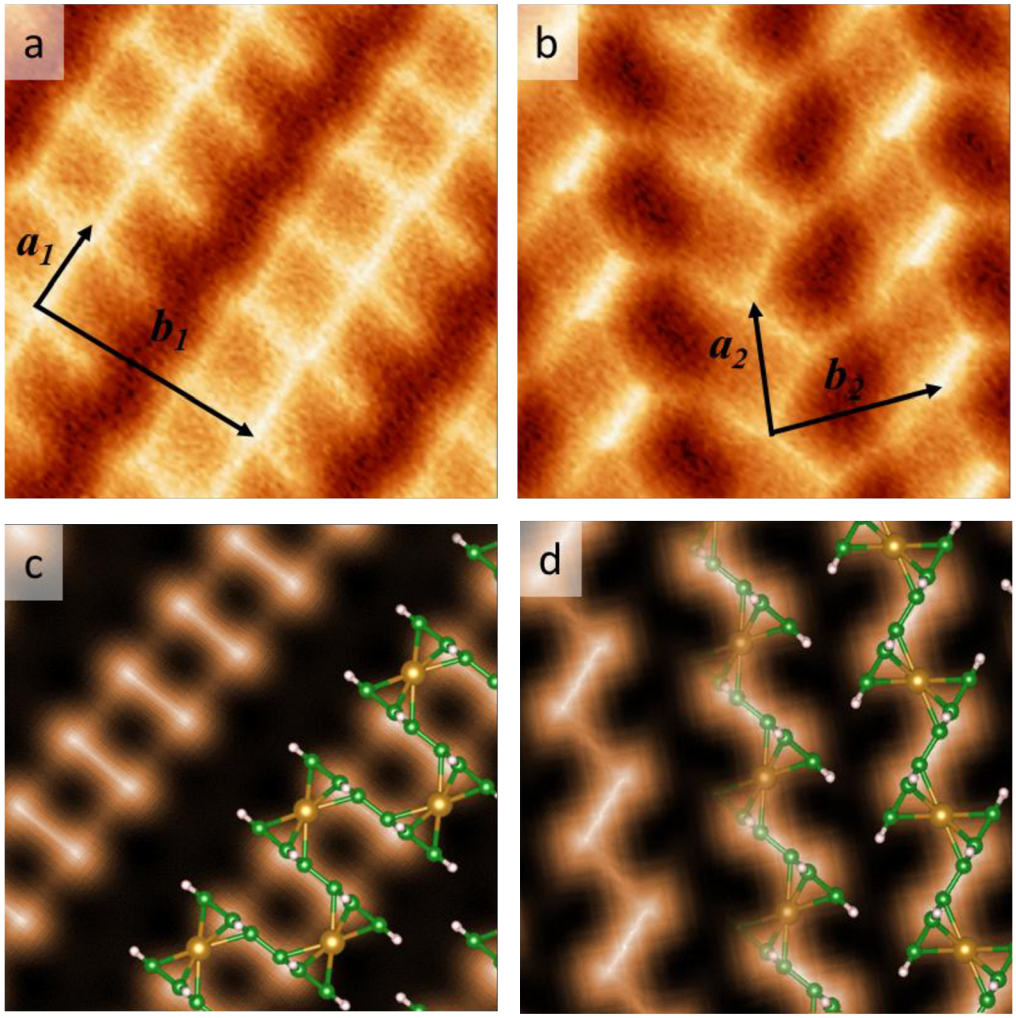

Figure 3.8: Structural arrangement of **polyferrocenylenes** in self-assembled islands. **(a, b)** High resolution constant height frequency shift images for **meander** and **zig-zag** PFc islands with different molecular arrangement respectively. Molecular periodicity highlighted by a and b vectors. **(c, d)** Simulated AFM images for the respective PFc islands. Proposed top view ball-stick models are superimposed over the simulated images. Scanning Parameters: (a,b) (10 mV, A_{osc} = 50 pm, 2 × 2 nm². Model: Fe, C, H, Ag atoms correspond to the yellow, green, white, and silver colors, respectively. Adapted from [89]

The PFc nanowires in the 2D islands are incommensurate with respect to the Ag(111) substrate, as depicted by constant height AFM images in **Figure 3.9**. It is clearly shown

that there is a mismatch between the high symmetry axes of the substrate and the polymer islands: ~11.5^0 for meander island (**Figure 3.9.a**) and ~5^0 for zig-zag island (**Figure 3.9.b**). This incommensurability evidently indicates that the interaction between the ferrocene units within the polymer is stronger than their coupling to the substrate.

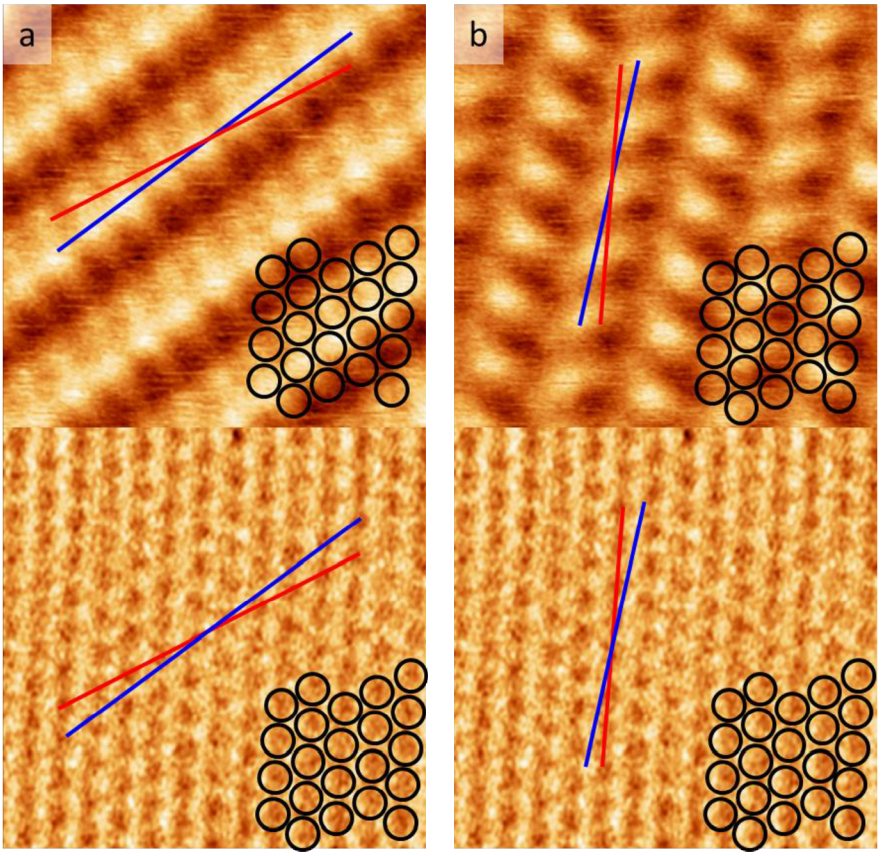

Figure 3.9: Incommensurability of the PFc islands. **(a,b)** Constant height AFM images over PFc islands with two different stacking. Bottom panel: constant height AFM images of atomically resolved Ag(111) lattice of the substrate. Red and blue lines highlight the high symmetry axis of the Ag(111) substrate and PFc rows, respectively. There is mismatch between high symmetry axes of the substrate and the Fc islands: 11.5° for stacking **(a)** and 5° for stacking **(b)**. Black circles added to highlight the atomic periodicity of the Ag(111) lattice. All images: 3 × 3 nm^2.

3.4. Lateral Manipulation of PFc Nanowires on Ag (111) Surface

It is necessary to establish the presence of covalently bonded PFc polymers in the 2D islands, and not just ferrocene units clustered together in an intricate fashion. This has been made possible by lateral manipulation experiments carried out with the help of STM tip, which also demonstrate weaker interactions of the PFc polymers with the substrate. The covalent coupling between the ferrocene centres is clearly visible as the chains are pulled from the edge of polymer row on the Ag(111) surface, causing the partial displacement of molecules inside the island. The edges of the islands are surrounded by the residual hydrogen and iodine adatoms which limits further connections between the polymer rows.

The PFc chains are arranged either in linear form or U-shaped inside the island, thus one polymer chain corresponding to one or two molecular rows respectively, **Figure 3.10**. The constant pulling over time resulted in the separation of PFc chain from the polymer island **(Figure 3.10.a-d)**. The high resolution constant height image on the island edge separated from the Ag(111) step edge, in **Figure 3.10.e-f**, clearly shows the structure of a U-shaped polymer chain. The ferrocene units tend to rotate during manipulation and thus some of them appear higher in STM. This rotation can be ascribed to the presence of two easy-rotation axes, one aligned across the polymer along the covalent bond between the two adjoining Cp rings and the other across each molecule, centred along the Cp rings of the individual molecule through the sandwiched iron atom.

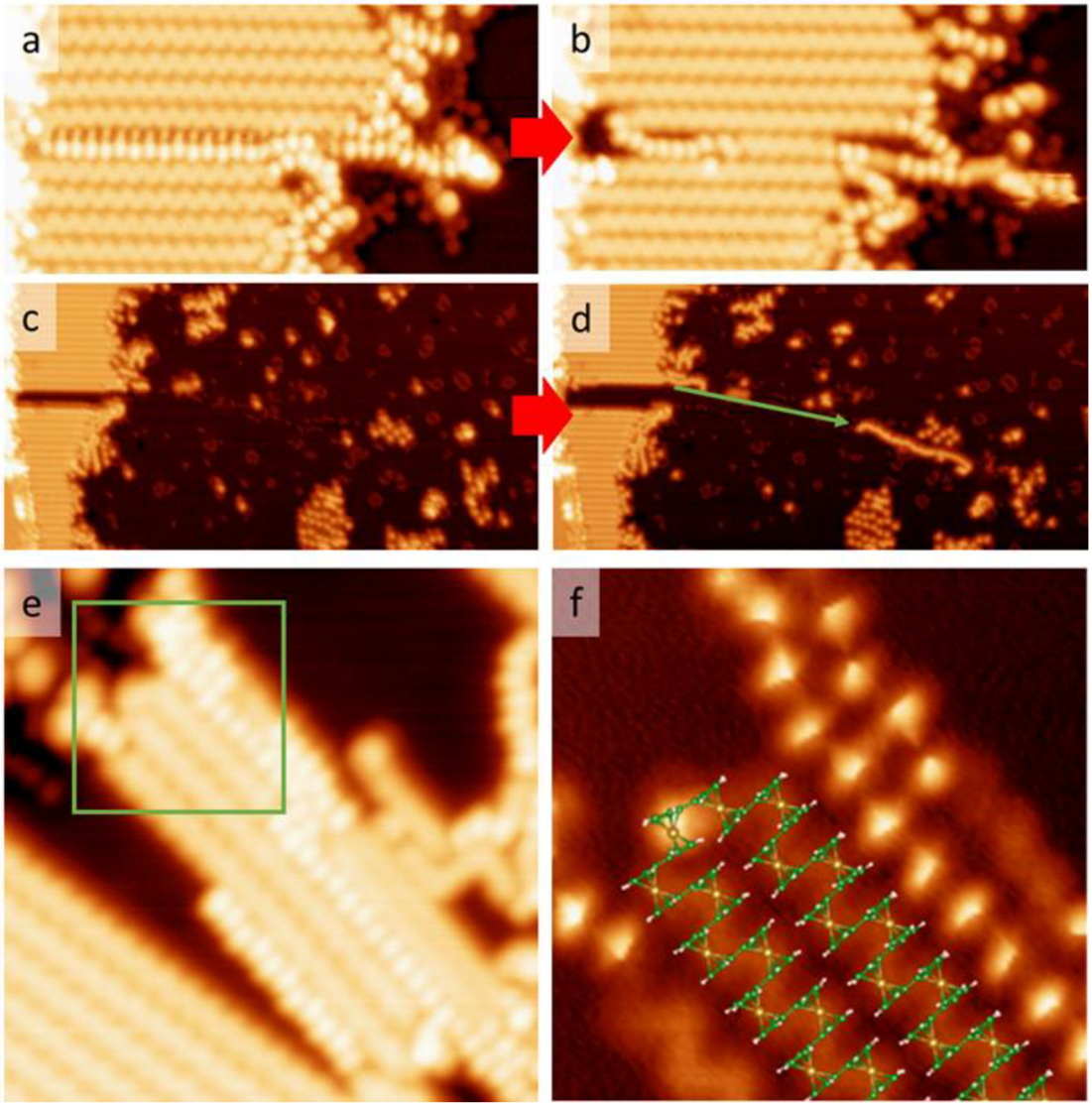

Figure 3.10: Polyferrocenylene nanowires self-assembled into 2D Islands: **(a-d)** STM sequence of successful interaction between scanning probe and molecular island. **(a-b)** Pulling a chain of PFc in the island. **(c-d)** Separation of the polymer chain from the island. **(e)** STM image of a separated island from the Ag(111) step edge. **(f)** High resolution constant height current image highlighting the interconnection between the molecular rows in the separated island. Tentative ball-stick model of the interconnection is superimposed. Scanning Parameters: (a, b) (500 mV, 20 pA, 10 × 5 nm²); (c, d) (500 mV, 20 pA, 70 × 35 nm²; (e) (300 mV, 20 pA, 14 × 14 nm²); (f) constant height zoom: 5 mV, 5 × 5 nm². Model: Fe, C, H atoms correspond to the yellow, green and white colors, respectively. Adapted from [89]

The length of PFc chain rationally depends on the coverage of bi-Fc molecules on the surface before the polymerization reaction. The polymer chains consisting of ~ 40 ferrocene units or more are much easier to pull and/or lift from the surface. A higher abundance of molecules on the surface result in longer polymer chains, around~50 nm (around 200 ferrocene units), **Figure 3.11.a**. The single PFc chain discussed above and further in **Sections 3.5** and **3.6** is 69 units long, **Figure 3.11.b**.

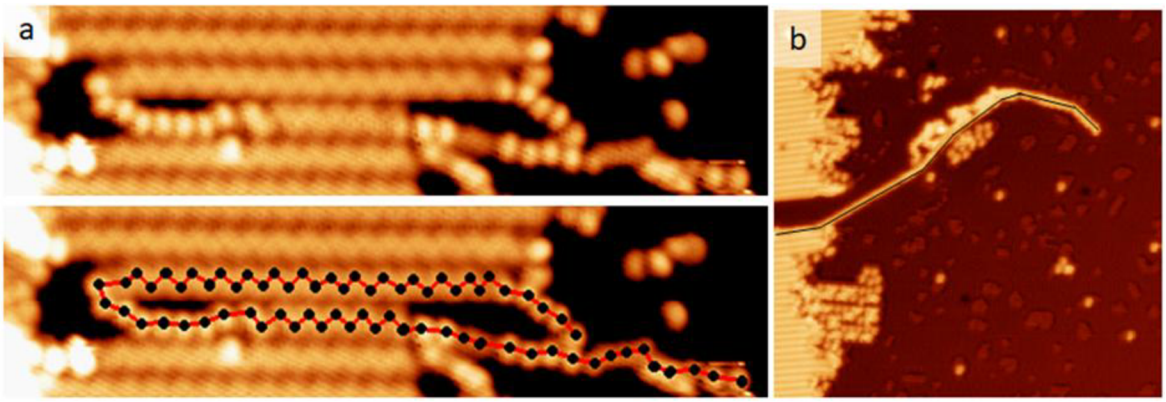

Figure 3.11: Polyferrocenylene nanowire length. **(a)** STM image of a manipulated **polyferrocenylene** nanowire. Bottom panel same as top but with superimposed black dots and red lines to highlight the order of the 69 ferrocene units in the nanowire. **(b)** STM image of a manipulated ~50 nm long **polyferrocenylene** nanowire. Black line highlights the nanowire. Scanning parameters: (a) (500 mV, 20 pA, 20 × 5 nm²); (b) (500 mV, 10 pA, 50 × 50 nm²).

3.5. Structure of Free Polyferrocenylene Chain

In this section, the molecular structure of a free PFc polymer (**Figure 3.12**) pulled out of the zig-zag confirmation 2D island has been discussed. The high resolution AFM image of PFc chain with a CO tip, in **Figure 3.12.a**, show two stable configurations of

ferrocene units which differ in their apparent heights. The two configurations: **perpendicular and inclined**, are a result of the rotation of the ferrocene units as well as the flexibility of the polymer. The perpendicular configuration is achieved when the Cp rings of the ferrocene unit align perpendicular to the substrate while the inclined configuration is when the Cp rings are protruding at an inclination of ~ 45^0 from the Ag(111) surface. The configurations have been precisely depicted with the help of simulated AFM images (**Figure 3.12.b**) and ball and stick models. The intermolecular distance (a_3) along the free polymer is ~0.55 nm for both the configurations (**Figure 3.12.a**), same as the molecular periodicity of the zig zag polymer 2D island (**Figure 3.8.b**).

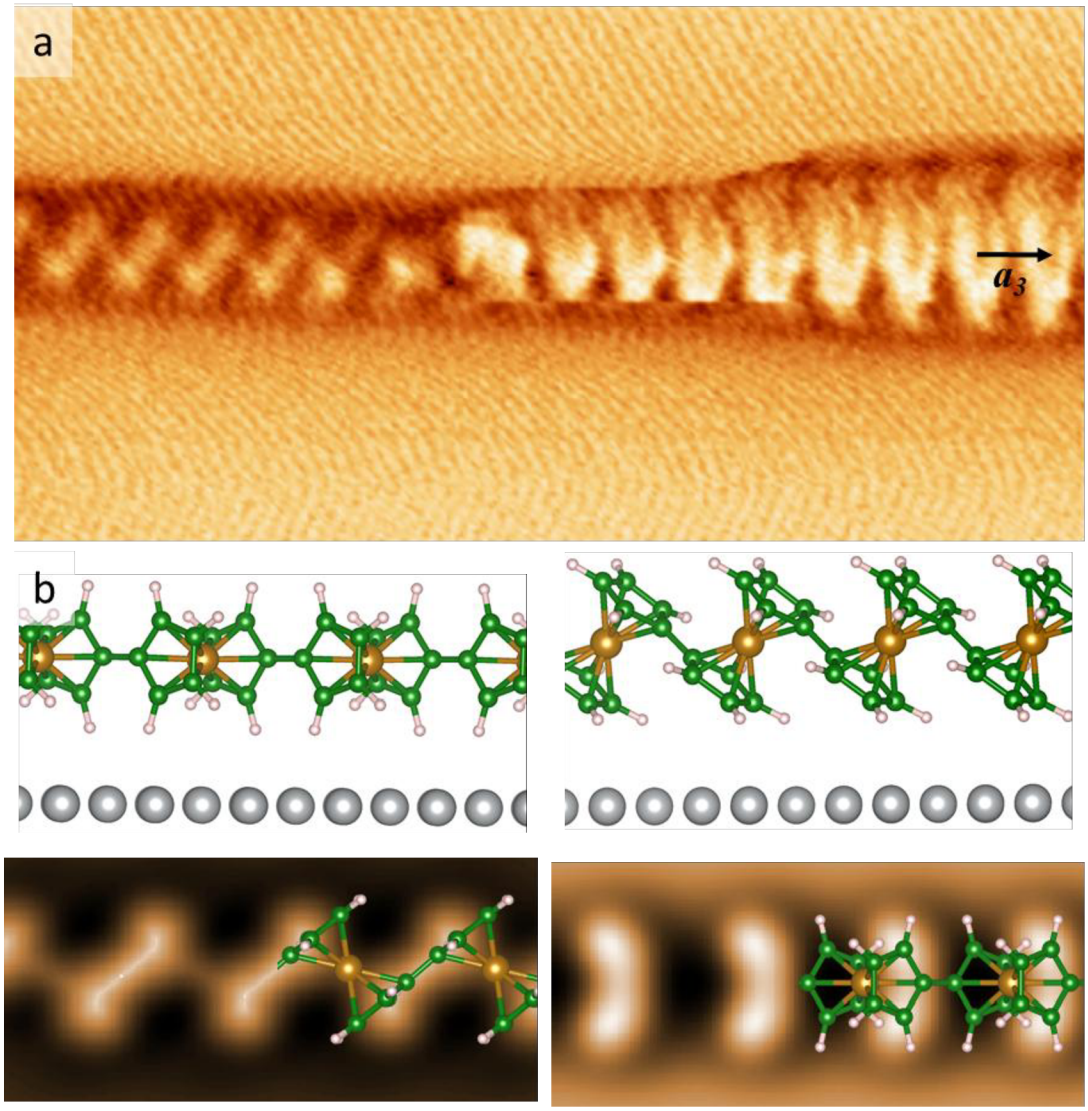

Figure 3.12: Structural arrangement of individual **polyferrocenylene** chain: **(a)** High resolution constant height frequency shift image of the isolated polymer chain. Molecular periodicity highlighted by a_3 vector. **(b)** Simulated AFM image of the isolated polymer chain showing perpendicular and inclined configurations. Proposed top view ball-stick models are superimposed over the simulated images. Scanning parameters: (a) (10 mV, A_{osc} = 50 pm, 8 × 4 nm²). Model: Fe, C, H, Ag atoms correspond to the yellow, green, white, and silver colors, respectively.

The series of successive constant height images, in **Figure 3.13**, on a PFc chain shows the process of reversible switching between the two configurations. This is possible by

causing perturbations on the chain with the help of scanning probe interactions. The transition area between the perpendicular and inclined configurations of the PFc chain has been shown in **Figure 3.13.b**. The height difference between the two configurations has been estimated by force spectroscopy measurements taken on the ferrocene units of the PFc chain, as shown in **Figure 3.13.c**. The ferrocene units in the inclined configuration are protruding 90 pm more from the surface than the ferrocene centres in the perpendicular configuration.

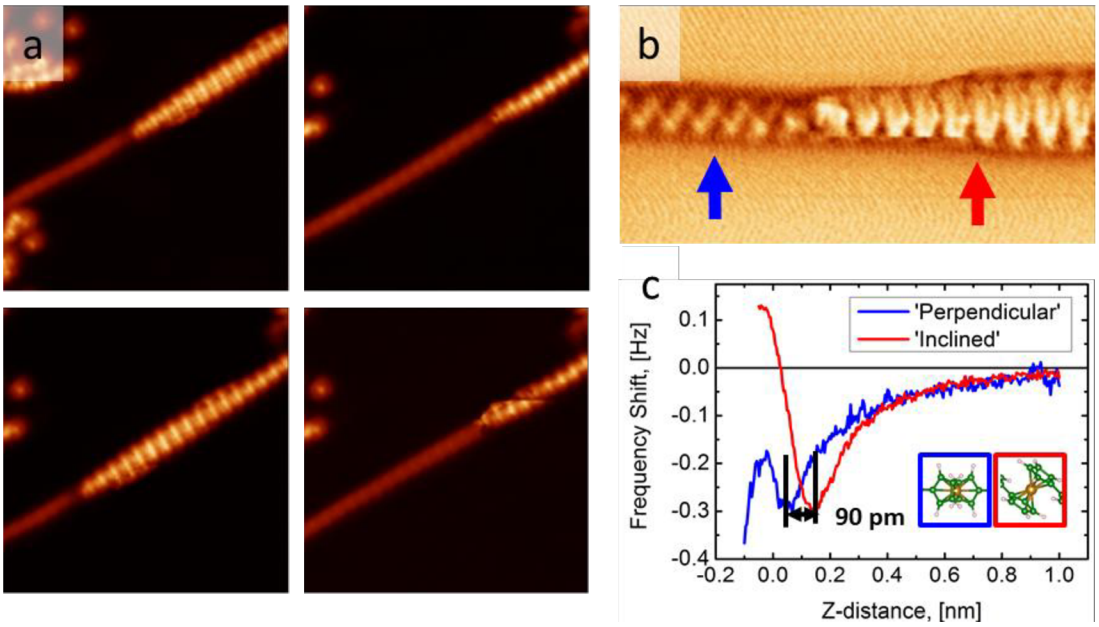

Figure 3.13: (a) Series of consecutive constant height STM images on a PFc chain. After each image the chain is perturbed with the scanning probe switching parts of the chain between standing and side configurations. **(b)** Constant height AFM image with CO functionalized tip on the transition area between side and standing configurations of the PFc chain. **(c)** *Δf(z)* spectroscopy taken on the Fc units corresponding to side (blue curve) and standing (red curve) configurations. Fc units in standing configuration are protruding 90 pm more from the surface than in side configuration. Fc molecules models for side and standing configurations are shown in the inset. Scanning Parameters: (a) (30 mV, 10 × 10 nm^2); (b) (10 mV, A_{osc} = 50 pm, 8 × 4 nm^2).

3.6. Electronic Properties of Polyferrocenylene

The geometrical characterization of the two different 2D polymer islands stimulates to study their electronic properties with the help of scanning tunneling spectroscope (STS). The dI/dV spectra (**Figure 3.14.d**) showed a prominent band gap of ~580 mV for the meander island (**Figure 3.14.a**) while a higher band gap of ~780 mV was observed for the zig-zag polymer island (**Figure 3.14.b**). The self-assembly of ferrocene units into 2D islands after deiodination, and subsequent formation of 1D PFc chains has significantly reduced the band gap of the system as compared to the single precursor molecules.

The dI/dV spectra of a single PFc chain (**Figure 3.14.c**) completely separated from the island is different from the 2D island depending on the configuration of the ferrocene units, shown in **Figure 3.14.d**. The perpendicular configuration shows similar dI/dV spectra as the 2D zig-zag island and has a same band gap of ~ 780mV. Unlike the perpendicular configuration, the inclined configuration of ferrocene molecule in the 1D PFc polymer shows a metallic behaviour dI/dV spectra with no band gap. The higher transverse conductivity of inclined configuration could be the result of charge transfer towards the surface. This is possible due to the standing orientation of ferrocene units causing the overlap of p_z orbitals of the Cp rings with the Ag(111) surface.

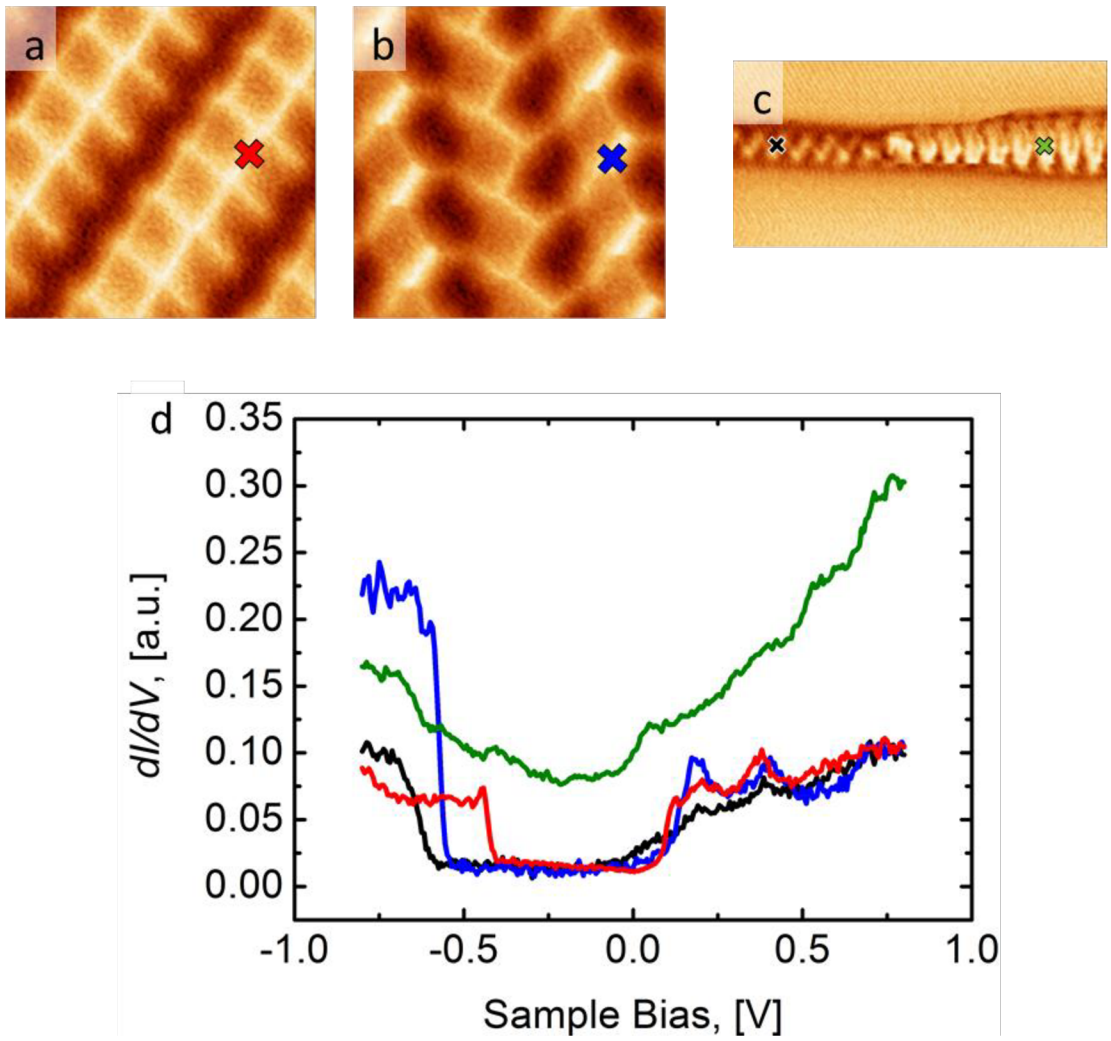

Figure 3.14: dI/dV measured on the two islands **(a,b)** and the free chain of **polyferrocenylene (c)**. **(d)** Red, blue, green, and black graphs correspond to measurements on **meander** island, **zig-zag** island, **inclined** configuration and **perpendicular** configuration of the free chain, respectively. The positions of spectroscopy are marked in (a-c) by crosses of the same color. Scanning Parameters: (a, b) (10 mV, A_{osc} = 50 pm, 2 × 2 nm²); (c) (10 mV, A_{osc} = 50 pm, 8 × 4 nm²).

The Kelvin Probe Force Microscopy (KPFM) measurements performed on the Fc_2-I_2 island as well as free 1D PFc chain, as depicted in **Figure 3.15**, show that the formation

of PFc on Ag(111) surface tend to decrease the work function, corresponding to an effect where PFc carries a partial positive charge thus acts as an electron donor.

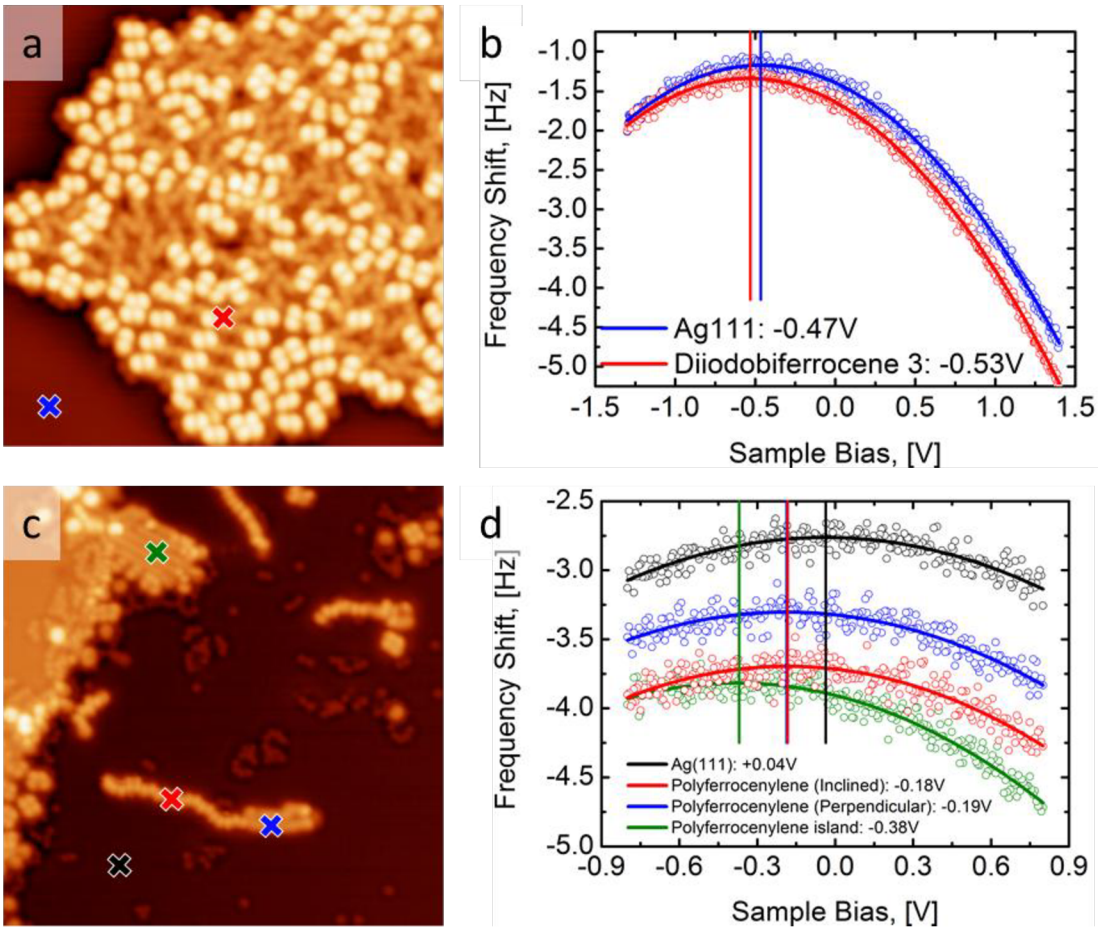

Figure 3.15. KPFM measurements. **(a)** STM image of **Fc_2-I_2** island in disordered phase. **(b)** $\Delta f(V)$ spectroscopy taken on **Fc_2-I_2** island (red curve) and Ag(111) substrate (blue curve). **(c)** STM image post Ullmann coupling reaction. **Polyferrocenylene** nanowire is separated out from the island. **(d)** $\Delta f(V)$ spectroscopies taken on Fc island (green), different parts of PFc nanowire (standing configuration: red and side configuration: blue, respectively) and Ag(111) substrate (black). Scanning Parameters: (a) (500 mV, 20 pA, A_{osc} = 50 pm, 30 × 30 nm²); (c) (50 mV, 10 pA, A_{osc} = 50 pm, 25 × 25 nm²). Crosses in the STM images mark the positions where spectroscopies of same color were taken. Vertical lines in spectroscopy

curves mark the value of contact potential difference (CPD). Corresponding CPD values shown in the insets.

3.7. Charge Transport in Polyferrocenylene Nanowire

The electronic structure of the 1D PFc polymer chain was further studied by performing a controlled lifting process with the help of SPM probe [144]–[148]. These measurements also helped to analyse the influence of the metallic substrate on the 1D polymer chain, as it is lifted from the surface. The simultaneous STM/AFM measurement tracked both tunneling current I and frequency shift Δf during the lifting experiment, hence record the mechanical and transport properties of the single polymer chain in the longitudinal direction.

The 1D polymer is pulled away from the surface by contacting the terminal ferrocene unit of the free polymer chain with the STM tip, as illustrated in **Figure 3.16.a**. The frequency spectra (Δf) recorded with respect to the tip lifting distance (z) portrayed an oscillating behaviour with varying periodicity on lifting the 1D polymer from the surface, as shown in **Figure 3.16.b**. Usually, for planar π-conjugated systems the frequency spectra Δf(z) is a periodic signal with a single well-defined oscillation amplitude. This periodic signal is a measure of each unit of the 1D system lifting from the substrate. But, the 1D PFc chain is unlike other systems showing an irregular variation in the frequency spectra during the lifting process. This behaviour has been studied theoretically for a better understanding by performing a steered molecular dynamics simulation of the lifting process of the 1D PFc polymer chain from the surface [89].

The I/V spectra recorded during the lifting experiments is a great tool to study the conductivity of the 1D polymer as a function of tip-sample distance(z) from the surface. On the start of the pulling process, there is no apparent band gap and the current increases abruptly with the applied bias, as shown in **Figure 3.16.c** (red curve). Hence the system behaves metallic, with a slow opening of the band gap as the tip-sample distance increases on lifting the polymer. The experimental band gap has been defined as a bias range when the current I is above the threshold value of 0.5 pA. Initially a flat region is seen at low biases in the I/V spectra on increasing the tip-sample distance. The band gap opening mostly happens when around 3-5 ferrocene units are hanging from the STM tip which is equal to a tip lifting distance of ~1.5-2.5 nm from the surface. An asymmetric opening of the band gap is shown in **Figure 3.16.d**, as a function of lifting distance (z) and bias polarity; bang gap opens faster for positive biases as compared to negative bias.

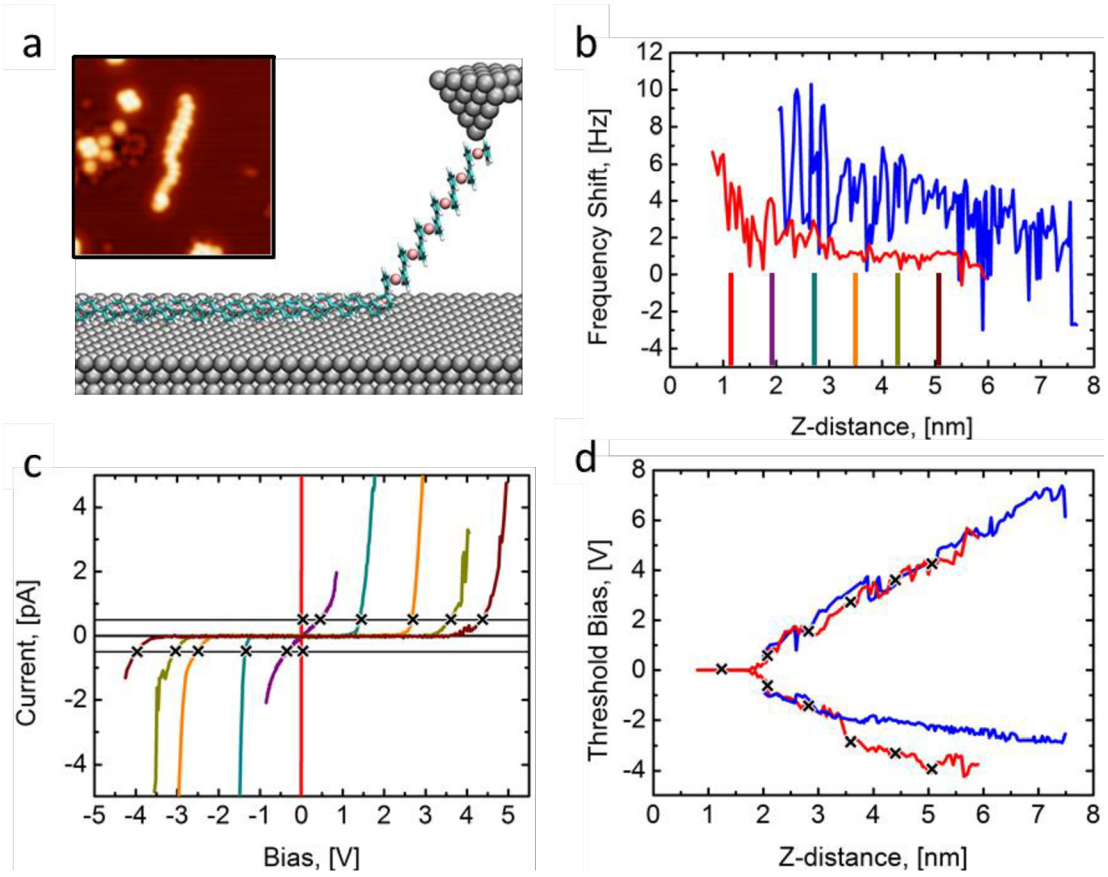

Figure 3.16: Lifting experiments with polyferrocenylene : **(a)** Simulated model of the partially lifted polyferrocenylene **2**. Inset: STM image of an isolated polyferrocenylene **2** before the lift. **(b)** Two $\Delta f(z)$ data sets taken during the polyferrocenylene **2** lifting experiment highlighted in red and blue colors. **(c)** I/V spectroscopy curves taken for the red data set for different z-distances: vertical lines of the same color in (b). Threshold bias defined from the 0.5 pA cut-off current marked as black crosses. **(d)** Threshold bias for the red and blue data set as a function of the lifting distance. Black crosses correspond to the bias threshold estimated from the curves shown in (c). Scanning Parameters: (a) inset: 500 mV, 20 pA, 15 × 15 nm², A_{osc} = 50 pm. (b, d) The z=0 height corresponds to the tip-sample height at STM feedback parameters of V= 1 mV, I = 3nA on clean Ag(111) surface for a metallic terminated tip.

The experimental charge transport behaviour of the 1D PFc polymer on lifting from the Ag(111) surface has been supported theoretically by developing a tight-binding model

based on previous models used to explain the transport characteristics of such systems during the past decades, as presented in [89].

3.8. Conclusion and Perspectives

This chapter has described the synthesis of long flexible polyferrocenylene nanowires measuring around 50 nm in length on Ag(111) surface. These nanowires initially self-assemble into two dimensional islands on Ullmann coupling of the precursor molecules. They can be laterally manipulated from the islands into free 1D chains on surface. The combined STM/AFM technique has been used to characterize both the 2D islands and the free 1D chain on the surface. The transport properties of single chain PFc polymer has been studied both in longitudinal and transversal directions. An apparent band gap opening has been observed for the voltage range where the nanowire is not conductive, during the lifting experiments. A non-resonant coherent charge transport model has been designed theoretically to explain the charge transport. With the help of spectroscopy experiments, the electronic properties of the PFc structures on the surface has been studied. A transition from semiconductor to metallic nature has been observed for a free nanowire on the surface depending on the orientation of the ferrocene units on the surface. A metal to insulator transition could be achieved on lifting the nanowire from the surface depending on the number of ferrocene units lifted with the help of STM tip.

The on-surface synthesis approach has paved the way to synthesise long, pure and stable individual PFc polymers which is otherwise a critical task using the traditional solution polymerization technique. It is much easier to study the structural and electronic properties on surface than in solution, even though surfaces might produce their own

effects. It would be interesting to carry out such polymerization techniques on semiconductor or insulator coated metal surfaces to understand the deviation in its structural and electronic properties. The study of magnetic characteristics of such polymers will be another interesting challenge in on-surface studies.

Conclusion

In this thesis, two different 1D polymers have been synthesised on metal surfaces and their structural geometry and electronic properties have been investigated with the help of combined STM/nc-AFM technique under UHV. The common characteristic of both the 1D systems described herein, lies in the presence of metal atoms in the polymer chain but in two different fashions: the first quinone based polymer has metal atoms coordinated with the quinone ligand forming π-d conjugated coordination polymers while the second 1D polymer is in itself made up of metal containing organometallic monomer units i.e. ferrocene.

The 1D coordination polymer has been formed as a result of dehydrogenative metalation of 2HQDI ligand molecule with transition metals such as Cr, Fe, Co, Ni, Cu. The on-surface synthesis approach led to the formation of long flexible polymers upto 100 nm. The MQDI (M=Cr, Fe, Co, Ni) and Cu_2QDI nanowires differ in their coordination modes on surface: the former showing a four-fold square planar coordination while the latter has a two-fold linear coordination. Regardless of the nature of the surface, the MQDI (M=Cr,Fe,Co,Ni) nanowires are structurally similar as characterized by high resolution nc-AFM imaging with CO functionalized tips and the AFM simulations clearly supports the experimental images. This system has paved its path towards a new class of anti-aromatic macrocycles constituting the backbone of the 1D Cu_2QDI nanowire characterized with the help of DFT calculations and a number of aromaticity predictions.

The work is in progress to study the charge transport through the 1D polymers by lifting the nanowires from the surface with the help of STM tip. The magnetic character of these nanowires on surface and on lifting them from the surface is under investigation.

In this work, the generation of long, flexible 1D PFc chains on a metal surface with lengths up to 50 nm is introduced, representing the longest homo-coupled polyferrocenylene known to date. The organometallic PFc are special homopolymers with direct covalent bonding between their ferrocene units. However, they are challenging for wet chemistry techniques due to precursor insolubility and the presence of impurities, which prevent the formation and investigation of high-molecular weight PFcs.

For this purpose, the Ullmann coupling reaction on atomically clean Ag(111) surface to polymerize 1,1'-diiodobiferrocene precursors is employed under ultra-high vacuum conditions. A controlled manipulation process is carried out to successfully isolate individual 1D PFc nanowires from the 2D polymer islands. The scanning tunneling spectroscopies of the polymers in the islands versus the free chain, helps to identify a transition from semiconducting electronic structure of the polymer 2D islands to a metal-like electronic character of the 1D chains depending on the orientation of the molecules on the surface. These observations are rationalized by calculations based on density functional theory. Finally, lifting experiments of chains are performed via the scanning probe to study the charge transport through the nanowires, showing a transition to insulating regime with the number of ferrocene units lifted from the surface. The charge transport studies have been supported by a theoretically devised transport model.

The advanced possibilities of synthesising such polymers on surface help to overcome the challenges faced in solution polymerization. The limits of solubility and purity do not allow producing polymers of large molecular weight thus only short oligomers have been synthesised ever. It is also not possible to separate individual polymers in solution and

study their physical and chemical properties, thus making the on surface characterization techniques an asset for studying such systems. Even though there is a huge progress in the field of UHV on surface chemistry, there are a lot of hurdles in bringing the pure academic research into application. It is possible to get individual polymers on surface but cannot be transferred outside the UHV system for further characterizations such as mass analysis.

The ultimate goal here is to demonstrate the new possibilities of synthesizing long flexible metal coordination polymers and organometallic polymers and characterize their material properties, which has not been possible in solution.

Bibliography

[1] L. A. Kolahalam, I. V. Kasi Viswanath, B. S. Diwakar, B. Govindh, V. Reddy, and Y. L. N. Murthy, "Review on nanomaterials: Synthesis and applications," *Mater. Today Proc.*, 18, 2182–2190, 2019.

[2] S. Mobasser and A. Akbar Firoozi, "Review of Nanotechnology Applications in Science and Engineering," *Journal of Civil Engineering and Urbanism*, 4, 84-93, 2016.

[3] K. K. Johannes V. Barth, Giovanni Costantini, "Engineering atomic and molecular nanostructures at surfaces," *Nature*, 437, 671-679, 2005.

[4] G. Schmid, V. Balzani, A. Credi, M. Venturi, and G. Hodes, *The Chemistry of Nanomaterials*. Wiley, 2004.

[5] L. A. Kolahalam, I. V. Kasi Viswanath, B. S. Diwakar, B. Govindh, V. Reddy, and Y. L. N. Murthy, "Review on nanomaterials: Synthesis and applications," *Materials Today: Proceedings*, 18, 2182–2190, 2019.

[6] T. P. Yadav, R. M. Yadav, and D. P. Singh, "Mechanical Milling: a top down approach for the synthesis of nanomaterials and nanocomposites," *Nanoscience and Nanotechnology*, 2, 22–48, 2012.

[7] H. D. Yu, M. D. Regulacio, E. Ye, and M. Y. Han, "Chemical routes to top-down nanofabrication," *Chem. Soc. Rev.*, 42, 6006–6018, 2013.

[8] B. K. Teo and X. H. Sun, "From top-down to bottom-up to hybrid nanotechnologies: Road to nanodevices," *J. Clust. Sci.*, 17, 529–540, 2006.

[9] M. Kwiat, S. Cohen, A. Pevzner, and F. Patolsky, "Large-scale ordered 1D-nanomaterials arrays: Assembly or not?," *Nano Today*, 8, 677–694, 2013.

[10] D. Vollath, "Nanomaterials an introduction to synthesis, properties and application," *Environ. Eng. Manag. J.*, 7, 865–870, 2008.

[11] A. Biswas, I. S. Bayer, A. S. Biris, T. Wang, E. Dervishi, and F. Faupel, "Advances

in top-down and bottom-up surface nanofabrication: Techniques, applications & future prospects," *Advances in Colloid and Interface Science*, 170, 2–27, 2012.

[12] L. Liu , H. Klaasen, A. Timmer, H.-Y. Gao, D. Barton, H. Mo¨nig, J. Neugebauer and H. Fuchs,*,†,‡ and Armido Studer "α-Diazo Ketones in On-Surface Chemistry," *J. Am. Chem. Soc.*, 140, 6000–6005, 2018.

[13] P. A. Held, H. Fuchs, and A. Studer, "Covalent-bond formation via on-surface chemistry," *Chem. - A Eur. J.*, 23, 5874–5892, 2017.

[14] S. Clair and D. G. De Oteyza, "Controlling a chemical coupling reaction on a surface: Tools and strategies for on-surface synthesis," *Chem. Rev.*, 119, 4717–4776, 2019.

[15] G. Franc and A. Gourdon, "Covalent networks through on-surface chemistry in ultra-high vacuum: State-of-the-art and recent developments," *Phys. Chem. Chem. Phys.*, 13, 14283–14292, 2011.

[16] G. Binnig, C. F. Quate' ', E. L. Gi, and C. Gerber, "Atomic Force Microscope." *Phy. Rev. Lett.*, 56, 930-934, 1986

[17] F. J. Giessibl, "Advances in atomic force microscopy." *Rev. Mod. Phys.* 75, 949, 2003.

[18] G. Binning, H. Rohrer, C. Gerber, and E. Weibel, "Surface studies by scanning tunneling microscopy," *Phys. Rev. Lett.*, 49, 57–61, 1982.

[19] P. K. Hansma and J. Tersoff, "Scanning tunneling microscopy," *J. Appl. Phys.*, 61, 1987.

[20] Q. Fan, J. Dai, T. Wang, J. Kuttner, G. Hilt, J.M. Gottfried, J. Zhu , "Confined synthesis of organometallic chains and macrocycles by Cu-O surface templating," *ACS Nano*, 10, 3747–3754, 2016.

[21] Q. Fan, J. M. Gottfried, and J. Zhu, "Surface-catalyzed C-C covalent coupling strategies toward the synthesis of low-dimensional carbon-based nanostructures," *Acc. Chem. Res.*, 48, 2484–2494, 2015.

[22] L. Dong, P. N. Liu, and N. Lin, "Surface-activated coupling reactions confined on a

Surface," *Acc. Chem. Res.*, 48, 2765–2774, 2015.

[23] J. Liu, Q. Chen, L. Xiao, J. Shang, X. Zhou, Y. Zhang, Y. Wang, X. Shao, J. Li, W. Chen, G.Q. Xu, H. Tang, D. Zhao, K. Wu, "Lattice-directed formation of covalent and organometallic Molecular wires by terminal alkynes on Ag surfaces," *ACS Nano*, 9, 6305–6314, 2015.

[24] Z. Cai, L. She, L. Wu, and D. Zhong, "On-surface synthesis of linear polyphenyl wires guided by surface steric effect," *J. Phys. Chem. C*, 120, 6619–6624, 2016.

[25] F. Kang and W. Xu, "On-surface synthesis of one-dimensional carbon-based nanostructures via C-X and C-H activation reactions," *ChemPhysChem*, 201900266, 2019.

[26] S. Haq, F. Hanke, M.S. Dyer, M. Persson, P. Iavicoli, D.B. Amabilino, R. Raval,, "Clean coupling of unfunctionalized porphyrins at surfaces to give highly oriented organometallic oligomers," *J. Am. Chem. Soc.*, 133, 12031–12039, 2011.

[27] M. Di Giovannantonio, M. Tomellini, J. Lipton-Duffin, G. Galeotti, M. Ebrahimi, A. Cossaro, A. Verdini, N. Kharche, V. Meunier, G. Vasseur, Y. Fagot-Revurat, D.F. Perepichka, F. Rosei, G. Contini, "Mechanistic picture and kinetic analysis of surface-confined Ullmann polymerization," *J. Am. Chem. Soc.*, 138, 51, 16696–16702, 2016.

[28] C. Nacci, F. Ample, D. Bleger, S. Hecht, C. Joachim, and L. Grill, "Conductance of a single flexible molecular wire composed of alternating donor and acceptor units," *Nat. Commun.*, 6, 1–8, 2015.

[29] H. Denawi, M. Koudia, R. Hayn, O. Siri, and M. Abel, "On-surface synthesis of spin crossover polymeric chains," *J. Phys. Chem. C*, 122, 15033–15040, 2018.

[30] Q. Sun, L. Cai, H. Ma, C. Yuan, and W. Xu, "Dehalogenative homocoupling of terminal alkynyl bromides on Au(111): Incorporation of acetylenic scaffolding into surface nanostructures," *ACS Nano*, 10, 7023–7030, 2016.

[31] P. Jelinek, "High resolution SPM imaging of organic molecules with functionalized tips," *J. Phys. Condens. Matter*, 29, 343002-18 2017.

[32] V. L. Mironov, “Fundamentals of Scanning Probe Microscopy,” *Russ. Acad. Sci. Inst. Phys. Microstruct.*, 1–95, 2004.

[33] D. W. Pohl, “Some design criteria in scanning tunneling microscopy.,” *IBM J. Res. Dev.*, 30, 417–427, 1986.

[34] A. L. Gassó, “Scanning Tunneling Microscopy : The new eyes and hands of the scientists,” 2018.

[35] J. E. Griffith and G. P. Kochanski, “Scanning tunneling microscopy,” *Annu. Rev. Mater. Sci.*, 20, 219–244, 1990.

[36] R. Fainchtein, “Scanning tunneling microscopy of organic conductors and superconductors,” *JHATD*, 13, 332–341, 1992.

[37] G. Binnig and H. Rohrer, “Scanning tunneling microscopy from birth to adolescence’,” *Reviews of Modern Physics*, 1987

[38] R. García and R. Pérez, “Dynamic atomic force microscopy methods,” *Surface Science Reports*, 47, 197–301, 2002.

[39] F. J. Giessibl, “The qPlus sensor, a powerful core for the atomic force microscope,” *Rev. Sci. Instrum.*, 90, 011101-59, 2019.

[40] www.specs-group.com/nc/specs/products/detail/kolibrisensor/, “KolibriSensor _ SPECS.” .

[41] J. Moussa and H. Amouri, “Supramolecular assemblies based on organometallic quinonoid linkers: a new class of coordination networks,” *Angew. Chemie - Int. Ed.*, 47, 1372–1380, 2008.

[42] J. López, F. De La Cruz, Y. Alcaraz, F. Delgado, and M. A. Vázquez, “Quinoid systems in chemistry and pharmacology,” *Med. Chem. Res.*, 24, 3599–3620, 2015.

[43] S. Pascal and O. Siri, “Benzoquinonediimine ligands: Synthesis, coordination chemistry and properties,” *Coord. Chem. Rev.*, 350, 178–195, 2017.

[44] O. Siri, P. Braunstein, M. M. Rohmer, M. Bénard, and R. Welter, “Novel ‘potentially antiaromatic’, acidichromic quinonediimines with tunable

delocalization of their 6π-electron subunits," *J. Am. Chem. Soc.*, 125, 13793–13803, 2003.

[45] B. Sarkar, D. Schweinfurth, N. Deibel, and F. Weisser, "Functional metal complexes based on bridging "imino"-quinonoid ligands", *Coord. Chem. Rev.* 293, 250-262, 2015.

[46] S. Hünig, "Aromatic/quinoid systems: Principles and applications," *Pure Appl. Chem.*, 62, 395–406, 1990.

[47] R. A. Metcalfe, L. C. G. Vasconcellos, H. Mirza, W. Franco, and A. B. P. Lever, "Synthesis and characterization of dinuclear complexes of 3,3',4,4'-tetraminobiphenyl with tetramminoruthenium and bis(bipyridine)- ruthenium residues and their two- and four-electron oxidized products including a ZINDO study of orbital mixing as a function of ligand oxidation state ," *J. Chem. Soc., Dalton Trans.*, 2653–2667, 1999.

[48] H. Audi, Z. Chen, A. Charaf-Eddin, A. D'Aléo, G. Canard, D. Jacquemin, O. Siri., "Extendable nickel complex tapes that reach NIR absorptions," *Chem. Commun.*, 50, 15140–15143, 2014.

[49] H. Rumpel and H. H. Limbach, "NMR study of kinetic HH/HD/DD isotope, solvent, and solid-state effects on the double proton transfer in Azophenine," *J. Am. Chem. Soc.*, 111, 5429–5441, 1989.

[50] R. Nietzki and E. Hagenbach, "Ueber tetramidobenzol und seine derivate," *Berichte der Dtsch. Chem. Gesellschaft*, 20, 328–338, 1887.

[51] H. Masui, A. B. P. Lever, and E. S. Dodsworth, "Substituent effects and bonding characteristics in (o-Benzoquinone diimine)bis(bipyridine)ruthenium(II) complexes," *Inorg. Chem.*, 32, 258–267, 1993.

[52] J. Rall, A. F. Stange, K. Hübler, and W. Kaim, "A coordination-induced 1,4→1,2-quinonediimine isomerization," *Angew. Chemie Int. Ed.*, 37, 2681–2682, 1998.

[53] D. Schweinfurth, M. M. Khusniyarov, D. Bubrin, S. Hohloch, C. Y. Su, and B. Sarkar, "Tuning spin-spin coupling in quinonoid-bridged dicopper(II) complexes through rational bridge variation," *Inorg. Chem.*, 52, 10332–10339, 2013.

[54] N. Deibel, M. G. Sommer, S. Hohloch, J. Schwann, D. Schweinfurth, F. Ehret, B. Sarkar, "Dinuclear quinonoid-bridged d^8 metal complexes with redox-active azobenzene stoppers: Electrochemical properties and electrochromic behavior," *Organometallics*, 33, 4756–4765, 2014.

[55] I. R. Jeon, J. G. Park, D. J. Xiao, and T. D. Harris, "An azophenine radical-bridged Fe_2 single-molecule magnet with record magnetic exchange coupling," *J. Am. Chem. Soc.*, 135, 16845–16848, 2013.

[56] J. A. Degayner, I. R. Jeon, and T. D. Harris, "A series of tetraazalene radical-bridged M_2 (M = CrIII, MnII, FeII, CoII) complexes with strong magnetic exchange coupling," *Chem. Sci.*, 6, 6639–6648, 2015.

[57] K. Ohno, T. Fujihara, and A. Nagasawa, "Formation of boron, nickel(II) and iridium(III) complexes with an azophenine derivative: Isomerization, delocalization and extension of the π-conjugated system on coordination," *Polyhedron*, 81, 715–722, 2014.

[58] K. Ohno, A. Nagasawa, and T. Fujihara, "Dinuclear nickel(II) complexes with 2,5-diamino-1,4-benzoquinonediimine ligands as precatalysts for the polymerization of styrene: Electronic and steric substituent effects," *Dalt. Trans.*, 44, 368–376, 2015.

[59] Y. Su, Y. Zhao, J. Gao, Q. Dong, B. Wu, and X. J. Yang, "Alkali metal and zinc complexes of a bridging 2,5-diamino-1,4- benzoquinonediimine ligand," *Inorg. Chem.*, 51, 5889–5896, 2012.

[60] J. P. Taquet, O. Siri, P. Braunstein, and R. Welter, "Dinuclear nickel and palladium complexes with bridging 2,5-diamino-1,4- benzoquinonediimines: Synthesis, structures, and catalytic oligomerization of ethylene," *Inorg. Chem.*, 45, 4668–4676, 2006.

[61] K. Biradha, A. Ramanan, and J. J. Vittal, "Coordination polymers versus metal-organic frameworks," *Cryst. Growth Des.*, 9, 2969–2970, 2009.

[62] K. Wada, K. Sakaushi, S. Sasaki, and H. Nishihara, "Multielectron-transfer-based rechargeable energy storage of two-dimensional coordination frameworks with

non-innocent ligands," *Angew. Chemie - Int. Ed.*, 57, 8886–8890, 2018.

[63] J. Park, M. Lee, D. Feng, Z. Huang, A. C. Hinckley, A.Yakovenko,X. Zou, Y. Cui, Z. Bao., "Stabilization of hexaaminobenzene in a 2D conductive metal-organic framework for high power sodium storage," *J. Am. Chem. Soc.*, 140, 10315–10323, 2018.

[64] Y. Chen, M. Tang, Y. Wu, X. Su, X. Li, S. Xu, S. Zhuo, J. Ma, D. Yuan, C. Wang, W. Hu., "A One-dimensional π–d conjugated coordination polymer for sodium storage with catalytic activity in Negishi coupling," *Angew. Chemie - Int. Ed.*, 58, 14731–14739, 2019.

[65] A. Shchyrba, C. Wäckerlin, J. Nowakowski, S. Nowakowska, J. Björk, S. Fatayer, J. Girovsky, T. Nijs, S. C. Martens, A. Kleibert., "Controlling the dimensionality of on-surface coordination polymers via endo- or exoligation," *J. Am. Chem. Soc.*, 136, 9355–9363, 2014.

[66] F. Huttmann, N. Schleheck, N. Atodiresei, and T. Michely, "On-Surface synthesis of sandwich molecular nanowires on graphene," 139, 9895-9900, 2017.

[67] M. Koudia, E. Nardi, O. Siri, and M. Abel, "On-surface synthesis of covalent coordination polymers on micrometer scale," *Nano Res.*, 10, 933–940, 2017.

[68] M. Telychko J. Su, A. Gallardo Y. Gu, J. I. Mendieta, D. Qi, A. Tadich, Sh. Song, P. Lyu, Zh. Qiu, H. Fang, M. Joo Koh, J. Wu, P. Jelínek, , "Strain-induced isomerization in one-dimensional metal–organic chains," *Angew. Chemie*, 18764–18770, 2019.

[69] C. Krull, M. Castelli, P. Hapala, D. Kumar, A. Tadich, M. Capsoni, M. T. Edmonds, J. Hellerstedt, S. A. Burke, P. Jelinek, A. Schiffrin. , "Iron-based trinuclear metal-organic nanostructures on a surface with local charge accumulation," *Nat. Commun.*, 9, 1–7, 2018.

[70] A. Cahlík, J.Hellerstedt, J. I. Mendieta-Moreno, M. Švec, V. M. Santhini, S. Pascal, D. Soler-Polo, S. I. Erlingsson, K. Výborný, P. Mutombo, O. Marsalek, O. Siri, P. Jelínek, "Significance of nuclear quantum effects in hydrogen bonded molecular chains," *ACS Nano*, 2021. DOI: 10.1021/acsnano.1c02572.

[71] V. M. Santhini, C. Wäckerlin, A. Cahlík, M. Ondráček, S. Pascal, A.Matěj, O. Stetsovych, P. Mutombo, P. Lazar, O. Siri, P. Jelínek , "1D Coordination π–d Conjugated Polymers with Distinct Structures Defined by the Choice of the Transition Metal: Towards a New Class of Antiaromatic Macrocycles," *Angew. Chemie - Int. Ed.*, 60, 439–445, 2021.

[72] J. Guo, J.-T Lü, Y. Feng, J. Chen, J. Peng, Z. Lin, X. Meng, Z. Wang, X-Z Li, E.-G. Wang, Y, Jiang, "Nuclear quantum effects of hydrogen bonds probed by tip-enhanced inelastic electron tunneling," *Science*. 352, 321–325, 2016.

[73] X. Z. Li, B. Walker, and A. Michaelides, "Quantum nature of the hydrogen bond," *Proc. Natl. Acad. Sci. U. S. A.*, 108, 6369–6373, 2011.

[74] L. Wang, S. D. Fried, S. G. Boxer, and T. E. Markland, "Quantum delocalization of protons in the hydrogen-bond network of an enzyme active site," *Proc. Natl. Acad. Sci. U. S. A.*, 111, 18454–18459, 2014.

[75] P. Liljeroth, J. Repp, and G. Meyer, "Current-induced hydrogen tautomerization and conductance switching of naphthalocyanine molecules," *Science*. 317, 1203–1206, 2007.

[76] T. Kumagai F. Hanke, S. Gawinkowski, J. Sharp, K. Kotsis, J. Waluk, M. Persson and L. Grill *et al.*, "Controlling intramolecular hydrogen transfer in a porphycene molecule with single atoms or molecules located nearby," *Nat. Chem.*, 6, 41–46, 2014.

[77] J. N. Ladenthin, T. Frederiksen, M. Persson, J. C. Sharp, S. Gawinkowski, J. Waluk & Takashi Kumagai*et al.*, "Force-induced tautomerization in a single molecule," *Nat. Chem.*, 8, 935–940, 2016.

[78] H. Böckmann, S. Liu, J. Mielke, S. Gawinkowski, J. Waluk, L. Grill, M. Wolf, and T. Kumagai, "Direct observation of photoinduced tautomerization in single molecules at a metal surface," *Nano Lett.*, 16, 1034–1041, 2016.

[79] Y. Litman, J. O. Richardson, T. Kumagai, and M. Rossi, "Elucidating the nuclear quantum dynamics of intramolecular double hydrogen transfer in Porphycene," *J. Am. Chem. Soc.*, 141, 2526–2534, 2019.

[80] L. Gross, F. Mohn, N. Moll, P. Liljeroth, and G. Meyer, "The chemical structure of a molecule resolved by atomic force microscopy," *Science.*, 325, 1110–1114, 2009.

[81] X. Meng, J. Guo, J. Peng, J. Chen, Z. Wang, J.-R. Shi, X.-Z. Li, E.-G. Wang and Y. Jiang , "Direct visualization of concerted proton tunnelling in a water nanocluster," *Nat. Phys.*, 11, 235–239, 2015.

[82] K.-H. Meiwes-Broer, "Electronic level structure of metal clusters at surfaces," Springer, Berlin, Heidelberg, 2000, 151–173.

[83] M. Bieri, M.-T. Nguyen, O. Gröning, J. Cai, M. Treier, K. Ait-Mansour, P. Ruffieux, C. A. Pignedoli, D. Passerone, Marcel Kastle, Klaus Müllen, and Roman Fasel, "Two-dimensional polymer formation on surfaces: Insight into the roles of precursor mobility and reactivity," *J. Am. Chem. Soc.*, 132, 16669–16676, 2010.

[84] P. Hapala, G. Kichin, C. Wagner, F. S. Tautz, R. Temirov, and P. Jelínek, "Mechanism of high-resolution STM/AFM imaging with functionalized tips," *Phys. Rev. B - Condens. Matter Mater. Phys.*, 90, 1–9, 2014.

[85] D. Geuenich, K. Hess, F. Köhler, and R. Herges, "Anisotropy of the induced current density (ACID), a general method to quantify and visualize electronic delocalization," *Chemical Reviews*, 105, 3758–3772, 2005.

[86] T. M. Krygowski and M. K. Cyrański, "Structural aspects of aromaticity," *Chemical Reviews*, 101, 1385–1419, 2001.

[87] M. Mauksch and S. B. Tsogoeva, "Strict correlation of HOMO topology and magnetic aromaticity indices in d-Block metalloaromatics," *Chem. - A Eur. J.*, 24, 10059–10063, 2018.

[88] D. W. Szczepanik and M. Solà, "Electron delocalization in planar metallacycles: Hückel or Möbius aromatic?," *ChemistryOpen*, 8, 219–227, 2019.

[89] V. M. Santhini, O. Stetsovych, M. Ondráček, J. I. Mendieta Moreno, P. Mutombo, B. de la Torre, M. Švec, J. Klívar, I. G. Stará, H. Vázquez, I. Starý, and P. Jelínek, "On-Surface Synthesis of Polyferrocenylene and its Single-Chain Conformational and Electrical Transport Properties," *Adv. Funct. Mater.*, 31, 2006391-410, 2021.

[90] T. J. Kealy and P. L. Pauson, “A new type of organo-iron compound,” *Nature*, 168, 1039–1040, 1951.

[91] S. A. Miller, J. A. Tebboth, and J. F. Tremaine, “Dicyclopentadienyliron,” *J. Chem. Soc.*, 632–635, 1952.

[92] G. Wilkinson, M. Rosenblum, M. C. Whiting, and R. B. Woodward, “The structure of iron bis-cyclopentadienyl,” *J. Am. Chem. Soc.*, 74, 2125–2126, 1952.

[93] R. Leber, L.E. Wilson, P. Robaschik, M.S. Inkpen, D.J. Payne, N.J. Long, T. Albrecht, C.F. Hirjibehedin, S. Heutz, “High-vacuum deposition of biferrocene thin films on room-temperature substrates,” *Chem. Mater.*, 29, 8663–8669, 2017.

[94] S. Barlow and D. O’Hare, “Metal–metal interactions in linked metallocenes,” *Chem. Rev.*, 97, 637–670, 1997.

[95] D. Astruc, “Why is ferrocene so exceptional?,” *Eur. J. Inorg. Chem.*, 2017, 6–29, 2017.

[96] P. Laszlo and R. Hoffmann, “Ferrocene: Ironclad history or rashomon tale?,” *Angew. Chemie - Int. Ed.*, 39, 123–124, 2000.

[97] E. W. Neuse, “Macromolecular ferrocene compounds as cancer drug models,” *J. Inorg. Organomet. Polym.*, 15, 3–32, 2005.

[98] H. Rosenberg, “Metallocene polymers,” *J. Macromol. Sci. Part C*, 4, 1–145, 1970.

[99] P. Nguyen, P. Gómez-Elipe, and L. Manners, “Organometallic polymers with transition metals in the main chain,” *Chem. Rev.*, 99, 1515–1548, 1999.

[100] P. V. Roling and M. D. Rausch, “Formation of 1,2-oligomeric ferrocenes from ullmann reactions of iodoferrocenes,” *J. Organomet. Chem.*, 141, 195–204, 1977.

[101] R. D. A. Hudson, “Ferrocene polymers: Current architectures, syntheses and utility,” *J. Organomet. Chem.*, 637–639, 47–69, 2001.

[102] M. D. Rausch, P. V. Roling, and A. Siegel, “Formation of ferrocene oligomers from mixed Ullmann reactions of halogenoferrocenes,” *Chem. Commun.*, 502–503, 1970.

[103] G. M. Brown, T. J. Meyer, D. O. Cowan, C. LeVanda, F. Kaufman, P. V. Rolling, and M. D. Rausch., "Oxidation-State and Electron-Transfer Properties of Mixed-Valence 1,1'-Polyferrocene Ions," *Inorg. Chem.*, 14, 506–511, 1975.

[104] H. Nishihara, T. Hirao, K. Aramaki, and K. Aoki, "Redox properties of hepta(1,1′-dihexylferrocenylene)," *Synth. Met.*, 84, 935–936, 1997.

[105] H. Nishihara, "Redox chemistry and functionalities of conjugated ferrocene systems," *Adv. Inorg. Chem.*, 53, 41–86, 2002.

[106] E. W. Neuse, "Polymetallocenylenes-Recent developments," *J. Macromol. Sci. Part A - Chem.*, 16, 3–72, 1981.

[107] K. H. Pannell, V. I. Imshennik, Y. V. Maksimov, M. N. Il'ina, H. K. Sharma, V. S. Papkov, and I. P. Suzdalev, "Mixed-valence behavior in an iodine complex of a ferrocenylenesilylene polymer," *Chem. Mater.*, 17, 1844–1850, 2005.

[108] Y. Sasaki, "Mixed Valence, Semiconducting Ferrocene- Containing Polymers," 2, 46–55, 1976.

[109] I. Manners, "Ring-opening polymerization of metallocenophanes," *Adv. Mater.*, 6, 68–71, 1994.

[110] I. Manners, "Putting metals into polymers," *Science* 294, 1664–1666, 2001.

[111] M. A. Hussein and A. M. Asiri, "Organometallic ferrocene- and phosphorus-containing polymers: Synthesis and characterization," *Des. Monomers Polym.*, 15, 207–251, 2012.

[112] M. A. Vorotyntsev and S. V. Vasilyeva, "Metallocene-containing conjugated polymers," *Adv. Colloid Interface Sci.*, 139, 97–149, 2008.

[113] P. Kruse, E. R. Johnson, G. A. DiLabio, and R. A. Wolkow, "Patterning of vinylferrocene on H-Si(100) via self-directed growth of molecular lines and STM-induced decomposition," *Nano Lett.*, 2, 807–810, 2002.

[114] J. G. Rodriguez and A. Lafuente, "Stereo chain template effect on the synthesis of conjugated 1 , 1 ´ -di- [p- (X-phenyl) ethenyl] ferrocenes," *ARKIVOC*, 2007, 195–208, 2007.

[115] E. W. Neuse and L. Bednarik, “Polyferrocenylenes by oxidative coupling of 1,1′-dilithioferrocene with Cu^{2+} Ion,” *Transit. Met. Chem.*, 4, 87–94, 1979.

[116] E. W. Neuse and R. K. Crossland, “Metallocene polymers XIX. Polyferrocenylenes,” *J. Organomet. Chem.*, 7, 344–347, 1967.

[117] R. A. Musgrave *et al.*, “Main-chain metallopolymers at the static-dynamic boundary based on nickelocene,” *Nat. Chem.*, 9, 743–750, 2017.

[118] X. Xiao, D. Brune, J. He, S. Lindsay, C. B. Gorman, and N. Tao, “Redox-gated electron transport in electrically wired ferrocene molecules,” *Chem. Phys.*, 326, 138–143, 2006.

[119] H. Nishihara and M. Murata, “Electron transfer in ferrocene-containing π-conjugated polymers,” *J. Inorg. Organomet. Polym.*, 15, 147–156, 2005.

[120] D. O. Cowan, J. Park, C. U. Pittman, Y. Sasaki, T. K. Mukherjee, and N. A. Diamond, “Semiconducting polymers. Mixed valence ferrocene-ferricenium polymers,” *J. Am. Chem. Soc.*, 94, 5110–5112, 1972.

[121] K. Sanechika, T. Yamamoto, and A. Yamamoto, “Dehalogenation polymerization of 1, 1’-Dihaloferrocene with magnesium as a new convenient synthetic route to Poly(1, 1’-ferrocenylene),” *Polym. J.*, 13, 255–261, 1981.

[122] G. Britain, “Ferrocenes Review,” *J.Orgnaometal. Chem.,* 123, 273-334, 1976.

[123] P. Park, A. J. Lough, and D. A. Foucher, “Copper-mediated polycondensations of substituted diiodoferrocenes and bis(stannyl)ferrocenes: Synthesis and properties of soluble polyferrocenylenes containing trimethylsilyl or methyl groups,” *Macromolecules*, 35, 3810–3818, 2002.

[124] R. Whitfield, N. P. Truong, D. Messmer, K. Parkatzidis, M. Rolland, and A. Anastasaki, “Tailoring polymer dispersity and shape of molecular weight distributions: Methods and applications,” *Chem. Sci.*, 10, 8724–8734, 2019.

[125] K. Sanechika, T. Yamamoto, and A. Yamamoto, “Dehalogenation polymerization of 1,1’-dihaloferrocene with magnesium as a new convenient synthetic route to poly(1,1’-ferrocenylene).,” *Polymer Journal*, 13, 255–261, 1981.

[126] C. K. Krug, Q. Fan, F. Fillsack, J. Glowatzki, N. Trebel, L.J. Heuplick, T. Koehler, J.M. Gottfried, "Organometallic ring: Vs. chain formation beyond kinetic control: Steering their equilibrium in two-dimensional confinement," *Chem. Commun.*, 54, 9741–9744, 2018.

[127] J. Liu, Q. Chen, Q. He, Y. Zhang, X. Fu,Y. Wang, D. Zhao, W. Chen, G.Q. Xud and K. Wu, "Bromine adatom promoted C-H bond activation in terminal alkynes at room temperature on Ag(111)," *Phys. Chem. Chem. Phys.*, 20, 11081–11088, 2018.

[128] M. Ormaza, R. Robles, N. Bachellier, P. Abufager, N. Lorente, and L. Limot, "On-surface engineering of a magnetic organometallic nanowire," *Nano Lett.*, 16, 1588–593, 2016.

[129] Q. Fan, C. Wang, Y. Han, J. Zhu, J. Kuttner, G. Hilt, J.M. Gottfried, "Surface-assisted formation, assembly, and dynamics of planar organometallic macrocycles and zigzag shaped polymer chains with C-Cu-C bonds," *ACS Nano*, 8, 709–718, 2014.

[130] Y. Ma, Y. Dai, W. Wei, and B. Huang, "Engineering intriguing electronic and magnetic properties in novel one-dimensional staircase-like metallocene wires," *J. Mater. Chem. C*, 1, 941–946, 2013.

[131] M. Ormaza, R. Robles, N. Bachellier, P.Abufager, N.Lorente, and L. Limot, "On-surface engineering of a magnetic organometallic nanowire," *Nano Lett.*, 16, 588–593, 2016.

[132] T. Knaak, M. Gruber, S. Puhl, F. Benner, A. Escribano, J. Heck, R. Berndt, "Interconnected cobaltocene complexes on metal surfaces," *J. Phys. Chem. C*, 121, 26777–26784, 2017.

[133] J. Choi and P. A. Dowben, "Cobaltocene adsorption and dissociation on Cu(111)," *Surf. Sci.*, 600, 2997–3002, 2006.

[134] J. L. Lin, H. Rauscher, A. Kirakosian, F. J. Himpsel, and P. A. Dowben, "Selective adsorption of metallocenes on clean and chemically modified si(111) surfaces," *J. Appl. Phys.*, 86, 5492–5496, 1999.

[135] R. C. Quardokus, N. A. Wasio, R. P. Forrest, C. S. Lent, S. A. Corcelli, J. A. Christie,

K. W. Hendersona and S. A. Kandel, “Adsorption of diferrocenylacetylene on Au(111) studied by scanning tunneling microscopy,” *Phys. Chem. Chem. Phys.*, 15, 6973, 2013.

[136] G. Zhang *et al.*, “Electronic structure-transport property relationships of polyferrocenylene, polyferrocenylacetylene, and polyferrocenylsilane,” *J. Phys. Chem. C*, vol. 114, no. 20, pp. 9469–9477, 2010.

[137] J. Berger, K. Kośmider, O. Stetsovych, M. Vondráček, P. Hapala, E.J. Spadafora, M. Švec, P. Jelínek, “Study of ferrocene dicarboxylic acid on substrates of varying chemical activity,” *J. Phys. Chem. C*, 120, 21955–21961, 2016.

[138] L. Shen, S. W. Yang, M. F. Ng, V. Ligatchev, L. Zhou, and Y. Feng, “Charge-transfer-based mechanism for half-metallicity and ferromagnetism in one-dimensional organometallic sandwich molecular wires,” *J. Am. Chem. Soc.*, 130, 13956–13960, 2008.

[139] P. Byszewski, Z. Klusek, S. Pierzgalski, S. Datta, E. Kowalska, and M. Popławska, “STM/STS observation of ferrocene derivative adduct to C_{60} on HOPG,” *J. Electron Spectros. Relat. Phenomena*, 130, 25–32, 2003.

[140] R.F. Dou, D.Y. Zhong, W.C. Wang, K. Wedeking, G. Erker, L. Chi, H. Fuchs, “Structures and stability of ferrocene derivative monolayers on Ag(110): Scanning tunneling microscopy study,” *J. Phys. Chem. C*, 111, 12139–12144, 2007.

[141] P. Saha, K. Yadav, S. Chacko, A. T. Philip, R. Ramapanicker, and T. G. Gopakumar, “Controlling growth to one dimension in nanoislands of ferrocene-sugar derivatives,” *J. Phys. Chem. C*, 120, 9223–9228, 2016.

[142] M. Lackinger, “Surface-assisted Ullmann coupling,” *Chem. Commun.*, 53, 7872–7885, 2017.

[143] T. Y. Dong, W. Y. Lee, P. T. Su, L. S. Chang, and K. J. Lin, “Electron transfer in mixed-valence polyferrocenium cations: Preparation, electrochemistry, and ^{57}Fe Mössbauer characteristics,” *Organometallics*, 17, 3323–3330, 1998.

[144] G. Kuang, S.Z. Chen, W. Wang, T. Lin, K. Chen, X. Shang, P.N. Liu, N. Lin, “Resonant charge transport in conjugated molecular wires beyond 10 nm range,”

J. Am. Chem. Soc., 138, 11140–11143, 2016.

[145] R. Pawlak, J.G. Vilhena, P. D'Astolfo, X. Liu, G. Prampolini, T. Meier, T. Glatzel, J.A. Lemkul, R. Häner, S. Decurtins, A. Baratoff, R. Pérez, S.X. Liu, E.Meyer, "Sequential bending and twisting around C-C Single bonds by mechanical lifting of a pre-adsorbed polymer," *Nano Lett.*, 20, 652–657, 2019.

[146] L. Lafferentz, F. Ample, H. Yu, S. Hecht, C. Joachim, and L. Grill, "Conductance of a single conjugated polymer as a continuous function of its length," *Science* 323, 1193–1198, 2009.

[147] S. H. Choi, C. Risko, M. Carmen Ruiz Delgado, B. Kim, J. L. Brédas, and C. Daniel Frisbie, "Transition from tunneling to hopping transport in long, conjugated oligo-imine wires connected to metals," *J. Am. Chem. Soc.*, 132, 4358–4368, 2010.

[148] H. C. Seong, B. S. Kim, and C. D. Frisbie, "Electrical resistance of long conjugated molecular wires," *Science,* vol. 320, 1482–1486, 2008.

List of Figures

pA); (f) NiQDI (100 mV, 42 pA); (g) CoQDI zoom-in (-400 mV, 32 pA); (h) NiQDI zoom-in (100 mV, 42 pA).

2.5 From left to right: sequentially acquired STM images of chain manipulation experiment of FeQDI wire on Au(111). Scanning parameters: 40x40 nm^2, 300 mV, 20 pA.

2.6 STM images (a) FeQDI on Cu(111) and (b) Cu_2QDI wires on Cu(111). The overview images are 200 × 200 nm^2 and the zoom-in images are 8 × 2 nm^2. Scanning parameters (bias voltage, tunnel current set point): (a) (500 mV, 20 pA); (b) (1.2 V, 10 pA); Zoom- in: (c) (-200 mV, 50 pA); (d) (300 mV, 30 pA).

2.7 High resolution constant height nc-AFM images with CO modified tip of (a) FeQDI wires on Au(111) (b) FeQDI wires on Cu(111) and (c) Cu_2QDI wires on Cu(111). Both (a) and (b) exhibit the same characteristic "x-like" contrast feature (marked by red arrows) between adjacent molecular units and same lattice periodicity, clearly distinct from the contrast and the periodicity between the neighbouring molecules in Cu_2QDI wires. [Scale bars: 1 nm; A_{osc} = 50 pm].

2.8 Simulated AFM images of (a) FeQDI/Au(111) (b) Cu_2QDI/Cu(111) coordination polymers.

2.9 (a) ACID plot of FeQDI/Cu(111), black arrow indicating the clockwise direction of current density vectors for better clarity. (b) ACID plot of Cu_2QDI/Cu(111), black arrow indicating the anticlockwise direction of current density vectors for better clarity. The molecular planes are placed perpendicular to the magnetic field vector. Small green arrows are computed current density vectors.

2.10 (a) NICS grid of FeQDI/Au(111) (b) NICS grid of Cu_2QDI/Cu(111).

2.11 Scheme depicting the bonds and resonating structures of the 12 membered macrocycle in Cu_2QDI wires on Cu(111).

3.1 Scheme of structure of polyferrocenylenes (PFc).

3.2 Scheme of on surface synthesis of poyferrocenylene on Ag(111) surface.

3.3 Fc_2-I_2 on Ag(111). (a) STM image of Fc_2-I_2 islands on surface. (b) STM image of Fc_2-I_2 islands along the step edges. Scanning Parameters: (a) (500 mV, 10 pA, 100 × 100 nm^2); (b) (500 mV, 10 pA, 50 × 50 nm^2).

3.4 Fc_2-I_2 on Ag(111). (a) STM image of Fc_2-I_2 islands on Ag(111) surface. (b) Disordered phase in the island. (c) Ordered phase in the Fc_2-I_2 islands. (d) I/V (red curve) and corresponding

dI/dV (blue curve) taken over Fc_2-I_2 island. Vertical blue lines highlight the band gap of ~2.4V on the molecules before reaction. Scanning Parameters: (a) (500 mV, 10 pA, 100 × 100 nm^2); (b, c) (500 mV, 10 pA, 10 × 10 nm^2).

3.5 STM topographies of polyferrocenylene samples prepared at different annealing temperature/time on Ag(111). (a) Annealing temperature: ~400K, 10min: some polyferrocenylene nanowires, but also high amount of unordered ferrocene clusters on the surface. (b) Annealing temperature: ~400K, 20min: majority of the ferrocene forms ordered polyferrocenylene nanowires. (c) Annealing temperature ~425K, 20 min: ferrocene desorbs from the surface, only Iodine remains. Scanning Parameters: (a) (900 mV, 10 pA, 100 × 100 nm^2); (b) (500 mV, 10 pA, 100 × 100 nm^2); (c) (500 mV, 10 pA, 100 × 100 nm^2), inset: 50 × 50 nm^2.

3.6 STM topography images of polyferrocenylene islands on Ag(111). Scanning Parameters: (a) (-300 mV, 20 pA, 70 × 70 nm^2); (b) (30 mV, 10 pA, 80 × 80 nm^2); (c) (-300 mV, 20 pA, 40 × 40 nm^2).

3.7 (a) STM overview of the two different polyferrocenylene islands. (b, c) Zoom-in images of the polyferrocenylene nanowires in the two islands. Scanning Parameters: (a) (-100 mV, 20 pA, 40 × 40 nm^2); (b) and (c) constant height current images: 1 mV, 3 × 3 nm^2.

3.8 Structural arrangement of polyferrocenylenes in self-assembled islands. (a, b) High resolution constant height frequency shift images for meander and zig-zag PFc islands with different molecular arrangement respectively. Molecular periodicity highlighted by a and b vectors. (c, d) Simulated AFM images for the respective PFc islands. Proposed top view ball-stick models are superimposed over the simulated images. Scanning Parameters: (a,b) (10 mV, A_{osc} = 50 pm, 2 × 2 nm^2). Model: Fe, C, H, Ag atoms correspond to the yellow, green, white, and silver colors, respectively.

3.9 Incommensurability of the PFc islands. (a,b) Constant height AFM images over PFc islands with two different stacking. Bottom panel: constant height AFM images of atomically resolved Ag(111) lattice of the substrate. Red and blue lines highlight the high symmetry axis of the Ag(111) substrate and PFc rows, respectively. There is mismatch between high symmetry axes of the substrate and the Fc islands: 11.5° for stacking (a) and 5° for stacking (b). Black circles added to highlight the atomic periodicity of the Ag(111) lattice. All images: 3 × 3 nm^2.

3.10 PFc nanowires self-assembled into 2D Islands: (a-d) STM sequence of successful interaction between scanning probe and molecular island. (a-b) Pulling a chain of polyferrocenylene in the island. (c-d) Separation of the polymer chain from the island. (e) STM image of a

separated island from the Ag(111) step edge. (f) High resolution constant height current image highlighting the interconnection between the molecular rows in the separated island. Tentative ball-stick model of the interconnection is superimposed. Scanning Parameters: (a, b) (500 mV, 20 pA, 10 × 5 nm^2); (c, d) (500 mV, 20 pA, 70 × 35 nm^2; (e) (300 mV, 20 pA, 14 × 14 nm^2); (f) constant height zoom: 5 mV, 5 × 5 nm^2. Model: Fe, C, H atoms correspond to the yellow, green and white colors, respectively.

3.11 Polyferrocenylene nanowire length. (a) STM image of a manipulated polyferrocenylene nanowire. Bottom panel same as top but with superimposed black dots and red lines to highlight the order of the 69 ferrocene units in the nanowire. (b) STM image of a manipulated ~50 nm long polyferrocenylene nanowire. Black line highlights the nanowire. Scanning parameters: (a) (500 mV, 20 pA, 20 × 5 nm^2); (b) (500 mV, 10 pA, 50 × 50 nm^2).

3.12 Structural arrangement individual PFc chain: (a) High resolution constant height frequency shift image of the isolated polymer chain. Molecular periodicity highlighted by a_3 vector. (b) Simulated AFM image of the isolated polymer chain showing perpendicular and inclined configurations. Proposed top view ball-stick models are superimposed over the simulated images. Scanning parameters: (a) (10 mV, A_{osc} = 50 pm, 8 × 4 nm^2). Model: Fe, C, H, Ag atoms correspond to the yellow, green, white, and silver colors, respectively.

3.13 (a) Series of consecutive constant height STM images on a PFc chain. After each image the chain is perturbed with the scanning probe switching parts of the chain between standing and side configurations. (b) Constant height AFM image with CO functionalized tip on the transition area between side and standing configurations of the PFc chain. (c) *Δf(z)* spectroscopy taken on the Fc units corresponding to side (blue curve) and standing (red curve) configurations. Fc units in standing configuration are protruding 90 pm more from the surface than in side configuration. Fc molecules models for side and standing configurations are shown in the inset. Scanning Parameters: (a) (30 mV, 10 × 10 nm^2); (b) (10 mV, A_{osc} = 50 pm, 8 × 4 nm^2).

3.14 dI/dV measured on the two islands (a, b) and the free chain of polyferrocenylene (c, d). Red, blue, green, and black graphs correspond to measurements on meander island, zig-zag island, inclined configuration and perpendicular configuration of the free chain, respectively. The positions of spectroscopy are marked in (a-c) by crosses of the same color. Scanning Parameters: (a, b) (10 mV, A_{osc} = 50 pm, 2 × 2 nm^2); (c) (10 mV, A_{osc} = 50 pm, 8 × 4 nm^2).

3.15 KPFM measurements. (a) STM image of Fc_2-I_2 island in disordered phase. (b) *Δf(V)* spectroscopy taken on Fc_2-I_2 island (red curve) and Ag(111) substrate (blue curve). (c) STM

image post Ullmann coupling reaction. PFc nanowire is separated out from the island. (d) *Δf(V)* spectroscopies taken on Fc island (green), different parts of PFc nanowire (standing configuration: red and side configuration: blue, respectively) and Ag(111) substrate (black). Scanning Parameters: (a) (500 mV, 20 pA, A_{osc} = 50 pm, 30 × 30 nm^2); (c) (50 mV, 10 pA, A_{osc} = 50 pm, 25 × 25 nm^2). Crosses in the STM images mark the positions where spectroscopies of same color were taken. Vertical lines in spectroscopy curves mark the value of contact potential difference (CPD). Corresponding CPD values shown in the insets.

3.16 Lifting experiments with polyferrocenylene: (a) Simulated model of the partially lifted polyferrocenylene. Inset: STM image of an isolated polyferrocenylene before the lift. (b) Two *Δf(z)* data sets taken during the polyferrocenylene lifting experiment highlighted in red and blue colors. (c) I/V spectroscopy curves taken for the red data set for different z-distances: vertical lines of the same color in (b). Threshold bias defined from the 0.5 pA cut-off current marked as black crosses. (d) Threshold bias for the red and blue data set as a function of the lifting distance. Black crosses correspond to the bias threshold estimated from the curves shown in (c). Scanning Parameters: (a) inset: 500 mV, 20 pA, 15 × 15 nm^2, A_{osc} = 50 pm. (b, d) The z=0 height corresponds to the tip-sample height at STM feedback parameters of V= 1 mV, I = 3nA on clean Ag(111) surface for a metallic terminated tip.

Appendix I: Quinoid Based Metal-Coordinated Polymers in Solution

Synthesis of 2,5-diamino-1,4 -benzoquinonediimines (2HQDI)

The synthesis of **2HQDI** in literature [1] has been carried out with commercially available tetraaminobenzene tetrahydrochloride. Here, this commercial reagent has been prepared in the laboratory and then used to synthesise **2HQDI**.

1,5-Difluoro-2,4-dinitrobenzene (m=1.5 g, 7.349 mmol) was dissolved in acetone (v=30ml) and tert-butyl amine (v=3.85 ml, 36.7 mmol) was added dropwise. The solution was placed under reflux at 56 ^{o}C for 1 hour 30 minutes. The solution is washed with ethanol and precipitate (m=2.085 g, 6.718 mmol) was isolated by vacuum filtration to obtain N,N'-tert butyl-2,4-dinitrobenzene-1,5- diamine.

Tin(II) dichloride dihydrate (m=9.11g, 40.308 mmol) was dissolved in 35% conc. HCL (v=32 ml) by ultrasonication for 1 min. N,N'-tert butyl-2,4-dinitrobenzene-1,5- diamine (m=2.085 g, 6.718 mmol) was added to the HCl solution and sonicated at a temperature of 40 ^{o}C for 30 minutes. Then the solution was stirred and heated to 120 ^{o}C for 15 minutes. The solution was left at room temperature and then in refrigerator for at least 1 hour. The solution becomes transparent with a white solid settled at the bottom. The solution was washed with HCL followed by diethyl ether and white wet precipitate was obtained by vacuum filtration. The precipitate was vacuum dried overnight and a white solid tetraaminobenzene tetrahydrochloride (m=1.84 g, 6.478 mmol) was obtained.

The synthesis protocol for 2,5-diamino-1,4-benzoquinonediimine described in the literature[1] was followed at this stage. The synthesised tetraaminobenzene tetrahydrochloride (m=1.84 g, 6.478 mmol) was placed in methanol (212 ml) and ceasium carbonate (m= 8.442 g, 25.912 mmol) was added as base and stirred at room temperature for 30 minutes. The precipitate was isolated by filtration and dried under vacuum. The resulting brown solid **2HQDI** (m= 410 mg, 46.5 % yield) was obtained. The NMR (**Figure 1**) is comparable to the data in the literature[1].

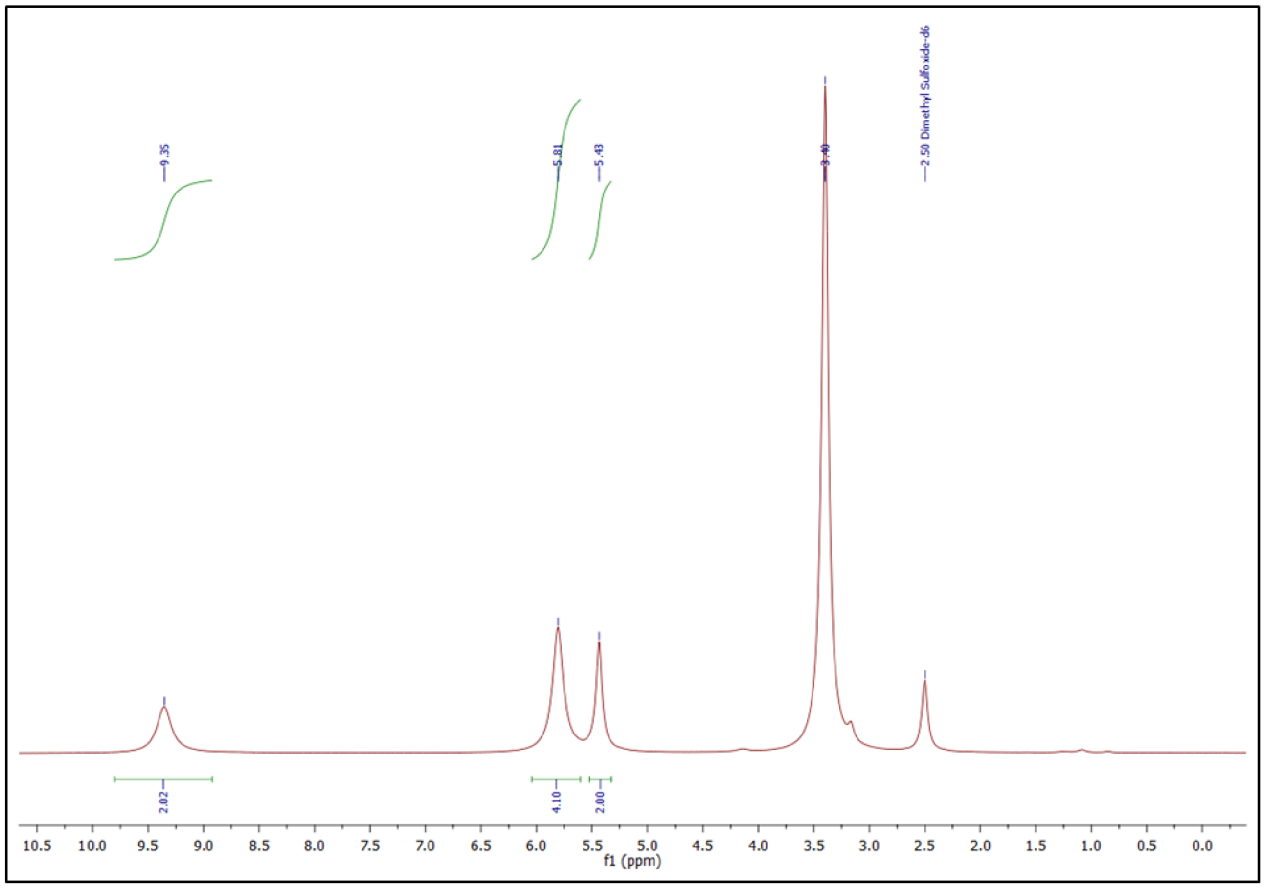

Figure 2: NMR spectra of **2HQDI** in DMSO synthesised using Cs_2CO_3 as base. ^1H NMR (250 MHz, $(CD_3)_2SO$): δ = 5.43 (s, 2H), 5.81 (br s, 4H), 9.35 (s, 2H).

Another synthesis process of **2HQDI** was carried out using potassium carbonate as the base. The synthesised tetraaminobenzene tetrahydrochloride (m=1.685 g, 5.94 mmol) was placed in methanol (195 ml). The base potassium carbonate (m= 3.28 g, 23.76 mmol) was added and stirred at room temperature for 30 minutes. The precipitate was isolated by filtration and dried under vacuum. The resulting brown solid **2HQDI** (m= 157.9 mg) was obtained. The yield was low but the NMR (**Figure 2**) was pretty much similar and pure as the process specified in literature.

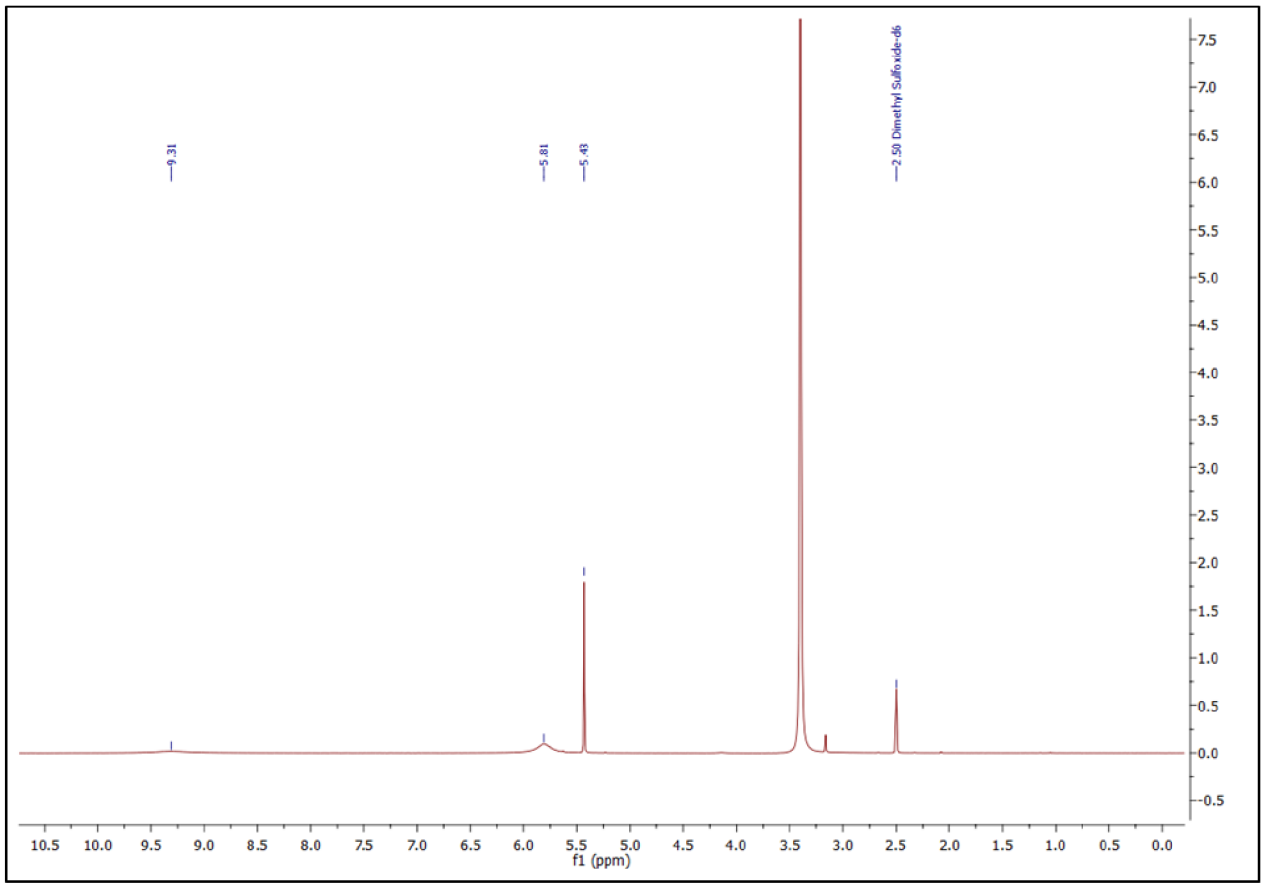

Figure 2: NMR spectra of **2HQDI** in DMSO synthesised using K_2CO_3 as base. 1H NMR (250 MHz, $(CD_3)_2SO$): δ = 5.43 (s, 2H), 5.81 (br s, 4H), 9.31 (s, 2H).

Synthesis of Dinuclear Complexes

The synthesis protocol of **dinuclear complexes** is similar as described in the literature [1] for nickel complexes.

Iron (II) acetylacetonate {$Fe(acac)_2$} (2 equiv.) was added to a suspension of **2HQDI** (1 equiv.) in toluene and stirred at room temperature for 2 hours. The resulting precipitate was isolated by vacuum filtration to give **FeQDI dinuclear complex** as shown in **Scheme 1.**

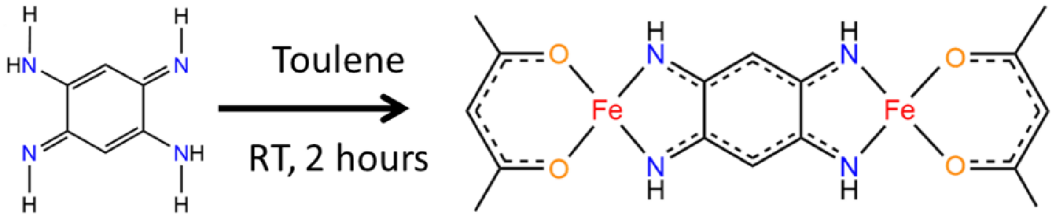

Scheme 1: Synthesis of FeQDI dinuclear complex

The UV-Vis-NIR absorption studies (**Figure 3.a**) have been carried out to study the stepwise metalation reactions of FeQDI complex in Dimethyl Sulfoxide (DMSO). There has not been any absorption shift in the peak during the 3 days, just an increase in the absorption peak at around 800 nm. The band around 400 nm is the adsorption of

2HQDI molecule in DMSO. To confirm the structure of the complex formed, MALDI analysis **(Figure 3.b, c)** has been carried out. It clearly shows a mixture of compounds, and the FeQDI dinuclear complex is very low in quantity.

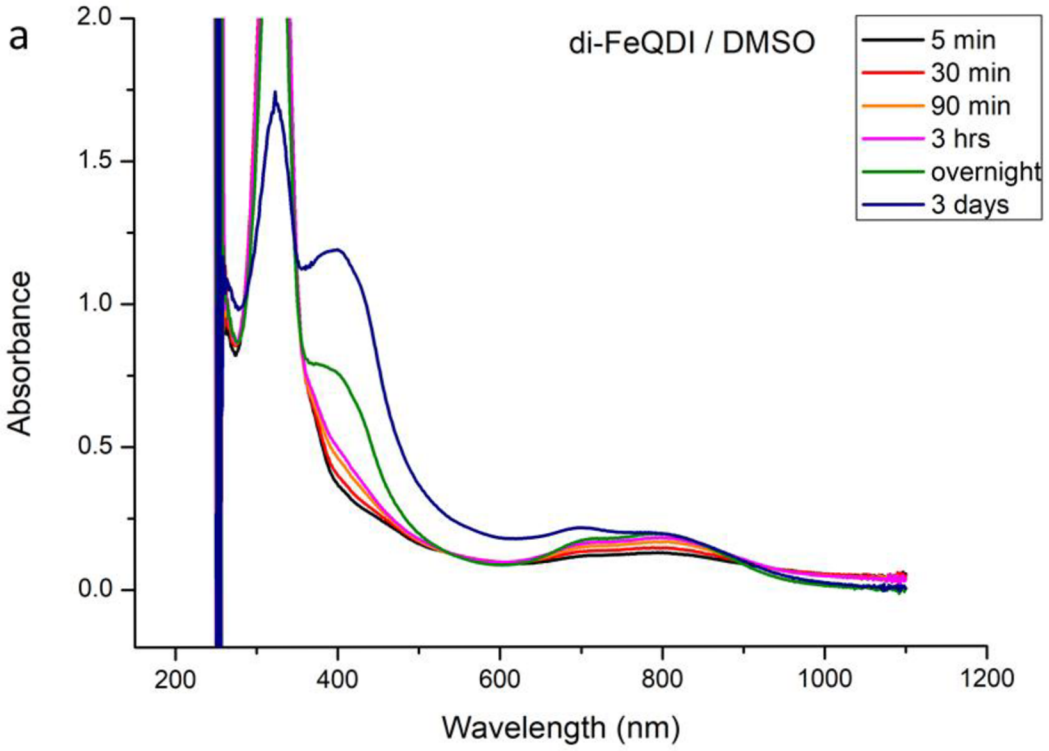

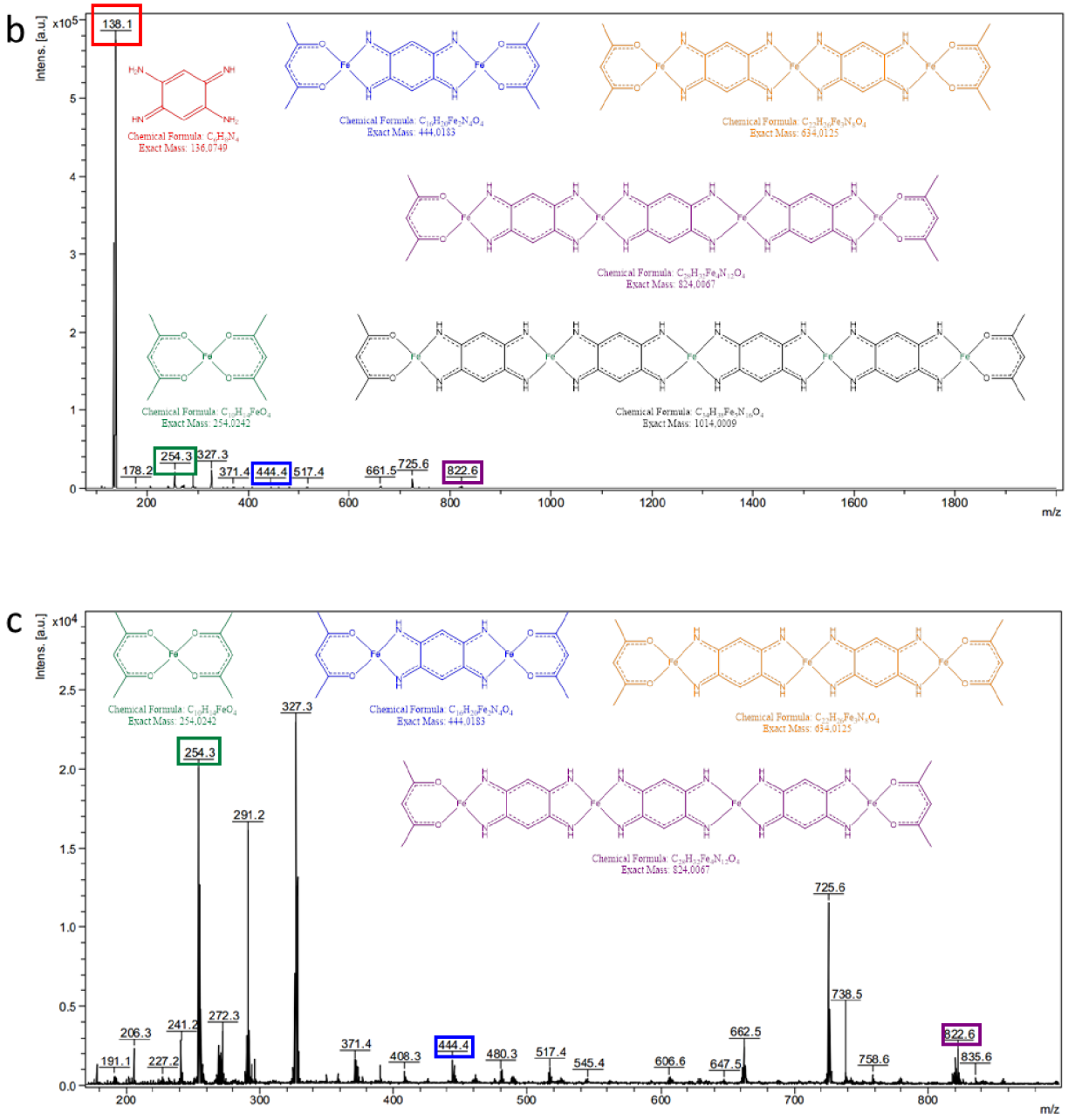

Figure 3: (a) UV-Vis-NIR absorption studies of FeQDI dinuclear complex in DMSO. **(b)** MALDI Analysis (Positive). **(c)** Zoom-in MALDI spectra

The procedure was repeated with Cobalt (II) acetylacetonate {$Co(acac)_2$} as shown in **Scheme 2** as shown in **Scheme 2** to form **CoQDI dinuclear complex.**

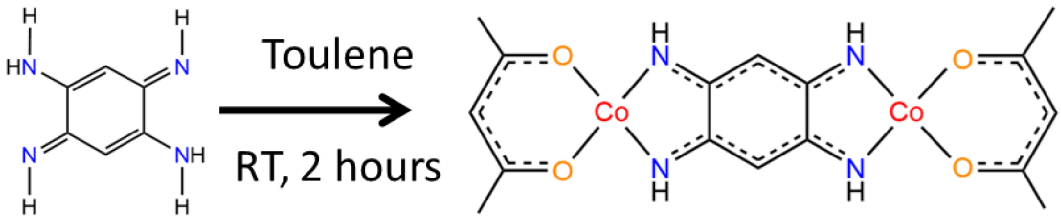

Scheme 2: Synthesis of CoQDI dinuclear complex

The stepwise metalation reactions of CoQDI dinuclear complex has been observed with UV-Vis-NIR absorption studies (**Figure 4.a**) in DMSO. No peak has been observed in the Visible-NIR region to confirm the occurrence of polymerization reaction. The band around 400 nm is the absorption of **2HQDI** molecule in DMSO which also decreases during 3 days, indicating a degradation of the complex. The MALDI analysis (**Figure 4.b, c**) shows mostly the presence of CoQDI dinuclear complex in very low proportions, but it is not stable to study the absorption kinetics.

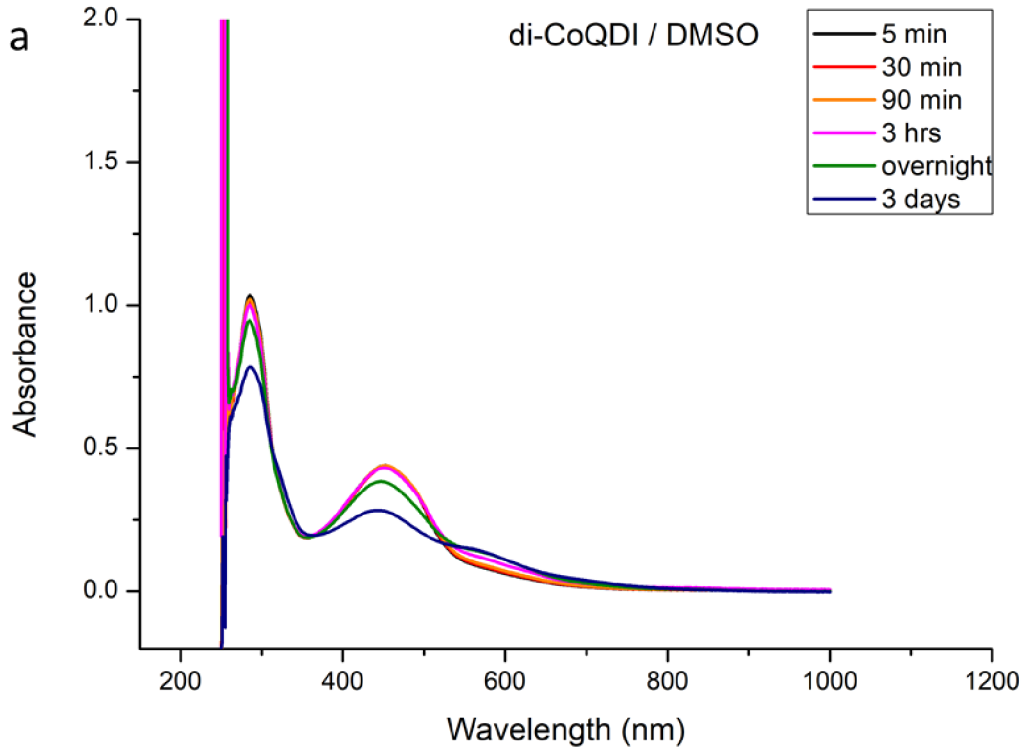
a
di-CoQDI / DMSO
5 min
30 min
90 min
3 hrs
overnight
3 days
Absorbance
Wavelength (nm)
2.0
1.5
1.0
0.5
0.0
200
400
600
800
1000
1200

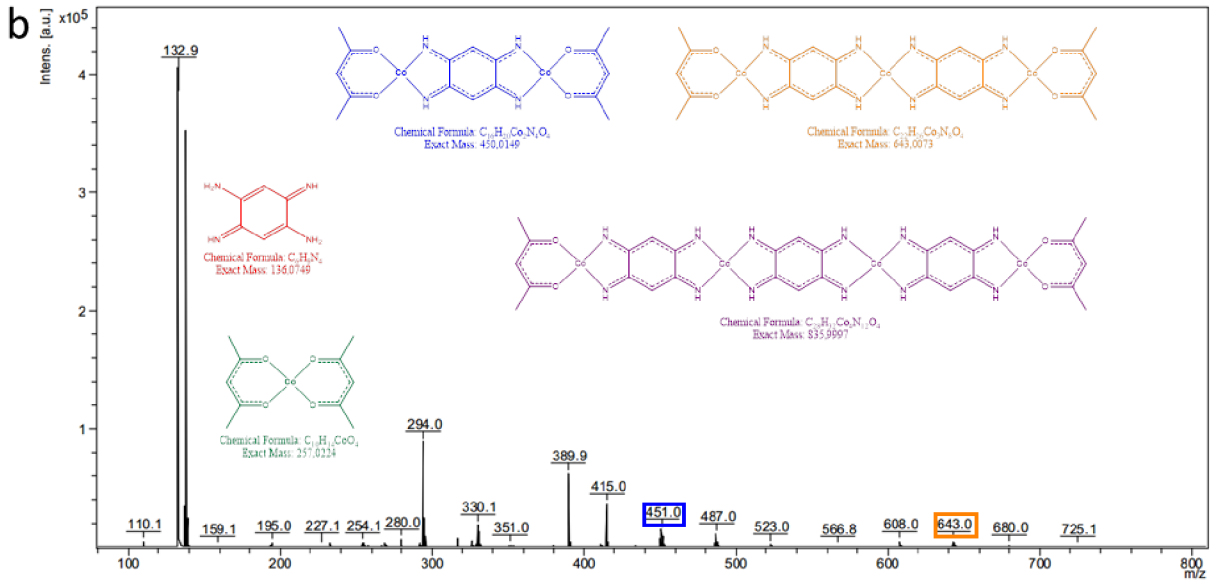
b
Intens. [a.u.]
x10^5
132.9
294.0
389.9
415.0
451.0
487.0
643.0
110.1
159.1
195.0
227.1
254.1
280.0
330.1
351.0
523.0
566.8
608.0
680.0
725.1
m/z

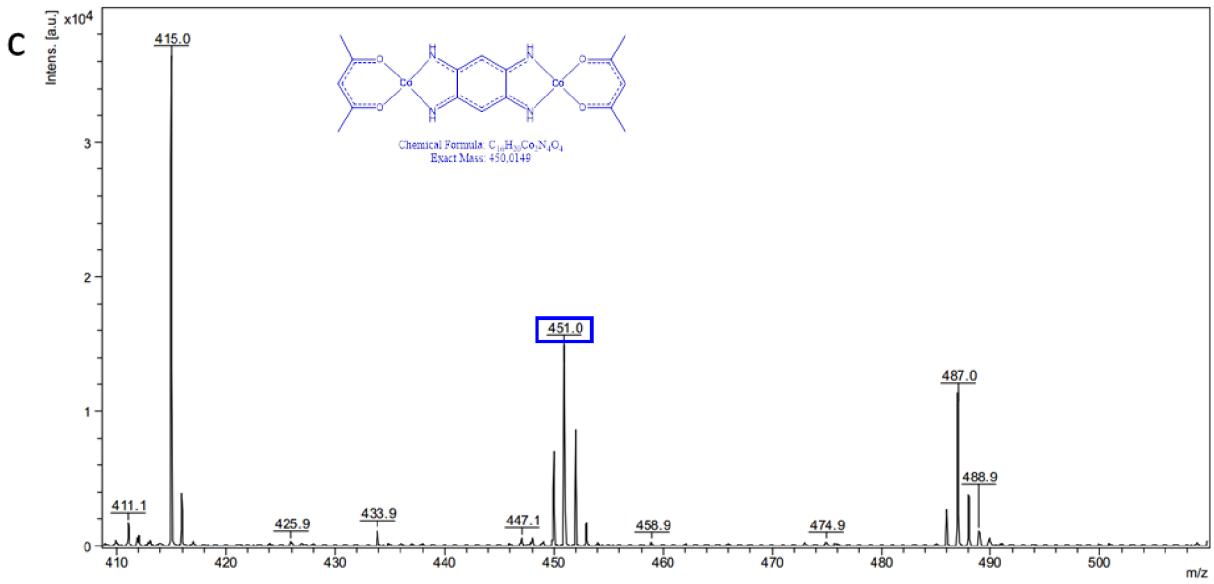

Figure 4: (a) UV-Vis-NIR absorption studies of CoQDI dinuclear complex in DMSO. **(b)** MALDI Analysis (Positive). **(c)** Zoom-in MALDI spectra

The synthesis of **CuQDI dinuclear complex** was carried out as described above using Copper (II) acetylacetonate {$Cu(acac)_2$} and **2HQDI** precursor molecules, as described in **Scheme 3**.

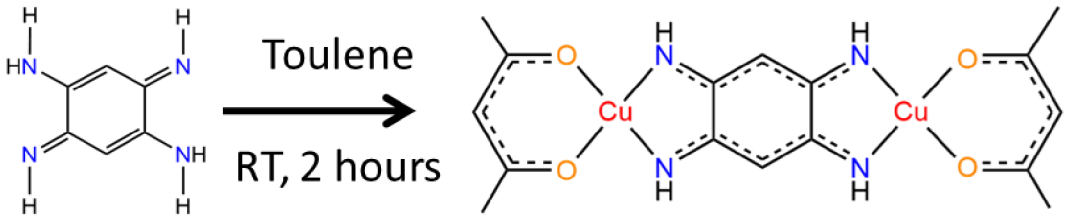

Scheme 3: Synthesis of CuQDI dinuclear complex

The UV-Vis-NIR spectrum (**Figure 5.a**) of CuQDI dinuclear complex shows a poly-absorption peak in DMSO around 400 nm characteristic of **2HQDI** molecule. The absorption peak decreases with time indicating the degradation of the complex. There is no evidence of metalation reactions in the Vis-NIR region. The MALDI analysis (**Figure 5.b, c**) shows that there is a very low proportion of CuQDI dinuclear complex which cannot be characterized as one.

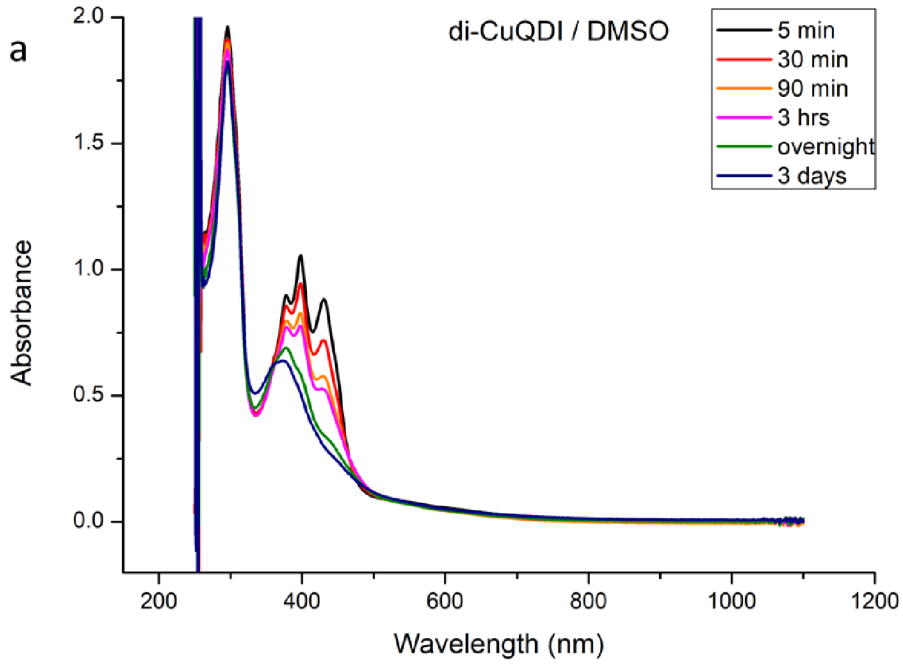

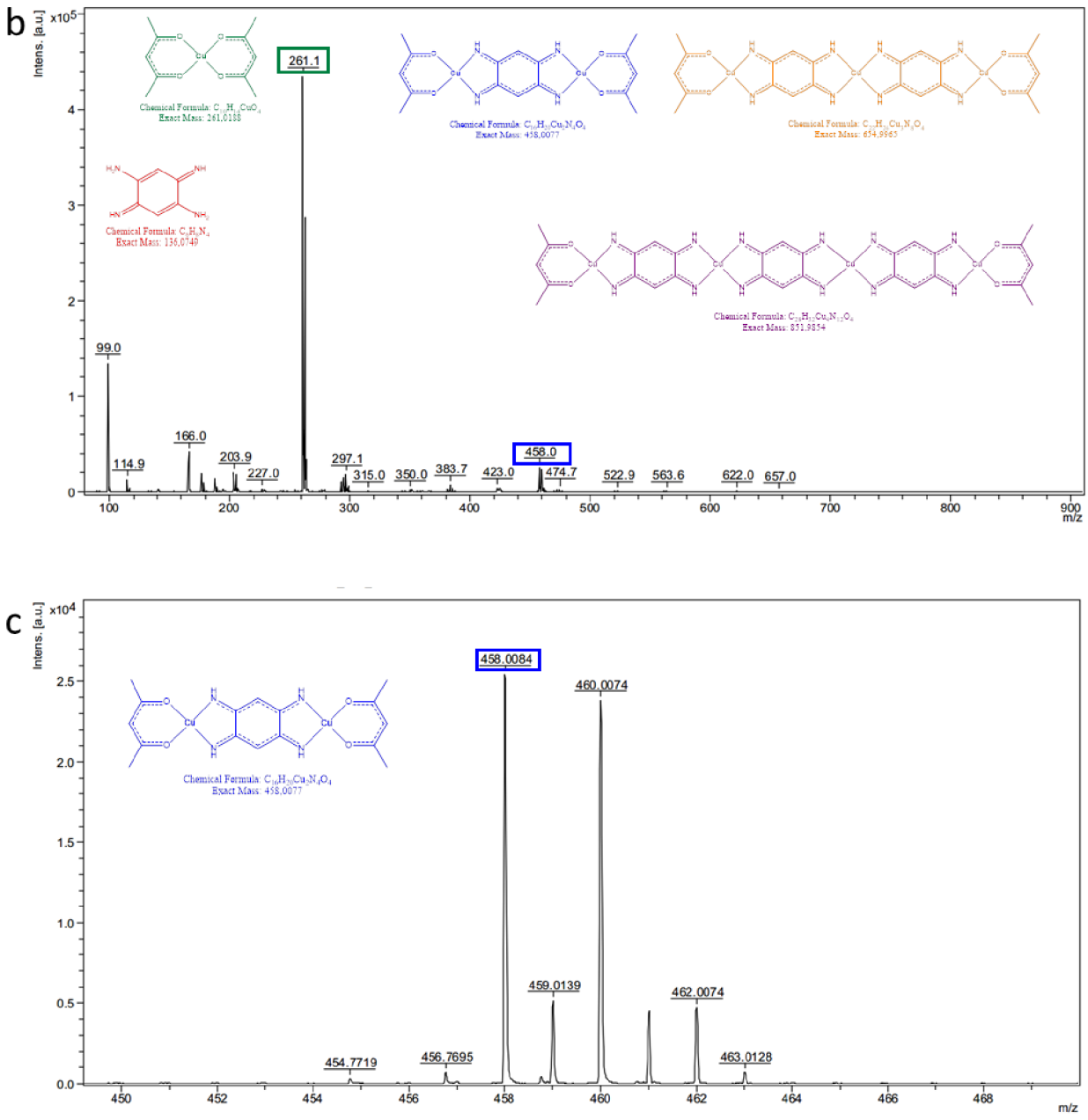

Figure 5: (a) UV-Vis-NIR absorption studies of CuQDI dinuclear complex in DMSO. **(b)** MALDI Analysis (Positive). **(c)** Zoom-in MALDI spectra

Synthesis of Trinuclear Complexes

The synthesis of **trinuclear complexes** has been carried out in the same way as described for nickel trinuclear complexes in the literature [1].

Iron (II) acetylacetonate {$Fe(acac)_2$} (2 equiv.) was added to a suspension of **2HQDI** (1 equiv.) in tetrahydrofuran (THF) and stirred at room temperature for 24 hours. The solvent was evaporated under vacuum with the help of rotary evaporator. Then chloroform was added to the resulting solid and the precipitate was obtained by vacuum filtration to give **FeQDI trinuclear complex**.

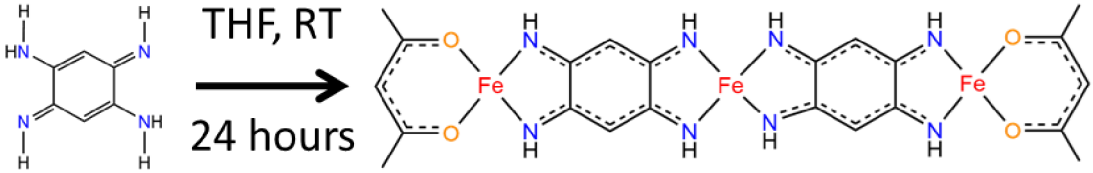

Scheme 4: Synthesis of FeQDI trinuclear complex

The FeQDI trinuclear complex in DMSO show a mild evolution of the UV-Vis-NIR (**Figure 6.a**) absorption band around 800 nm in the Vis-NIR region during the three days but there are no signs of metalation reactions occurring in this process. There is a very low absorbance peak for **2HQDI** molecule around 400 nm which confirm the coordination reaction. The MALDI spectrum (**Figure 6.b, c**) shows very low proportions of tetranuclear complex rather than trinuclear complex.

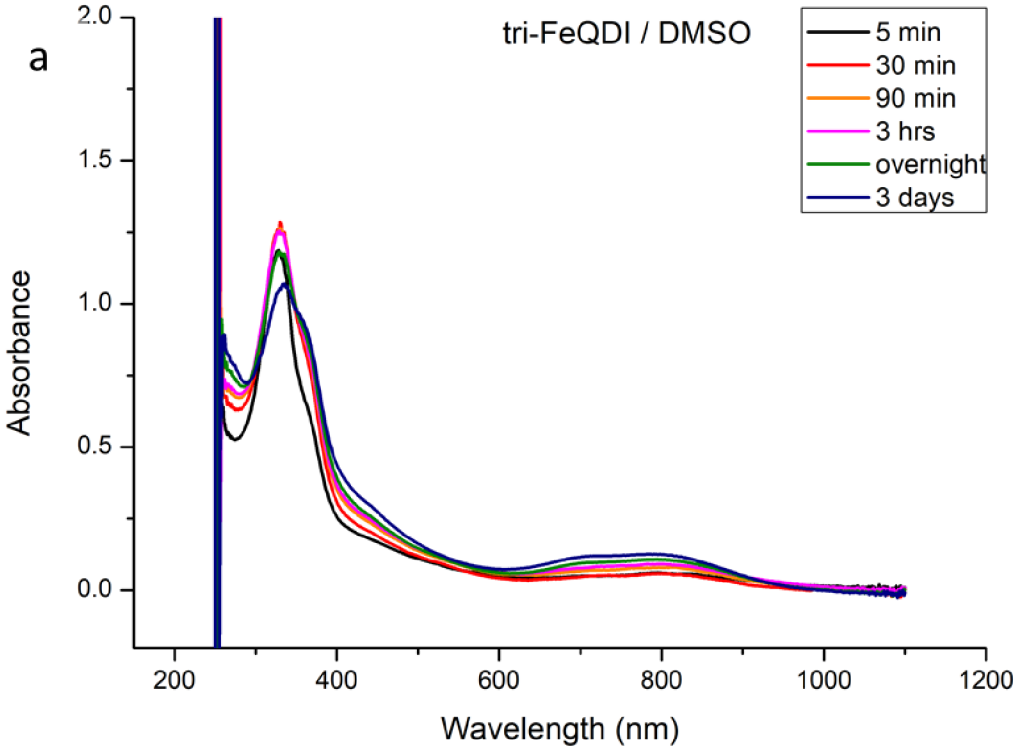
a
tri-FeQDI / DMSO
5 min
30 min
90 min
3 hrs
overnight
3 days
Absorbance
Wavelength (nm)
2.0
1.5
1.0
0.5
0.0
200
400
600
800
1000
1200

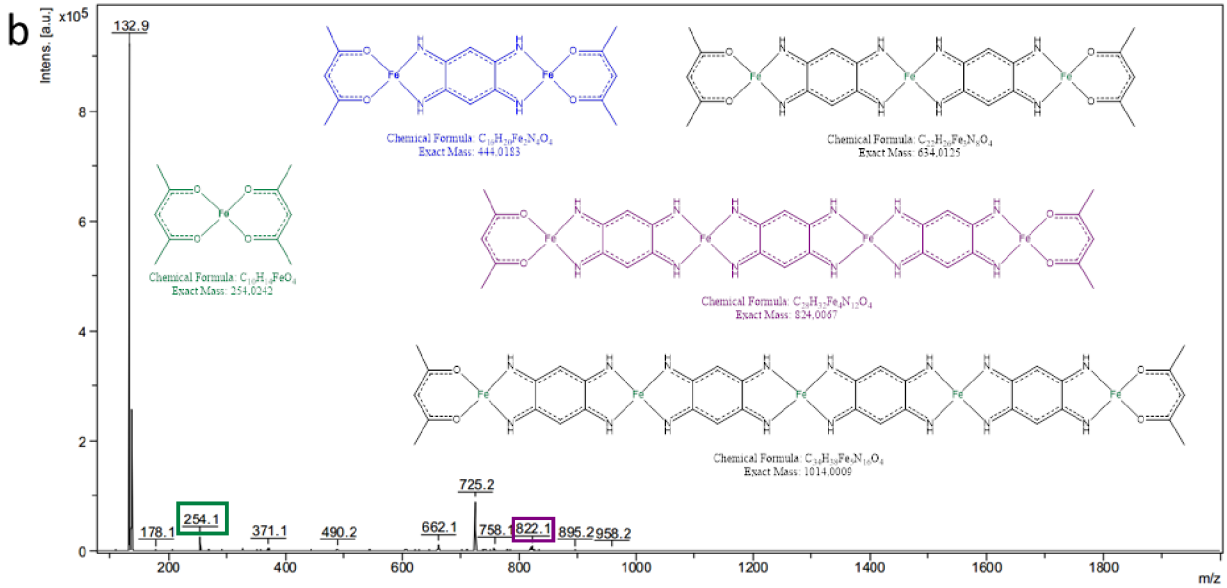
b
Intens. [a.u.]
x10^5
132.9
254.1
178.1
371.1
490.2
662.1
725.2
758.1
822.1
895.2
958.2
m/z
Chemical Formula: C11H7FeO4
Exact Mass: 254.0242
Chemical Formula: C15H10Fe2N4O4
Exact Mass: 444.0183
Chemical Formula: C22H10Fe3N6O4
Exact Mass: 654.0125
Chemical Formula: C29H13Fe4N8O4
Exact Mass: 824.0067
Chemical Formula: C36H16Fe5N10O4
Exact Mass: 1014.0009

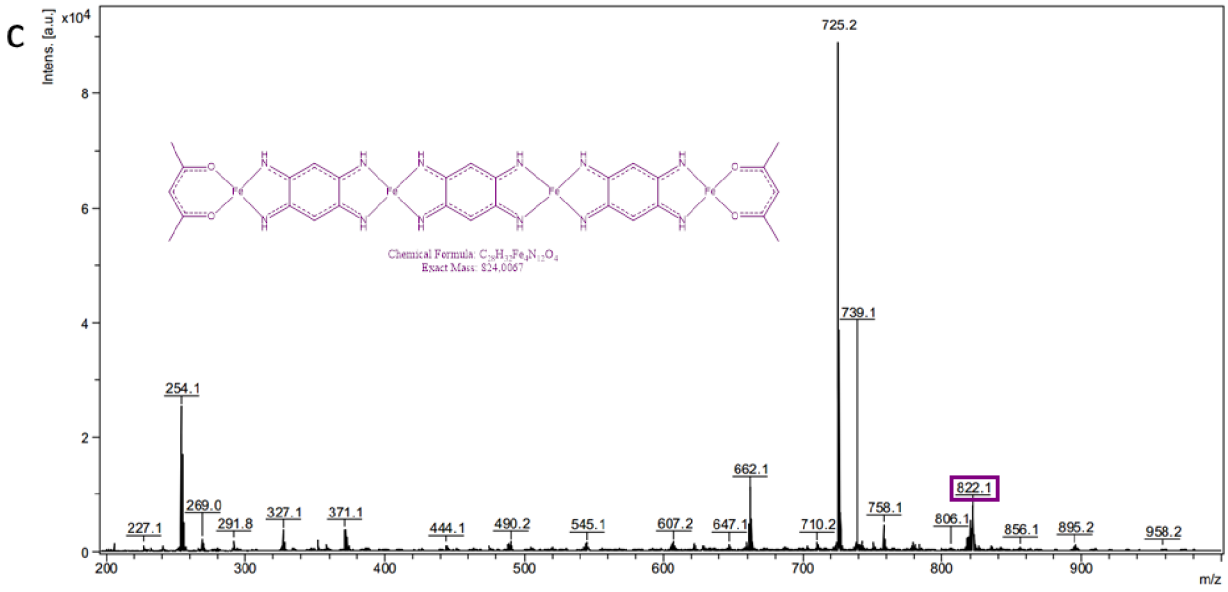

Figure 6: (a) UV-Vis-NIR absorption studies of FeQDI trinuclear complex in DMSO. **(b)** MALDI Analysis (Positive). **(c)** Zoom-in MALDI spectra

Similar synthesis procedure was repeated with Cobalt (II) acetylacetonate {$Co(acac)_2$ to form **CoQDI trinuclear complex (Scheme 5).**

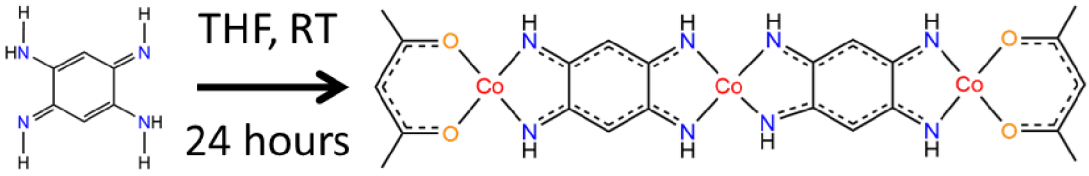

Scheme 5: Synthesis of CoQDI trinuclear complex

The UV-Vis-NIR absorption analysis (**Figure 7.a**) clearly shows an evolution of the absorption band around 800 nm and degradation of the quinone absorption band, indicating a change in the structure of the complex. But there is again no metalation reaction occurring in this case, as there is no absorption shifts occurring in NIR region. The MALDI analysis (**Figure 7.b, c**) shows very low proportions of CoQDI dinuclear complex, but the absorption studies do not behave the same.

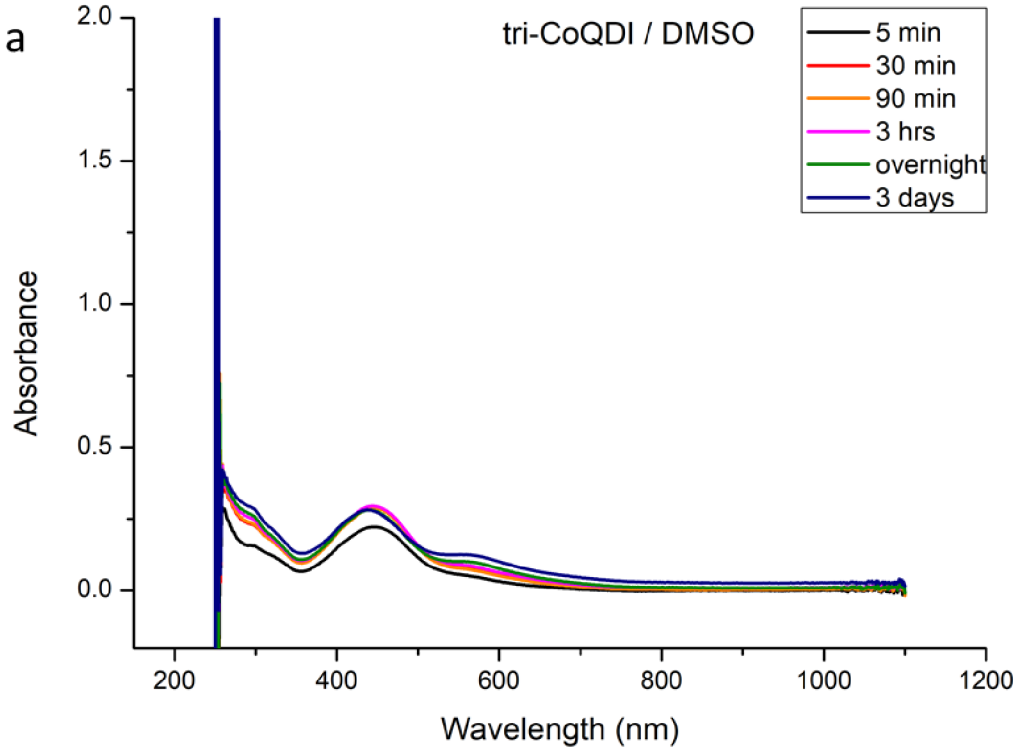

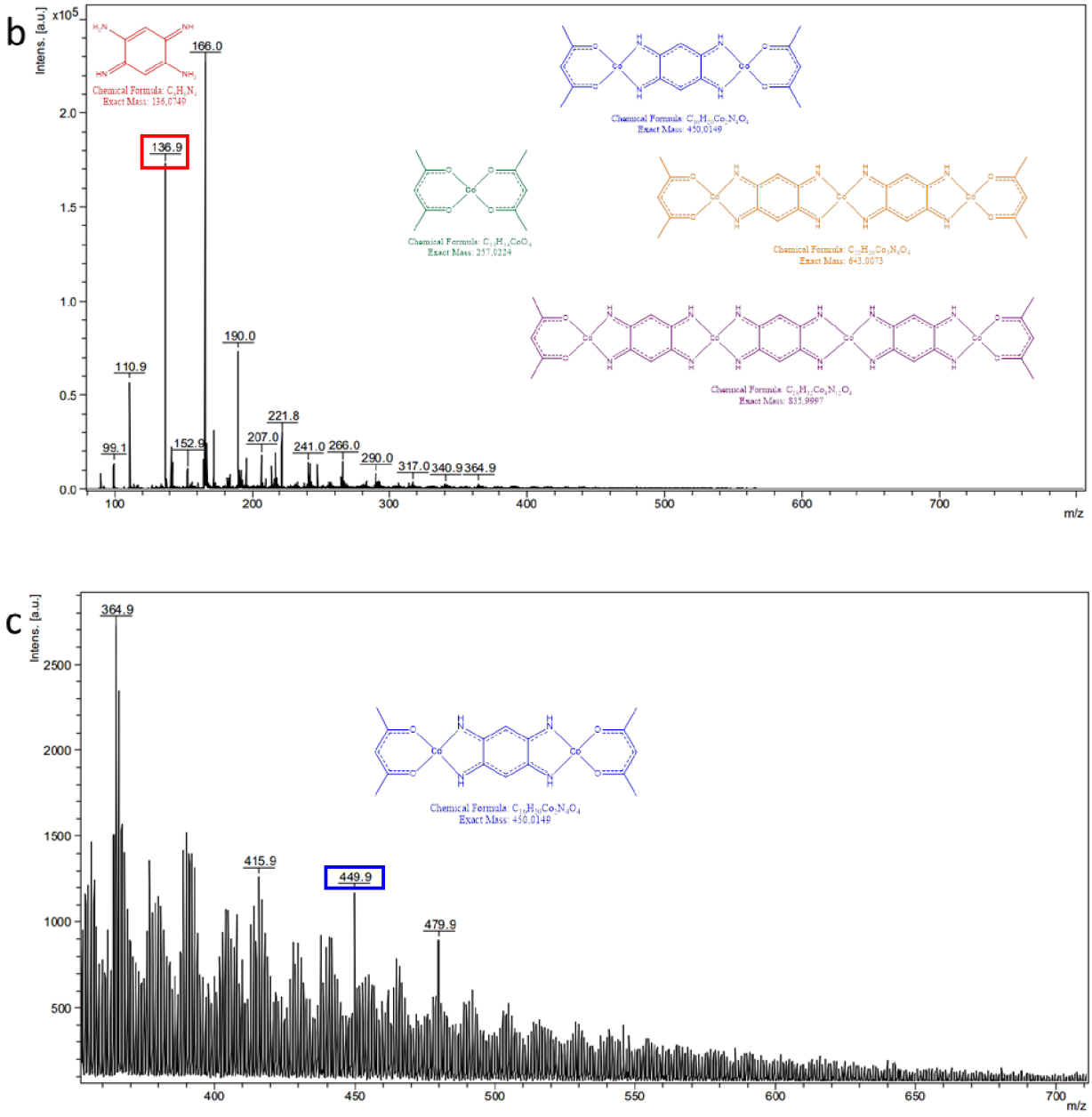

Figure 7 : (a) UV-Vis-NIR absorption studies of CoQDI trinuclear complex in DMSO. **(b)** MALDI Analysis (Positive). **(c)** Zoom-in MALDI spectra

The synthesis procedure similar to FeQDI, was carried out with **2HQDI** and Copper (II) acetylacetonate {$Cu(acac)_2$} to form **CuQDI trinuclear complex (Scheme 6)**.

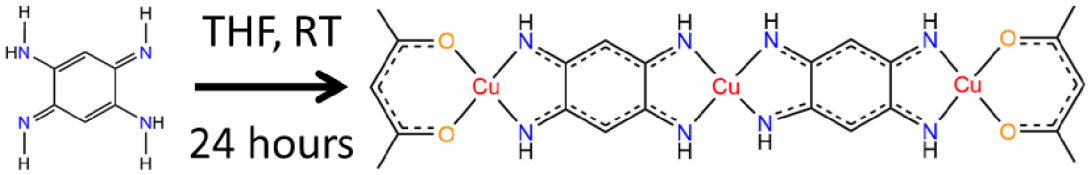

Scheme 6: Synthesis of CuQDI trinuclear complex

The UV-Vis-NIR absorption studies in DMSO (**Figure 8.a**) do not show any metalation reaction bands and also the quinone absorption bands are not clear enough. The MALDI analysis (**Figure 8.b, c**) show very low proportion of CuQDI dinuclear complex and not the trinuclear complex.

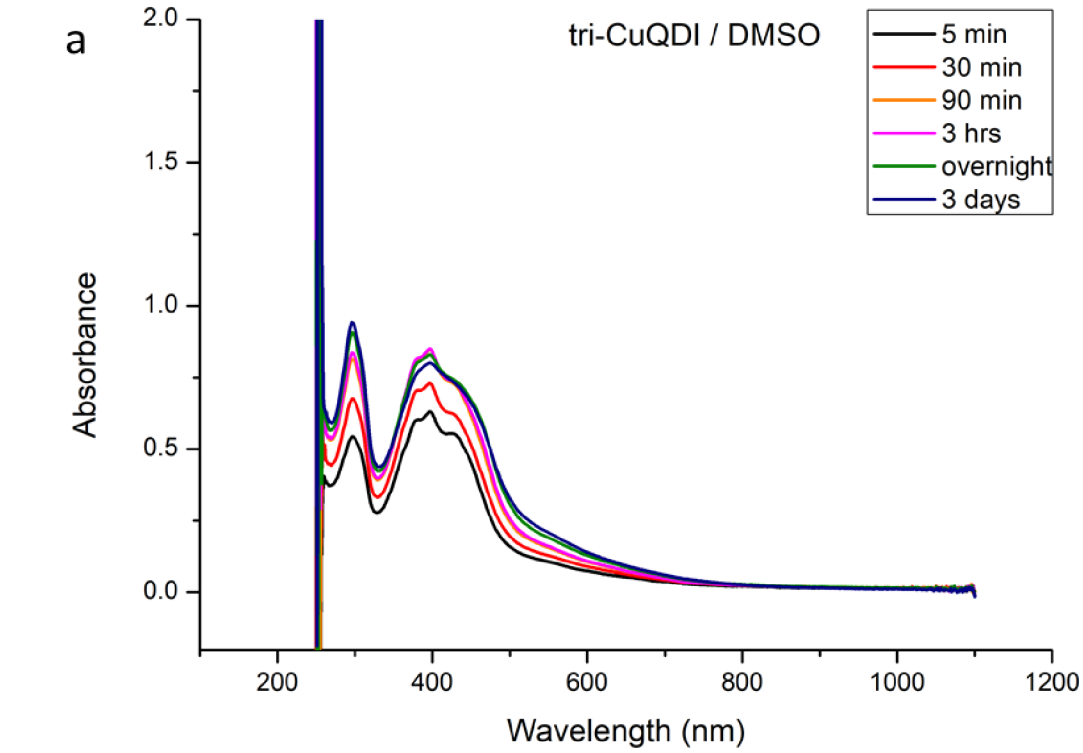
a
tri-CuQDI / DMSO
5 min
30 min
90 min
3 hrs
overnight
3 days
Absorbance
Wavelength (nm)
2.0
1.5
1.0
0.5
0.0
200
400
600
800
1000
1200

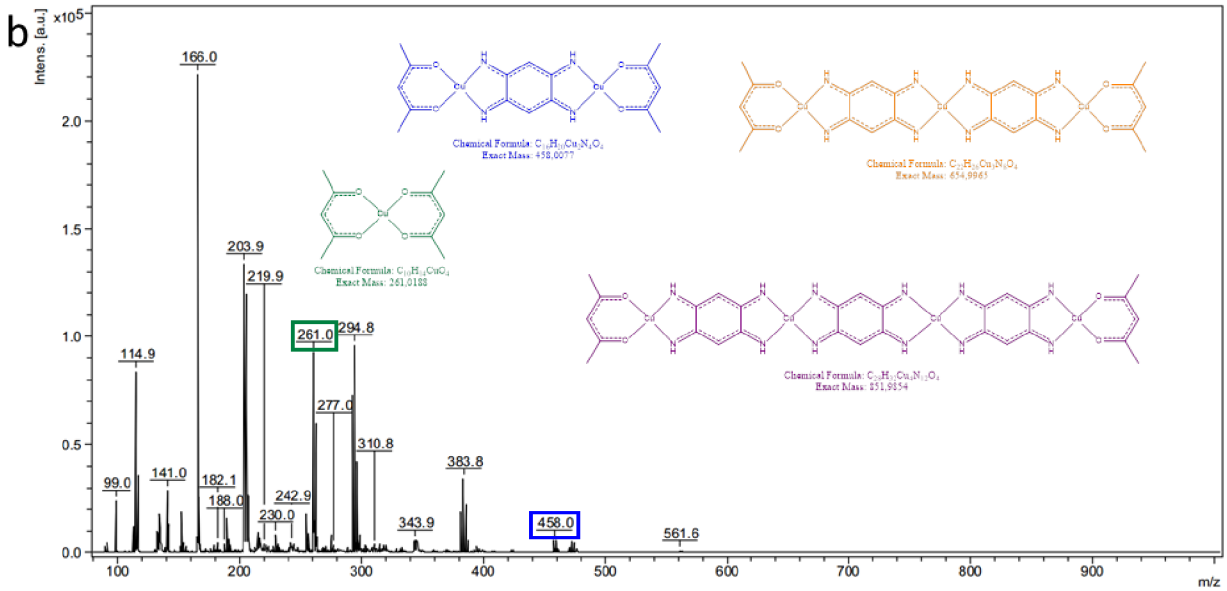
b
x10^5
Intens. [a.u.]
166.0
203.9
219.9
261.0
294.8
277.0
310.8
114.9
99.0
141.0
182.1
188.0
242.9
230.0
343.9
383.8
458.0
561.6
m/z

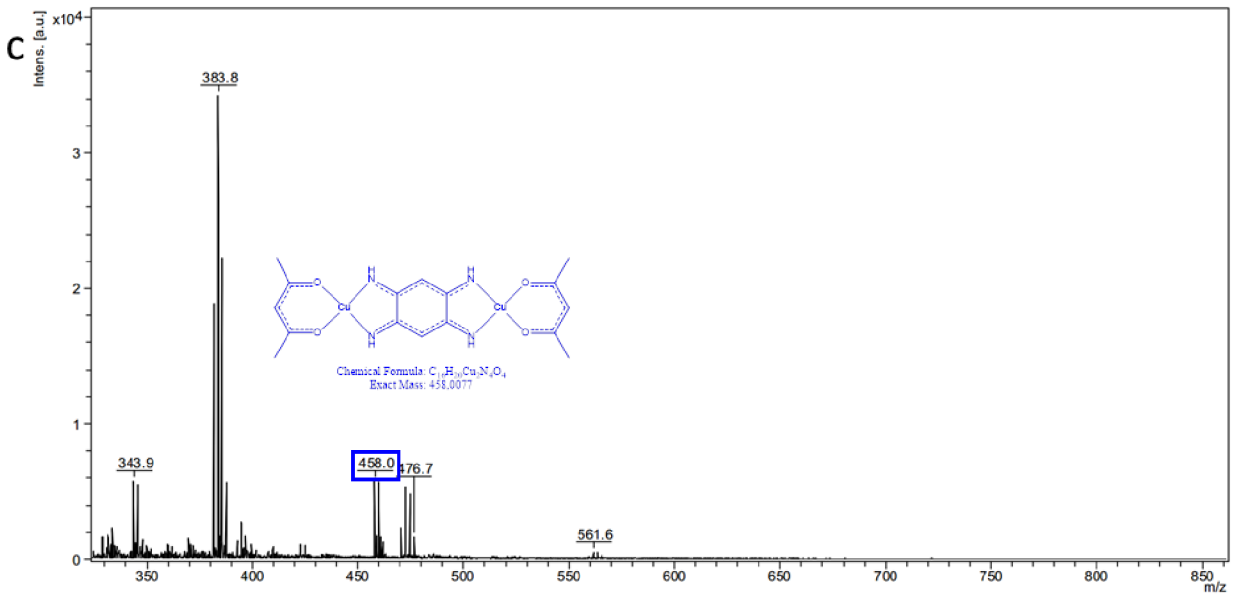

Figure 8: (a) UV-Vis-NIR absorption studies of CuQDI trinuclear complex in DMSO. **(b)** MALDI Analysis (Positive). **(c)** Zoom-in MALDI spectra

References

[1] H. Audi, Z. Chen, A. Charaf-Eddin, A. D'Aléo, G. Canard, D. Jacquemin, O. Siri, *Chem. Commun.*, **2014**, *50*, 15140.

About the Author

E-mail: vm.santhini@gmail.com
Contact number: +420 774362915, +917838316328

Publications

- **Vijai M. Santhini**, Christian Wackerlin, Aleš Cahlík, Martin Ondraček, Simon Pascal, Adam Matěj, Oleksandr Stetsovych, Pingo Mutombo, Petr Lazar, Olivier Siri and Pavel Jelínek ; 1D Coordination π–d Conjugated Polymers with Distinct Structures Defined by the Choice of the Transition Metal:Towards a New Class of Antiaromatic Macrocycles. *Angew.Chem. Int. Ed.* **2021**, 60, 439–445.
- **Vijai M. Santhini**, Oleksandr Stetsovych, Martin Ondraček, Jesus I. Mendieta Moreno, Pingo Mutombo, Bruno de la Torre, Martin Švec, Jiri Klivar, Irena G. Stára, Hector Vazquez, Ivo Stáry, and Pavel Jelínek; On-Surface Synthesis of Polyferrocenylene and its Single-Chain Conformational and Electrical Transport Properties. *Adv. Funct. Mater.* **2021**, 31, 2006391.
- Aleš Cahlík, Jack Hellerstedt, Jesús I. Mendieta-Moreno, Martin Švec, **Vijai M. Santhini**, Simon Pascal, Diego Soler-Polo, Sigurdur I. Erlingsson, Karel Výborný, Pingo Mutombo, Ondrej Marsalek, Olivier Siri, and Pavel Jelínek; Significance Of Nuclear Quantum Effects In Hydrogen Bonded Molecular Chains. *ACS Nano*. **2021**, DOI: 10.1021/acsnano.1c02572.

Conference Participation

- **nc-AFM 22-2019**, Regensburg (Germany), *On surface formation of 1D polyferrocenylene chains on metal surfaces with unique structural and electronic properties* (Poster).
- **DPG-2019**, Regensburg (Germany), *On surface formation of 1D polyferrocenylene chains on metal surfaces with unique structural and electronic properties* (Oral Presentation).
- **SICC 10- 2018**, Singapore, *Semiconducting to Metallic Transitions Observed in Polyferrocenylene Nanowires* (Oral Presentation).
- **NANOCON-2018**, Brno (Czech Republic), *On surface formation of 1D polyferrocenylene chains on metal surfaces with peculiar structural and electronic properties* (Oral Presentation).

Additional Information

- Fischer Scholarship Holder during Ph.D, Department of Physcial Chemistry, Faculty of Science, Palacky University, Olomouc, Czech Republic (2017-2021).
- 3 months Internship in Centre Interdisciplinaire de Nanoscience de Marseille (CINaM) under Prof. Dr. Olivier Siri.
- Dr. Tasilo PRNKA Prize for Oral Presentation, Nanocon 2018, Brno, Czech Republic.